

COMPARING UNSTABLE CISLUNAR ORBITS FOR EFFICIENT TRANSFERS TO DEEP-SPACE TARGETS

by

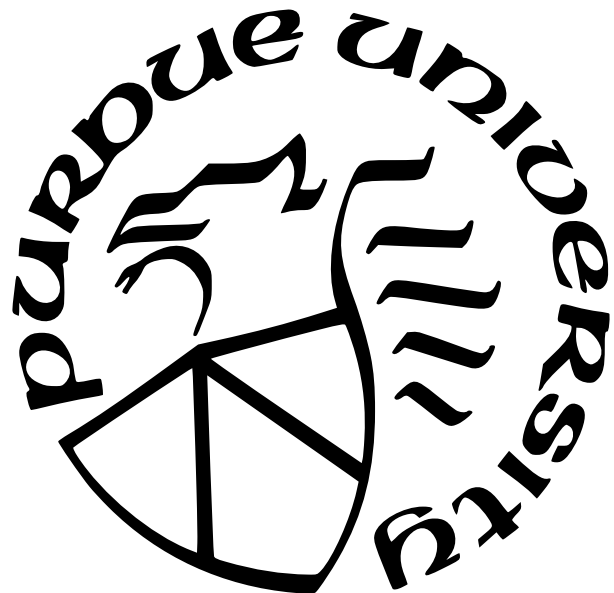
Jonathan H. Richmond

A Thesis

Submitted to the Faculty of Purdue University

In Partial Fulfillment of the Requirements for the degree of

Master of Science in Aeronautics and Astronautics



School of Aeronautics and Astronautics

West Lafayette, Indiana

December 2024

**THE PURDUE UNIVERSITY GRADUATE SCHOOL
STATEMENT OF COMMITTEE APPROVAL**

Dr. Kathleen C. Howell, Chair

School of Aeronautics and Astronautics

Dr. Carolin Frueh

School of Aeronautics and Astronautics

Dr. Kenshiro Oguri

School of Aeronautics and Astronautics

Approved by:

Dr. Denfeng Sun

To my family and my Lord Jesus Christ,
for always having supported me.

"Being confident of this, that he who began a good work in you will carry it on to completion until the day of Christ Jesus." - Philippians 1:6

ACKNOWLEDGMENTS

First and foremost, I would like to thank my advisor Professor Kathleen Howell for inviting me into the research group and continuing to support me and provide me with wonderful opportunities. Her research insights and industry connections have proven invaluable during my time as a Master's student and I have enjoyed learning from her as I strive to contribute to the field of astrodynamics as she has.

I am also grateful to my Master's committee members, Professor Carolin Frueh and Professor Kenshiro Oguri, for taking the time out of their busy schedules to provide insightful advice and feedback on my thesis research. My gratitude also extends to the Purdue University Gambaro Graduate Program of Aeronautics and Astronautics for providing me with office space, access to their technologies and facilities, and the Ross Fellowship which funded this graduate degree, and to Saber Astronautics for funding my research assistantship these last couple of years.

In addition to the faculty at Purdue, many others have contributed to my education and research. In particular, the members of the Multi Body Dynamics Research Group have listened to and provided feedback on hours of brainstorming and presentations over the past three-and-a-half years. Special thanks goes to Colton, Antony, JP, and Ricardo for coursework and research guidance, Liam, Josiah, and Lorin for support as we all defended together, and Nadia for encouraging me throughout the whole process.

I would like to thank my good friend Isaac and Professor Clifford Whitfield for their support during my undergraduate studies at The Ohio State University and for encouraging me to attend graduate school in the first place. I would also like to acknowledge all of my friends and peers from Graduate InterVarsity Christian Fellowship, especially Weston, Edwin, and Emily, who formed my core life support group here in West Lafayette. For her contributions to my research and presentations, I want to extend special gratitude to Alicia, as well as for her continued encouragement and support in academics and in life, even from a distance.

My family deserves the biggest recognition for getting me to where I am today. I would like to thank my parents for pushing me to be the man I am today, providing me with a

loving home and stellar education, and always telling me how proud they are of me. I would like to thank my siblings as well for continuing to be my support system and never failing to bring joy and humor into my life. In addition to these, Grace has been the most constant source of support and motivation in my life through college and graduate school. I could not have made it this far without her, and I am forever grateful to have her in my life. Finally, all the glory and credit for my work goes to my creator and savior, my Lord Jesus Christ, who has brought me thus far and has great plans for my future.

TABLE OF CONTENTS

LIST OF TABLES	9
LIST OF FIGURES	10
LIST OF SYMBOLS	15
ABBREVIATIONS	19
ABSTRACT	20
1 INTRODUCTION	21
1.1 Motivation	21
1.2 Research Objectives	22
1.3 Previous Contributions	24
1.4 Overview of Current Work	26
2 DYNAMICAL MODELS	29
2.1 Coordinate Frames	29
2.1.1 The Barycentric Rotating Frame	29
2.1.2 The Arbitrary Barycentric Inertial Frame	30
2.1.3 The Ecliptic J2000 Primary-Centered Frame	30
2.2 The Relative Two-Body Problem	31
2.2.1 Equations of Motion	32
2.2.2 Conic Sections	33
2.2.3 Keplerian Orbital Elements	34
Cartesian state to Keplerian orbital elements	36
Keplerian orbital elements to Cartesian state	37
2.2.4 Kepler's Equation	38
2.3 The Circular Restricted Three-Body Problem	39
2.3.1 Equations of Motion	39
2.3.2 Nondimensionalized Values	41
2.3.3 Equilibrium Points	42
2.3.4 Jacobi Constant	42
2.4 Patched Dynamical Models	44
2.4.1 The Patched 2BP-CR3BP Model	44
2.4.2 The Blended CR3BP Model	46
2.5 Coordinate Frame Transformations	47
2.5.1 Barycentric Rotating Frame - Primary-Centered Arbitrary Inertial Frame	48
2.5.2 Barycentric Rotating Frame - Ecliptic J2000 Frame	49
3 CR3BP DYNAMICAL STRUCTURES	51
3.1 Differential Corrections	51
3.1.1 State Transition Matrix	51
3.1.2 Multi-Variable Newton-Raphson Method	53
3.1.3 Central Difference Method	54

3.2	Periodic Orbits	56
3.2.1	Lyapunov Orbits	56
A Lyapunov Targeter	56	
Lyapunov Initial Guess	57	
Converged Lyapunov Orbit	58	
Natural Parameter Continuation	58	
3.2.2	Orbital Stability	61
The Monodromy Matrix	61	
Stability Index	62	
Time Constant	63	
Bifurcations	63	
New Family Generation from Bifurcation	65	
3.2.3	Halo Orbits	65
A Halo Targeter	65	
Converged Halo Families	66	
3.2.4	Butterfly Orbits	68
3.2.5	Axial Orbits	68
An Axial Targeter	68	
Converged Axial Families	70	
3.2.6	Vertical Orbits	70
A Vertical Targeter	70	
Converged Vertical Families	72	
3.3	Invariant Manifolds	74
3.3.1	Approximating a Manifold Arc	75
3.3.2	Manifold Time-of-Flight	78
3.4	Poincaré Maps	79
4	CISLUNAR-MARS TRAJECTORY CONSTRUCTION	81
4.1	Near-Ballistic Transfers between the Earth-Moon and Sun-Earth Systems . .	81
4.1.1	Methodology	82
4.1.2	Example	85
4.2	The Moon-to-Moon Analytical Transfer Method	88
4.2.1	Methodology	88
4.2.2	Example	95
4.3	End-to-End Transfers	99
4.3.1	Transfers with Direct System Departure	99
4.3.2	Transfers with an Intermediate Staging Orbit	101
4.3.3	Transfer Tradespace	102
4.4	Modified Keplerian Hohmann Transfer	104
5	CISLUNAR DEPARTURE ORBIT COMPARISON	107
5.1	Comparing Transfers via Intermediate Sun-Earth Halos to Direct Transfers .	107
5.1.1	A Simple Cost Function	108
5.1.2	Comparing Lowest-Cost Solutions between Transfer Types	109
5.2	Comparing Cislunar Departure Families	111

5.2.1	Contributing Factors for Lower Total Maneuver Costs	112
5.2.2	Contributing Factors for Lower Total Times-of-Flight	114
5.2.3	Comparison between Departure Orbits	117
5.3	Comparison to Previous Work	124
6	CONCLUDING REMARKS	129
6.1	Investigation Summary	129
6.1.1	Low-Energy Cislunar-to-Mars Transfer Design Methodology	129
6.1.2	Intermediate Sun-Earth Staging Halo Orbits	130
6.1.3	Cislunar Departure Characteristics	131
6.2	Recommendations for Future Work	133
	REFERENCES	136
A	END-TO-END TRANSFER TRADESPACES	142

LIST OF TABLES

2.1	Orbital values of relevant 2BP systems.	35
2.2	Characteristic values of relevant CR3BP systems.	42
3.1	Manifold-related values of relevant CR3BP systems.	77
4.1	MMAT sphere of influence radii of relevant CR3BP systems.	89
5.1	Representative transfer costs from previous and current investigations.	127

LIST OF FIGURES

2.1	Barycentric rotating and arbitrary inertial frames in a CR3BP system.	30
2.2	Earth-centered Ecliptic J2000 frame.	31
2.3	Two-body problem in a barycentric inertial frame.	32
2.4	Orientation and location along an orbit in an inertial frame utilizing Keplerian orbital elements.	35
2.5	Definition of eccentric anomaly and the auxiliary circle.	39
2.6	CR3BP barycentric rotating frame with Lagrange points.	43
2.7	<i>XY</i> -Projection of the Patched 2BP-CR3BP Model	45
2.8	Patched 2BP-CR3BP sphere of influence around Earth, encompassing a large portion of the Sun-Earth L_2 Lyapunov family.	46
2.9	<i>xy</i> -Projection of the Blended CR3BP Model	47
3.1	Simple Targeting Example.	55
3.2	Converged periodic Lyapunov orbit in the Earth-Moon barycentric rotating frame.	59
3.3	Earth-Moon L_1 Lyapunov orbit family.	60
3.4	Earth-Moon L_2 Lyapunov orbit family.	60
3.5	Earth-Moon Lyapunov family stability index evolution.	63
3.6	Earth-Moon Lyapunov family time constant evolution.	64
3.7	Earth-Moon L_1 northern halo orbit family.	67
3.8	Earth-Moon L_2 northern halo orbit family.	67
3.9	Earth-Moon Halo family stability index evolution.	68
3.10	Earth-Moon southern butterfly family.	69
3.11	Earth-Moon butterfly family stability index evolution.	70
3.12	Earth-Moon L_1 northwest axial orbit family.	71
3.13	Earth-Moon L_2 northeast axial orbit family.	72
3.14	Earth-Moon axial family stability index evolution.	72
3.15	Earth-Moon L_1 vertical orbit family.	73
3.16	Earth-Moon L_2 vertical orbit family.	74
3.17	Earth-Moon vertical family stability index evolution.	74
3.18	Earth-Moon L_1 Lyapunov Manifolds ($C = 3.05$).	77

3.19	Earth-Moon L_2 Halo Manifolds ($C = 3.08$)	78
3.20	Poincaré map	79
4.1	Earth-Moon and Sun-Earth manifolds at the intersection surface in the Sun-Earth rotating frame.	83
4.2	The intersection surface phase plots for Figure 4.1.	84
4.3	Intersection surface phase plots with a near intersection after varying the parameters.	86
4.4	Initial guess for near-ballistic Earth-Moon to Sun-Earth transfer from phase plots in the Sun-Earth rotating frame.	87
4.5	Converged near-ballistic tranfer between Earth-Moon and Sun-Earth halo orbits in the Sun-Earth rotating frame.	87
4.6	Representation of the distant, two-burn MMAT with a plane change (adapted from Canales[37]).	92
4.7	Representation of the two feasible arrival ellipse orientations. The top images are XY -plane views while the bottom are XZ -plane views.	94
4.8	MMAT departure CR3BP arc in the Sun-Earth barycentric rotating frame.	96
4.9	MMAT arrival CR3BP arc in the Sun-Mars barycentric rotating frame.	96
4.10	Evolution along the MMAT family continued by the initial epoch.	97
4.11	Minimum- Δv MMAT in the Sun-centered Ecliptic J2000 frame.	98
4.12	Minimum-TOF MMAT in the Sun-centered Ecliptic J2000 frame.	98
4.13	Direct departure CR3BP arc.	100
4.14	"Direct" MMAT in the Sun-centered Ecliptic J2000 frame.	100
4.15	Departure unstable manifold arc in the Earth-Moon barycentric rotating frame.	102
4.16	Departure CR3BP arc with staging orbit in the Sun-Earth barycentric rotating frame.	103
4.17	MMAT with staging orbit in the Sun-centered Ecliptic J2000 frame.	103
4.18	Tradespace of both solution categories originating from the same Earth-Moon departure orbit.	104
4.19	Hohmann transfer between Earth and Mars.	105
5.1	Transfer tradespace departing from an Earth-Moon L_2 Lyapunov orbit ($JC = 3.03$).	108
5.2	Transfer tradespace departing from an Earth-Moon L_2 northern halo orbit ($JC = 3.13$).	110
5.3	Transfer tradespace departing from an Earth-Moon L_1 Lyapunov orbit ($JC = 3.03$).	111

5.4	Transfer tradespace departing from an Earth-Moon L_1 Lyapunov orbit ($JC = 2.98$)	112
5.5	Northern L_1 halo orbit ($JC = 3.03$) departure manifold arc in the Earth-Moon barycentric rotating frame for a low- Δv case.	114
5.6	Departure CR3BP arc with northern L_2 halo staging orbit ($JC = 3.000808$) in the Sun-Earth barycentric rotating frame for a low- Δv case.	115
5.7	MMAT in the Sun-centered Ecliptic J2000 frame for a staging orbit low- Δv case.	116
5.8	L_1 Lyapunov orbit ($JC = 3.0$) departure CR3BP arc for a low- Δv case.	116
5.9	MMAT in the Sun-centered Ecliptic J2000 frame for a direct low- Δv case.	117
5.10	Northern L_2 halo orbit ($JC = 3.13$) departure manifold arc in the Earth-Moon barycentric rotating frame for a low-TOF case.	118
5.11	Departure CR3BP arc with northern L_2 halo staging orbit ($JC = 3.0008189$) in the Sun-Earth barycentric rotating frame for a low-TOF case.	119
5.12	MMAT in the Sun-centered Ecliptic J2000 frame for a staging orbit low-TOF case.	120
5.13	Northern L_2 halo orbit ($JC = 3.13$) departure CR3BP arc for a low-TOF case.	120
5.14	MMAT in the Sun-centered Ecliptic J2000 frame for a direct low-TOF case.	121
5.15	Average Δv comparison between lowest-cost transfers with staging orbits from various orbits/families.	122
5.16	Average Δv comparison between lowest-cost transfers with direct departures from various orbits/families.	123
5.17	Average TOF comparison between lowest-cost transfers from various orbits/families.	124
5.18	Average cost function value comparison between lowest-cost transfers from various orbits/families.	125
5.19	L_2 Lyapunov orbit ($JC = 3.13$) departure CR3BP arc for lowest-cost case.	125
5.20	MMAT in the Sun-centered Ecliptic J2000 frame for lowest-cost case.	126
A.1	Earth-Moon L_1 Lyapunov departure orbits and their stability characteristics.	142
A.2	Transfer tradespace departing from an Earth-Moon L_1 Lyapunov orbit ($JC = 3.13$)	143
A.3	Transfer tradespace departing from an Earth-Moon L_1 Lyapunov orbit ($JC = 3.1$)	143
A.4	Transfer tradespace departing from an Earth-Moon L_1 Lyapunov orbit ($JC = 3.07$)	144
A.5	Transfer tradespace departing from an Earth-Moon L_1 Lyapunov orbit ($JC = 3.03$)	144
A.6	Transfer tradespace departing from an Earth-Moon L_1 Lyapunov orbit ($JC = 3.0$)	145
A.7	Transfer tradespace departing from an Earth-Moon L_1 Lyapunov orbit ($JC = 2.98$)	145
A.8	Earth-Moon L_2 Lyapunov departure orbits and their stability characteristics.	146

A.9 Transfer tradespace departing from an Earth-Moon L_2 Lyapunov orbit ($JC = 3.13$).	147
A.10 Transfer tradespace departing from an Earth-Moon L_2 Lyapunov orbit ($JC = 3.1$).	147
A.11 Transfer tradespace departing from an Earth-Moon L_2 Lyapunov orbit ($JC = 3.07$).	148
A.12 Transfer tradespace departing from an Earth-Moon L_2 Lyapunov orbit ($JC = 3.03$).	148
A.13 Transfer tradespace departing from an Earth-Moon L_2 Lyapunov orbit ($JC = 3.0$).	149
A.14 Transfer tradespace departing from an Earth-Moon L_2 Lyapunov orbit ($JC = 2.98$).	149
A.15 Earth-Moon L_1 northern halo departure orbits and their stability characteristics.	150
A.16 Transfer tradespace departing from an Earth-Moon L_1 northern halo orbit ($JC = 3.13$).	151
A.17 Transfer tradespace departing from an Earth-Moon L_1 northern halo orbit ($JC = 3.1$).	151
A.18 Transfer tradespace departing from an Earth-Moon L_1 northern halo orbit ($JC = 3.07$).	152
A.19 Transfer tradespace departing from an Earth-Moon L_1 northern halo orbit ($JC = 3.03$).	152
A.20 Earth-Moon L_2 northern halo departure orbits and their stability characteristics.	153
A.21 Transfer tradespace departing from an Earth-Moon L_2 northern halo orbit ($JC = 3.13$).	154
A.22 Transfer tradespace departing from an Earth-Moon L_2 northern halo orbit ($JC = 3.1$).	154
A.23 Transfer tradespace departing from an Earth-Moon L_2 northern halo orbit ($JC = 3.07$).	155
A.24 Transfer tradespace departing from an Earth-Moon L_2 northern halo orbit ($JC = 3.03$).	155
A.25 Earth-Moon L_1 northwestern axial departure orbits and their stability characteristics.	156
A.26 Transfer tradespace departing from an Earth-Moon L_1 northwestern axial orbit ($JC = 3.0$).	157
A.27 Earth-Moon L_2 northeastern axial departure orbits and their stability characteristics.	158
A.28 Transfer tradespace departing from an Earth-Moon L_2 northeastern axial orbit ($JC = 3.0$).	159
A.29 Transfer tradespace departing from an Earth-Moon L_2 northeastern axial orbit ($JC = 2.98$).	159

A.30 Earth-Moon L_1 vertical departure orbits and their stability characteristics. . . .	160
A.31 Transfer tradespace departing from an Earth-Moon L_1 vertical orbit ($JC = 3.1$). .	161
A.32 Transfer tradespace departing from an Earth-Moon L_1 vertical orbit ($JC = 3.07$). .	161
A.33 Transfer tradespace departing from an Earth-Moon L_1 vertical orbit ($JC = 3.03$). .	162
A.34 Transfer tradespace departing from an Earth-Moon L_1 vertical orbit ($JC = 3.0$). .	162
A.35 Transfer tradespace departing from an Earth-Moon L_1 vertical orbit ($JC = 2.98$). .	163
A.36 Earth-Moon L_2 vertical departure orbits and their stability characteristics. . . .	164
A.37 Transfer tradespace departing from an Earth-Moon L_2 vertical orbit ($JC = 3.1$). .	165
A.38 Transfer tradespace departing from an Earth-Moon L_2 vertical orbit ($JC = 3.07$). .	165
A.39 Transfer tradespace departing from an Earth-Moon L_2 vertical orbit ($JC = 3.03$). .	166
A.40 Transfer tradespace departing from an Earth-Moon L_2 vertical orbit ($JC = 3.0$). .	166
A.41 Transfer tradespace departing from an Earth-Moon L_2 vertical orbit ($JC = 2.98$). .	167
A.42 Earth-Moon butterfly departure orbits and their stability characteristics.	168
A.43 Transfer tradespace departing from an Earth-Moon butterfly orbit ($JC = 3.07$). .	169
A.44 Transfer tradespace departing from an Earth-Moon butterfly orbit ($JC = 3.03$). .	169
A.45 Transfer tradespace departing from an Earth-Moon butterfly orbit ($JC = 3.0$). .	170
A.46 Transfer tradespace departing from an Earth-Moon butterfly orbit ($JC = 2.98$). .	170

LIST OF SYMBOLS

Variables

a	Semimajor axis [km]
B	Barycenter
C	Jacobi constant
d	Manifold step-off distance
d_{SoI}	Sphere of influence gravitational ratio
DF	Jacobian matrix
E	Eccentric anomaly [rad (deg)]
\mathcal{E}	Specific mechanical energy [km ² /s ²]
e	Eccentricity
\bar{e}	Eccentricity vector in \mathbb{R}^3
\bar{F}	Constraint vector
\bar{F}_g	Gravitational force vector in \mathbb{R}^3 [kN]
G	Universal gravitational constant [kN*km ² /kg ²]
\tilde{G}	Normalized gravitational constant
g	Gravitational acceleration
\bar{h}	Specific angular momentum vector in \mathbb{R}^3 [km ² /s]
i	Inclination [rad (deg)]
J	Cost function cost
L	Lagrange (equilibrium) point
l^*	Characteristic length [km]
M	Mean anomaly [rad (deg)]
m	Mass [kg]
m^*	Characteristic mass [kg]
MI	Momentum integral
n	Mean motion [rad/s (deg/s)]
\tilde{n}	Normalized mean motion
\bar{n}	Node vector in \mathbb{R}^3

P	Primary
\mathbb{P}	Period [s]
\mathcal{P}_b	Bridge ratio
\bar{Q}	Inertial state vector in \mathbb{R}^6
\bar{q}	Rotating state vector in \mathbb{R}^6
\bar{R}	Inertial position vector in \mathbb{R}^3 [km]
r	Distance [kg]
\bar{r}	Position vector in \mathbb{R}^3 [km]
$\dot{\bar{r}}$	Velocity vector in \mathbb{R}^3 [km/s]
$\ddot{\bar{r}}$	Acceleration vector in \mathbb{R}^3 [km/s ²]
r_a	Radius of apoapsis [km]
r_p	Radius of periapsis [km]
r_{SOI}	Sphere of influence radius
s/c	Spacecraft
T	Epoch [s]
t	Time [s]
t^*	Characteristic time [s]
TOF	Time-of-flight [s]
U	Pseudo-potential
v	Velocity [km/s]
\bar{v}	Velocity vector in \mathbb{R}^3 [km]
v_r	Radial velocity [lm/s]
X	Position along the \hat{X} -axis in an inertial frame [km]
\bar{X}	Free variable vector
\ddot{X}	Acceleration along the \hat{X} -axis in an inertial frame [km/s ²]
x	Position along the \hat{x} -axis in a rotating frame
\dot{x}	Velocity along the \hat{x} -axis in a rotating frame
\ddot{x}	Acceleration along the \hat{x} -axis in a rotating frame
Y	Position along the \hat{Y} -axis in an inertial frame [km]

\ddot{Y}	Acceleration along the \hat{Y} -axis in an inertial frame [km/s ²]
y	Position along the \hat{y} -axis in a rotating frame
\dot{y}	Velocity along the \hat{y} -axis in a rotating frame
\ddot{y}	Acceleration along the \hat{y} -axis in a rotating frame
Z	Position along the \hat{Z} -axis in an inertial frame [km]
\ddot{Z}	Acceleration along the \hat{Z} -axis in an inertial frame [km/s ²]
z	Position along the \hat{z} -axis in a rotating frame
\dot{z}	Velocity along the \hat{z} -axis in a rotating frame
\ddot{z}	Acceleration along the \hat{z} -axis in a rotating frame
Γ	Periodic solution
Δv	Change in velocity that characterizes a maneuver
ϵ	Machine tolerance
θ	True anomaly [rad (deg)]
κ	Small perturbation
λ	Eigenvalue
μ	CR3BP mass ratio
μ_{2BP}	Two-body gravitational constant [kN*km ² /kg]
$\bar{\nu}$	Eigenvector in \mathbb{R}^6
\bar{P}	Inertial position vector in \mathbb{R}^3
$\dot{\rho}$	Barycentric rotating velocity
$\bar{\rho}$	Barycentric rotating position vector in \mathbb{R}^3
$\dot{\bar{\rho}}$	Barycentric rotating velocity vector in \mathbb{R}^3
Σ	Hyperplane
ς	Stability index
τ	Time
Υ	Time constant
Φ	State transition matrix
ϕ	State transition matrix element
Ω	Right ascension of ascending node (RAAN) [rad (deg)]

ω Argument of periapsis [rad (deg)]

$\bar{\omega}$ Angular velocity vector in \mathbb{R}^3

Coordinate Frames

$\{\hat{X}, \hat{Y}, \hat{Z}\}$ Arbitrary inertial coordinate frame

$\{\hat{X}_{Ec}, \hat{Y}_{Ec}, \hat{Z}_{Ec}\}$ Ecliptic J2000 inertial coordinate frame

$\{\hat{x}, \hat{y}, \hat{z}\}$ Rotating coordinate frame

ABBREVIATIONS

2BP	2-Body Problem
BCR4BP	Bicircular Restricted 4-Body Problem
CR3BP	Circular Restricted 3-Body Problem
DRO	Distant retrograde orbit
ER3BP	Elliptic Restricted 3-Body Problem
E-M	Earth-Moon
HFEM	High-fidelity ephemeris model
HR3BP	Hills Restricted 3-Body Problem
HR4BP	Hills Restricted 4-Body Problem
LEO	Low Earth orbit
LMO	Low Mars orbit
MMAT	Moon-to-moon analytical transfer
NAIF	Navigation and Ancillary Information Facility
NASA	National Aeronautics and Space Administration
NRHO	Near-rectilinear halo orbit
QBCR4BP	Quasi-Bicircular Restricted 4-Body Problem
RAAN	Right ascension of ascending node
SoI	Sphere of influence
STM	State transition matrix
SVD	Singular value decomposition
S-E	Sun-Earth
S-M	Sun-Mars
TOF	Time-of-flight

ABSTRACT

With increasing interest in cislunar operations and exploration of deep space destinations like Mars, a foundational understanding of cislunar dynamics and their potential for facilitating departure from the vicinity of Earth is essential. This investigation addresses this need by analyzing system departure characteristics from a variety of periodic orbit families with unstable members in the Earth-Moon Circular-Restricted 3-Body Problem (CR3BP). Specifically, a cislunar-to-Mars transfer methodology is developed, leveraging multi-body dynamical systems theory, especially invariant manifolds of periodic orbits, to design lower-energy deep space transfers in comparison to traditional methods. The proposed approach generates families of end-to-end transfers that vary in total maneuver Δv cost and time-of-flight, originating from different unstable cislunar orbits. The tradespaces of these transfer families are then analyzed and compared across various departure orbits to identify departure characteristics across orbit families and energy levels (Jacobi constants). The analysis reveals certain unstable Earth-Moon CR3BP orbit families with more favorable departure characteristics. Additionally, this investigation compares the computed deep space transfer costs with those of traditional interplanetary transfers and others from existing literature. Although this transfer design strategy is specifically applied to Mars transfers in this investigation, the methodology is broadly applicable to other deep space destinations. Furthermore, the general findings on cislunar departure characteristics have implications for mission designs to destinations beyond the Earth-Moon region.

1. INTRODUCTION

1.1 Motivation

In recent years, international interest in cislunar missions and operations has rapidly increased. This is evidenced by the development of infrastructure for the National Aeronautics and Space Administration's (NASA) Gateway program, a long-term hub that will reside in an Earth-Moon Near-Rectilinear Halo Orbit (NRHO) in the lunar vicinity[1]. While there are a lot of exciting opportunities for cislunar missions, periodic orbits and dynamical structures in this region of space can also be exploited as stepping stones on the way to deep-space exploration. In its 2022 Strategic Plan, NASA outlines goals to "Extend human presence to the Moon and on towards Mars for sustainable long-term exploration, development, and utilization" and "Enhance space access and services"[2], that are further supported by its "Moon to Mars Objectives" document released that same year[3]. These documents support the idea that operations and infrastructure in the cislunar region can be employed to support future missions to Mars and other deep-space targets.

Unlike Earth orbits, periodic orbits and trajectories in cislunar space exist in a complex multi-body dynamical regime that is significantly affected by gravitational forces from both the Earth and the Moon (and in some cases the Sun). While the addition of these forces introduces new challenges to the trajectory design process, it also provides opportunities to leverage elements of dynamical systems theory in ways that are not possible with standard Keplerian dynamics. These elements include unstable families of periodic orbits with stable and unstable invariant manifolds that are useful for constructing transfers between orbits. These techniques are currently employed to design missions in the cislunar region and similar strategies can be adapted and applied to construct transfers between cislunar orbits and deep-space targets residing outside of the Earth region.

NASA's goal of establishing a permanent presence on Mars necessitates more efficient and adaptable transfer strategies for missions since traditional approaches have high maneuver costs and are inflexible. In the past, NASA and other space agencies have designed and executed uncrewed interplanetary missions to Mars. However, their goal to develop a human presence on Mars in the near future requires an increase in both crewed and un-

crewed missions to the Martian vicinity, highlighting the need for low-cost, reliable transfer strategies. Traditionally, uncrewed interplanetary missions depart from the Earth with high-energy transfers[4]. Not only do these solutions have a high propellant cost, but they are also point solutions that need to be recomputed whenever a mission parameter changes. As humankind prepares for sustained exploration of Mars, the development of more cost-effective and flexible mission strategies is crucial to ensure success.

An alternative option is to depart from a cislunar orbit, perhaps after refueling at a servicing depot, decreasing the propellant costs for both the launch from the surface of Earth and the interplanetary transfer. The past successful applications of multi-body dynamical systems theory to cislunar transfer design suggest that these techniques can also be applied to deep-space transfers with similar performance. Utilizing unstable periodic orbit families and invariant manifold theory allows for lower-energy and lower-cost departures from the Earth-Moon system. After departure, patched dynamical models and existing transfer techniques are employed to complete the construction of end-to-end transfers from the Earth-Moon system to deep-space destinations. One consequence of this approach is that invariant manifolds often increase the trajectory time-of-flight. While long times-of-flight are not desirable characteristics for manned missions due to radiation and other concerns, it is an acceptable trade-off for cargo and supply missions. Consequently, rather than focusing on optimizing the interplanetary transfer itself, comparing available unstable periodic orbit families leads to insight into time-efficient departures from the Earth-Moon system. The exploitation of simplified dynamical models also provides families of transfers instead of point solutions, adding flexibility to the mission design process. Incorporating these dynamical techniques into mission planning offers a more flexible approach to deep-space transfers.

1.2 Research Objectives

To sustain an increase in missions to Mars and other deep-space targets, a framework for lower-cost transfers from the Earth region is necessary. One promising avenue to decrease propellant costs is to utilize invariant manifold theory for low-energy departures from unstable multi-body periodic orbits in the cislunar region. Since the application of multi-

body dynamical systems theory to cislunar mission design is relatively new, little is known about the departure characteristics for families of unstable periodic orbits modeled in the Earth-Moon Circular Restricted 3-Body Problem (CR3BP). Additionally, previous work has determined that invariant manifolds from one Sun-planet CR3BP system do not connect to manifolds in other systems in a practical amount of time[5]. Consequently, new transfer design methodologies must be developed to connect manifolds from planetary systems. Finally, since the current standard methods for interplanetary transfers produce only point solutions, it would be beneficial to have new flexible methodologies that provide families of transfers. Developing these new methodologies that connect invariant manifolds across Sun-planet systems is key to achieving lower-energy deep-space transfers.

Consequently, this investigation aims to develop a design methodology for end-to-end transfers to deep-space targets that provides families of solutions to compare the departure characteristics of unstable Earth-Moon CR3BP periodic orbit families. This goal is broken down into the following objectives:

1. **Establish a low-energy transfer design methodology between the cislunar region and Mars that utilizes CR3BP invariant manifolds.** This new transfer methodology includes a solution for bridging the gap between the invariant manifolds of Sun-planet CR3BP systems. Employing the CR3BP and patched models, the resulting solutions also exist in families, providing flexible mission design.
2. **Compare transfers that stage in intermediate Sun-Earth halo orbits to "direct" transfers.** Immediately once a trajectory departs the Earth-Moon CR3BP, it is in a region of space that is modeled by the Sun-Earth CR3BP. Sun-Earth invariant manifolds may depart their system faster than Earth-Moon manifolds that are propagated in the Sun-Earth model. Consequently, transfers that arrive at an intermediate Sun-Earth staging orbit are compared to those that directly depart the Sun-Earth system trajectory to determine the classification that has more favorable departure characteristics.

3. **Analyze and compare the Earth-Moon departure characteristics of various unstable CR3BP periodic orbit families within the framework of this investigation.** The ultimate goal of this investigation is to compare families of unstable Earth-Moon orbits to determine the ones that provide low-energy transfers to Mars with lower times-of-flight. The results inform future interplanetary and deep-space mission designs and lend insight into cislunar departure dynamics.

To demonstrate the transfer methodologies, all the end-to-end cislunar-to-Mars transfers in this investigation depart from various Earth-Moon CR3BP orbits but arrive at the same Sun-Mars L_1 northern halo orbit. Although this investigation primarily investigates cislunar-to-Mars transfers, the techniques and developed methodologies apply to many other applications involving CR3BP systems and other deep-space targets.

1.3 Previous Contributions

Traditionally, missions to Mars and other deep-space targets employ impulsive transfers that depart directly from the Earth or low Earth orbit (LEO). The three most recent missions in 2020 utilized this approach: the Emirates Mars Mission[6], the Chinese Tianwen-1 mission[7], and NASA’s Mars 2020 mission[8]. Porkchop plots are often applied in tandem with patched conics to quickly provide point initial guesses for various epochs[4]. Earth flybys have also been proposed by Landau and Longuski to reduce propellant requirements[9], while Fritz and Turkoglu harness gravity-assist maneuvers around other bodies[10]. While they are practical strategies for fast transfers, these traditional methods highlight the need for innovative techniques to reduce propellant costs and increase mission flexibility.

The application of multi-body dynamics to space trajectory design has evolved significantly since its origins, leading to its application in several notable missions. One of the biggest breakthroughs in multi-body astrodynamics occurred with the development of the CR3BP by Euler in 1722[11]. However, it took centuries before this model was finally incorporated into trajectory design in the late 20th century. Some notable missions that have utilized multi-body dynamics include the International Sun-Earth Explorer-3 (ISEE-3)[12], Genesis[13], ARTEMIS[14], CAPSTONE[15], and the James Webb Space Telescope[16]. Cur-

rently, this model and associated techniques are also being employed to design the baseline trajectory and operations for NASA’s Gateway hub[1], [17], [18]. Dynamical systems theory continues to play an increasing role in spacecraft mission design, offering new possibilities for future exploration.

Within the context of interplanetary transfers and missions to deep-space targets, although missions applying multi-body dynamical systems theory have yet to be flown, several authors have developed/proposed multi-body dynamics methodologies. Miele and Wang exploit the dynamics of a circular-restricted 4-body problem to numerically optimize transfers between Keplerian LEO and low Mars orbits (LMO)[19]. Going a step further, Conte starts from a lunar distant retrograde orbit (DRO), a stable CR3BP orbit, but still employs pork-chop plots to design direct transfers to low Mars orbits[20], while Esper and Aldrin harness aero-braking to arrive into a Phobos DRO[21]. Interplanetary transfer design strategies utilizing multi-body invariant manifolds started to appear around 2005 with Topputo et al., who investigated transfers between CR3BP Sun-Earth and Sun-Mars Lyapunov orbits[22]. Nakamiya et al. conducted a similar investigation between Sun-Earth and Sun-Mars halo orbits in the Hills Restricted 3-Body Problem (HR3BP)[23]. Haibin et al. added gravity assists and pseudo-manifolds to aid in the transfer process between Sun-Earth and Sun-Mars halo orbits in the CR3BP[24], while Kakoi et al. investigated transfers from Earth-Moon CR3BP halo orbits to Mars[25]. To depart from a stable CR3BP orbit, Cavallari et al. utilize Earth-Moon Lyapunov manifolds to facilitate transfers between lunar DROs and Sun-Mars Lyapunov orbits[26]. Most recently in 2022, Scantamburlo et al. investigated Lyapunov manifolds in the Elliptic Restricted 3-Body Problem (ER3BP) to connect the Sun-Earth and Sun-Mars systems[27], and Canales et al. employed a semi-analytical moon-to-moon transfer design methodology to construct trajectories between CR3BP Sun-Earth and Sun-Mars halo orbits[28], [29]. Taking a slightly different approach, Lu et al.[30], Shimane and Ho[31], and Singh and Negi[32] investigated the application of low-thrust maneuvers (instead of impulsive) to connect the invariant manifolds of Sun-planet systems. Almost all of these previous studies treat the Sun-Earth and Sun-Mars systems as coplanar, and none of them include analyses of other periodic orbit families besides Lyapunovs and halos.

Several authors have also investigated connecting Earth-Moon to Sun-Earth orbits in their respective CR3BP systems. Masdemont et al. go directly to CR3BP Sun-Earth libration point orbits from Keplerian lunar orbits[33]. The previous study by Kakoi et al. utilizes a patched CR3BP model to ballistically connect Earth-Moon and Sun-Earth halo orbits in their actual respective planes[25]. Guo and Lei conducted a similar investigation to CR3BP Sun-Earth libration point orbits[34], whereas Pasquale et al. investigated heliocentric escape options[35]. Finally, other authors have also investigated connections in other dynamical models, such as Boudad et al. with the Bi-Circular Restricted 4-Body Problem (BCR4BP)[36]. These studies demonstrate the growing interest in leveraging multi-body dynamical systems theory to connect various space regimes, offering valuable insights for future mission designs.

1.4 Overview of Current Work

The main goal of this investigation is to compare families of unstable periodic orbits in the Earth-Moon CR3BP to determine the ones that have desirable system departure characteristics. A transfer design methodology is developed between the Earth-Moon and Sun-Mars CR3BP systems that utilizes invariant manifolds to facilitate the orbit family comparison. This methodology consists of two transfer types: one that stages at an intermediate Sun-Earth halo orbit and one that directly departs the system. Both types produce families of transfers instead of just point solutions, allowing for more flexible mission designs. The resulting methodology and results apply to other deep-space targets besides Mars, such as Venus or asteroids, and provide insight into general low-energy interplanetary transfers.

The following chapters elaborate on the cislunar-to-Mars transfer design methodology and the CR3BP Earth-Moon unstable orbit family analysis:

- **Chapter 2: Dynamical Models**

This chapter introduces the dynamical models and coordinate frames that are employed in this investigation. The relative 2-Body Problem (2BP) and CR3BP are the main dynamical models utilized, with patched and blended model combinations that describe transitions between the systems. Within the CR3BP, the barycentric synodic rotating

frame is primarily employed to represent trajectories, but a Sun-centered Ecliptic J2000 frame best represents the interplanetary transfers in their entirety.

- **Chapter 3: CR3BP Dynamical Structures**

The techniques from dynamical systems theory that are applied in this investigation are described here. These numerical techniques and dynamical structures are utilized in both the transfer design process and the subsequent analysis of the system departure characteristics. This chapter also includes examples of the unstable CR3BP periodic orbit families that appear throughout this investigation, as well as procedures for generating invariant manifolds from them.

- **Chapter 4: Cislunar-to-Mars Transfer Construction**

Two existing transfer methodologies are adapted and combined to form end-to-end cislunar-to-Mars transfer strategies. All of the transfers utilize a version of the Moon-to-Moon Analytical Transfer (MMAT) method developed by Canales[37]. If transfers stage at an intermediate Sun-Earth orbit, near-ballistic transfers between the Earth-Moon orbits and the Sun-Earth halo orbits are constructed similarly to Kakoi's methodology[38]. This chapter also explains Hohmann transfers and their utility in designing patched conic transfers between the Earth and Mars.

- **Chapter 5: Cislunar Departure Orbit Comparison**

With a fully developed end-to-end transfer strategy, cislunar-to-Mars trajectories are constructed, originating from a variety of unstable Earth-Moon orbits. Several periodic orbit families, and orbits at different Jacobi constants (energy levels) within these families, are analyzed to determine those that provide favorable system departure characteristics compared to the others. This chapter also includes a comparison between the transfers that directly depart the system and those that utilize intermediate staging orbits. It concludes with a comparison of the transfer results to those from the existing literature, including Hohmann transfers.

- **Chapter 6: Conclusion**

The main results and conclusions of the investigation are summarized along with recommendations for potential future work.

2. DYNAMICAL MODELS

In the cislunar and other multi-body environments, the gravitational accelerations from one or more masses can affect spacecraft trajectories simultaneously, depending on their proximity to the vehicle. Multiple dynamical models are available to describe the spacecraft behavior; however, as the fidelity of the models increases, so does their complexity. Consequently, the appropriate dynamical model for a given application is a balance between accuracy and simplicity. This investigation is based on two primary dynamical models: The relative 2-Body Problem (2BP) and the Circular Restricted 3-Body Problem (CR3BP). The 2BP serves as a model for spacecraft dynamics when its behavior is well-represented by assuming it is solely governed by the gravitational influence of a single body, primarily applied to heliocentric arcs along a trajectory. In cases where the dynamics are significantly influenced by the gravitational forces of two bodies, for example, in Sun-planet or the Earth-Moon systems, the CR3BP offers a more accurate description of the spacecraft behavior while remaining simple enough to provide insight into the general dynamics.

2.1 Coordinate Frames

In this investigation, Cartesian coordinate frames are employed to represent three-dimensional vector quantities. Coordinate frames may remain fixed in space or rotate about their origin. Selection of coordinate frame depends on the specific application as it can be advantageous to either position the origin at the center of mass of the system (barycenter) or align it with a primary body of interest.

2.1.1 The Barycentric Rotating Frame

In a CR3BP system, the behavior of a spacecraft is best illustrated within a rotating frame with the origin at the system barycenter. The \hat{x} -axis is defined to extend from the barycenter toward the smaller primary body, while the \hat{z} -axis aligns with the system angular momentum vector. Completing the triad, the \hat{y} -axis is evaluated as $\hat{y} = \hat{z} \times \hat{x}$. This set of unit vectors rotates about the barycenter at a constant angular rate n identical to the mean

motion of the two primaries. Consequently, the primary bodies remain fixed in place in the rotating frame.

2.1.2 The Arbitrary Barycentric Inertial Frame

The rotating frame is also defined relative to the arbitrary barycentric inertial (non-accelerating) frame by an angle θ . When $\theta = 0$ (arbitrarily defined to be true when $t = 0$ in the time-autonomous CR3BP), the two frames are aligned and as time progresses, θ increases as the rotating frame revolves around the shared origin with $\dot{\theta} = n$. The arbitrary inertial frame is denoted with the right-handed unit vectors \hat{X} , \hat{Y} , and \hat{Z} , where $\hat{Z} = \hat{z}$. In Figure 2.1, the barycentric $\{\hat{x}, \hat{y}, \hat{z}\}$ rotating frame and $\{\hat{X}, \hat{Y}, \hat{Z}\}$ arbitrary inertial frame for a sample CR3BP system are illustrated, with their common origin centered at the barycenter of the primaries, P_1 and P_2 .

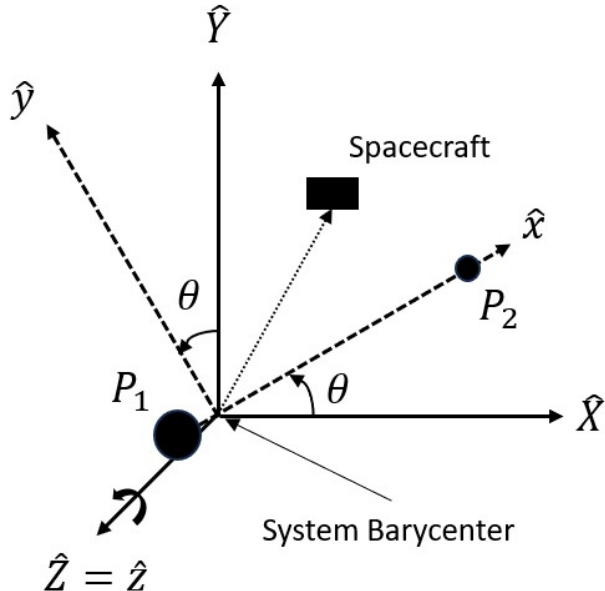


Figure 2.1. Barycentric rotating and arbitrary inertial frames in a CR3BP system.

2.1.3 The Ecliptic J2000 Primary-Centered Frame

A commonly employed primary-centered reference frame is the Ecliptic J2000. As the name implies, this frame is defined with its origin at the center of Earth and the Sun-Earth

orbital (ecliptic) plane on January 1, 2000 as the $\hat{X}_{Ec}\hat{Y}_{Ec}$ -plane. The \hat{X}_{Ec} -axis is directed towards the vernal equinox, the line of intersection between the Earth equatorial and ecliptic planes on January 1, 2000. The \hat{Z}_{Ec} -axis is orthogonal to the ecliptic plane, and the \hat{Y}_{Ec} -axis completes the triad, defined as $\hat{Y}_{Ec} = \hat{Z}_{Ec} \times \hat{X}_{Ec}$. In this investigation, the Ecliptic J2000 frame is utilized with its origin translated to the center of the Sun, the shared primary body for the patched dynamical model. The Ecliptic J2000 coordinate frame, as illustrated in Figure 2.2, is computed from the Navigation and Ancillary Information Facility (NAIF) SPICE ephemeris toolkit[39].

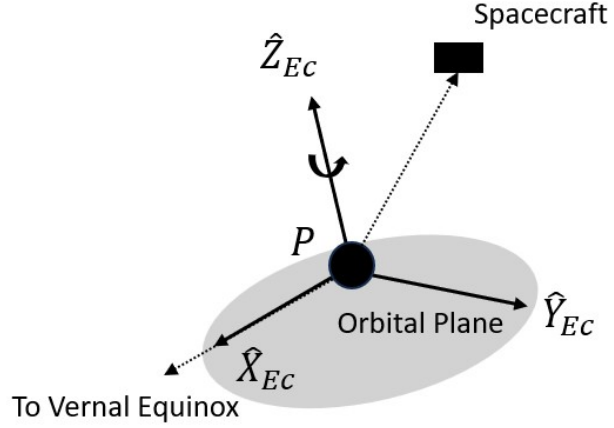


Figure 2.2. Earth-centered Ecliptic J2000 frame.

2.2 The Relative Two-Body Problem

This investigation treats the behavior of spacecraft in heliocentric space, specifically when they are far from planets and moons, as a relative 2-body Problem, governed by a single gravitational force. This section provides a brief overview of key aspects of relative 2BP dynamics, Keplerian orbital elements, and Kepler's Equation. For a more comprehensive derivation of the 2BP, refer to Chapters 1 and 2 of Vallado's *Fundamentals of Astrodynamics and Applications*[40]. Additionally, Canales highlights the background information relevant to understanding the transfer methodologies presented in this analysis[37].

2.2.1 Equations of Motion

The relative 2BP involves two point masses, for example, a primary body and a spacecraft, that exert gravitational forces on each other. Since external forces are not acting on the system, the center of mass of these two bodies moves at a constant velocity and serves as the origin for an inertial coordinate frame. In the inertial frame, the gravitational force that the primary body exerts on the spacecraft, denoted as $\bar{F}_{g_{P \rightarrow s/c}}$, is expressed as:

$$\bar{F}_{g_{P \rightarrow s/c}} = -\frac{Gm_P m_{s/c}}{r_{P \rightarrow s/c}^3} \bar{r}_{P \rightarrow s/c}, \quad (2.1)$$

where G is the universal gravitational constant (6.67384×10^{-20} kN*km 2 /kg 2), m_P and m_S are the masses of the primary and secondary body, e.g., a spacecraft, respectively, $r_{P \rightarrow s/c}$ is the distance from the primary body to the spacecraft, and $\bar{r}_{P \rightarrow s/c} = \bar{r}_{s/c} - \bar{r}_P$ is the relative position vector from the primary body to the spacecraft in the inertial frame, as illustrated in Figure 2.3.

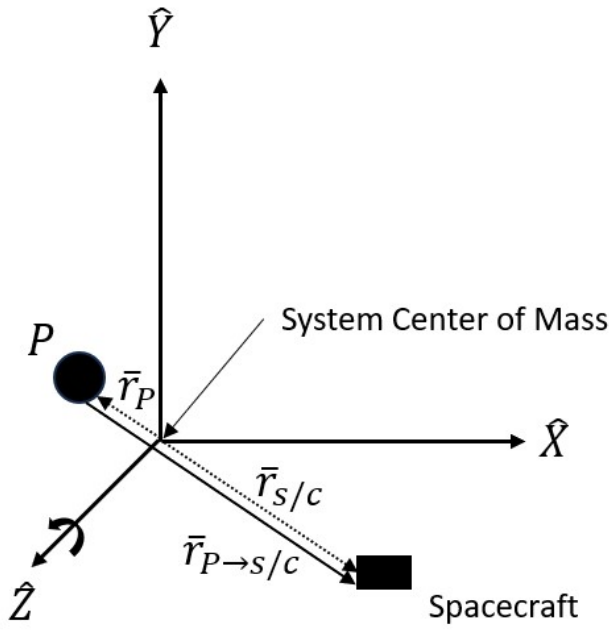


Figure 2.3. Two-body problem in a barycentric inertial frame.

Within the relative inertial frame, the 2BP equations of motion are derived in both vector and scalar forms[37], [40]. Assuming that the secondary mass is negligible compared to the mass of the primary body, in the $\{\hat{X}, \hat{Y}, \hat{Z}\}$ inertial frame:

$$\ddot{\bar{r}}_{P \rightarrow s/c} = -\frac{\mu_{2BP}}{r_{P \rightarrow s/c}^3} \bar{r}_{P \rightarrow s/c}, \quad (2.2)$$

$$\ddot{X} = -\frac{\mu_{2BP}}{r_{P \rightarrow s/c}^3} (X_{s/c} - X_P), \quad (2.3)$$

$$\ddot{Y} = -\frac{\mu_{2BP}}{r_{P \rightarrow s/c}^3} (Y_{s/c} - Y_P), \quad (2.4)$$

$$\ddot{Z} = -\frac{\mu_{2BP}}{r_{P \rightarrow s/c}^3} (Z_{s/c} - Z_P), \quad (2.5)$$

where $\ddot{\bar{r}}_{P \rightarrow s/c}$ is the inertial acceleration vector of the spacecraft relative to the primary body, \ddot{X} , \ddot{Y} , and \ddot{Z} are the scalar components of that acceleration, and $\mu_{2BP} = Gm_P$. These equations of motion are employed to describe spacecraft behavior in heliocentric space in this investigation.

2.2.2 Conic Sections

Instead of relying on numerical propagation of the nonlinear equations of motion, spacecraft behavior in the relative 2BP is effectively represented analytically through conic sections. Two essential constants characterize conic orbits: specific angular momentum \bar{h} and specific mechanical energy \mathcal{E} :

$$\bar{h} = \bar{r}_{P \rightarrow s/c} \times \dot{\bar{r}}_{P \rightarrow s/c}, \quad (2.6)$$

$$\mathcal{E} = \frac{v_{P \rightarrow s/c}^2}{2} - \frac{\mu_{2BP}}{r_{P \rightarrow s/c}}, \quad (2.7)$$

where $v_{P \rightarrow s/c} = \|\dot{r}_{P \rightarrow s/c}\|_2$ is the spacecraft velocity in the inertial frame relative to the primary body. Kepler's first law, asserting that orbital motion is conic, provides the trajectory equation for the 2BP:

$$r_{P \rightarrow s/c} = \frac{a(1 - e^2)}{1 + e \cos(\theta)}, \quad (2.8)$$

where a represents the orbit semimajor axis, e is the orbit eccentricity, and θ denotes the orbit true anomaly. Equation (2.8) is also employed to compute the periapsis and apoapsis distances, r_p and r_a respectively:

$$r_p = a(1 - e), \quad (2.9)$$

$$r_a = a(1 + e). \quad (2.10)$$

The eccentricity also signifies the type of conic section:

- $0 < e < 1$: Elliptical orbit ($e = 0$ represents a circular orbit).
- $e = 1$: Parabola.
- $e > 1$: Hyperbola.

Similarly, Kepler's third law provides the orbit period \mathbb{P} and, consequently, the mean motion:

$$\mathbb{P} = 2\pi\sqrt{\frac{a^3}{\mu_{2BP}}}, \quad (2.11)$$

$$n = \frac{2\pi}{\mathbb{P}} = \sqrt{\frac{\mu_{2BP}}{a^3}}. \quad (2.12)$$

This investigation focuses on arc segments of circles and ellipses in the 2BP with $0 \leq e < 1$.

2.2.3 Keplerian Orbital Elements

Instead of specifying the six-dimensional state of a spacecraft in a relative 2BP elliptical orbit via Cartesian coordinates, six orbital elements are employed to articulate the size, shape, orientation, and current location along the orbit. In addition to the semimajor axis a and eccentricity e , that were introduced earlier and describe the size and shape of the ellipse,

three angles characterize the orientation of the orbit with respect to an inertial frame, as illustrated in Figure 2.4:

- **Inclination** i signifies the tilt of the orbital plane relative to the inertial $\hat{X}_{Ec}\hat{Y}_{Ec}$ -plane.
- **Right ascension of the ascending node** (RAAN) Ω denotes the angle between the \hat{X}_{Ec} -axis and the ascending node, where the orbit crosses the $\hat{X}_{Ec}\hat{Y}_{Ec}$ -plane in the positive \hat{Z}_{Ec} direction.
- **Argument of periapsis** ω is the angle between the ascending node and the periapsis.

Finally, the true anomaly θ defines the spacecraft position relative to the orbit periapsis. Table 2.1 provides the gravitational constants and some relevant orbital values for the two-body systems employed in this investigation.

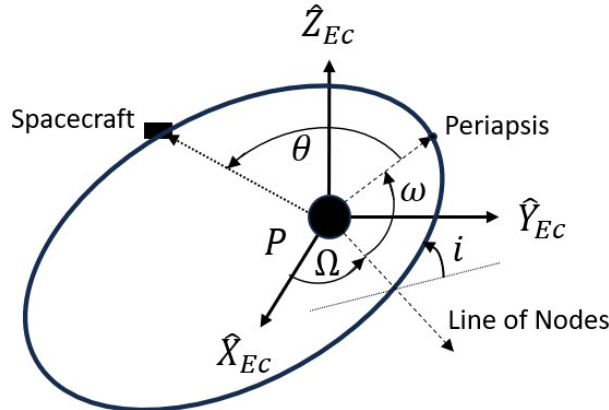


Figure 2.4. Orientation and location along an orbit in an inertial frame utilizing Keplerian orbital elements.

Table 2.1. Orbital values of relevant 2BP systems.

Body	μ_{2BP} [km ³ /s ²]	a [km]	\mathbb{P} [d]	e	i [deg]
Sun	1.32712×10^{11}	-	-	-	-
Earth	398600	1.49598×10^8	365.257	1.67359×10^{-2}	1.70780×10^{-5}
Moon	4902.80	384748	27.4892	5.55455×10^{-2}	5.15665
Mars	42828.4	2.27941×10^8	686.979	9.34015×10^{-2}	1.84971

Cartesian state to Keplerian orbital elements

While Keplerian orbital elements have their benefits, when transitioning between models and coordinate frames, it is convenient to be able to convert between these elements and Cartesian coordinates. To do so, starting from a Cartesian state, the inclination is calculated from the angular momentum:

$$i = \arccos\left(\frac{h_Z}{\|\bar{h}\|}\right). \quad (2.13)$$

From the node vector \bar{n} :

$$\bar{n} = \hat{Z}_{Ec} \times \bar{h}, \quad (2.14)$$

the RAAN becomes:

$$\Omega = \begin{cases} \arccos\left(\frac{n_X}{\|\bar{n}\|}\right) & n_Y \geq 0 \\ 2\pi - \arccos\left(\frac{n_X}{\|\bar{n}\|}\right) & n_Y < 0 \end{cases}. \quad (2.15)$$

The eccentricity vector \bar{e} is also calculated from the angular momentum:

$$\bar{e} = \frac{\dot{\bar{r}}_{P \rightarrow s/c} \times \bar{h}}{\mu_{2BP}} - \frac{\bar{r}_{P \rightarrow s/c}}{r_{P \rightarrow s/c}}, \quad (2.16)$$

and

$$e = \|\bar{e}\|. \quad (2.17)$$

The remaining three orbital elements are calculated as follows:

$$a = \frac{\|\bar{h}\|}{\mu_{2BP}(1 - e^2)}, \quad (2.18)$$

$$\omega = \begin{cases} \arccos\left(\frac{\bar{n} \cdot \bar{e}}{\|\bar{n}\|e}\right) & e_Z \geq 0 \\ 2\pi - \arccos\left(\frac{\bar{n} \cdot \bar{e}}{\|\bar{n}\|e}\right) & e_Z < 0 \end{cases}, \quad (2.19)$$

and

$$\theta = \begin{cases} \arccos\left(\frac{\bar{e} \cdot \bar{r}_{P \rightarrow s/c}}{e r_{P \rightarrow s/c}}\right) & v_r \geq 0 \\ 2\pi - \arccos\left(\frac{\bar{e} \cdot \bar{r}_{P \rightarrow s/c}}{e r_{P \rightarrow s/c}}\right) & v_r < 0 \end{cases}, \quad (2.20)$$

where

$$v_r = \frac{\dot{r}_{P \rightarrow s/c} \cdot \bar{r}_{P \rightarrow s/c}}{r_{P \rightarrow s/c}}. \quad (2.21)$$

These six elements define the Keplerian orbit as well as the specific state along that orbit.

Keplerian orbital elements to Cartesian state

Similarly, the Cartesian state vector can be obtained from the Keplerian orbital elements. First, the eccentric anomaly E is needed, the angle made by the eccentricity vector pointing to periapsis and the vector from the center of the ellipse to the point directly above the spacecraft location (perpendicular to the eccentricity vector) on an auxiliary circle drawn tangent to the ellipse. The eccentric anomaly and the auxiliary circle are illustrated in Figure 2.5, along with the eccentricity vector and semimajor axis. The eccentric anomaly is related to the true anomaly,

$$E = \arctan\left(\frac{\sqrt{1 - e^2} \sin(\theta)}{e + \cos(\theta)}\right), \quad (2.22)$$

that is then utilized to calculate the distance from the primary:

$$r_{P \rightarrow s/c} = a(1 - e \cos(E)). \quad (2.23)$$

These values lead to the position and velocity magnitude vectors:

$$\bar{r}_0 = \begin{bmatrix} r_{P \rightarrow s/c} \cos(\theta) \\ r_{P \rightarrow s/c} \sin(\theta) \\ 0 \end{bmatrix}, \quad (2.24)$$

$$\dot{\bar{r}}_0 = \sqrt{\frac{\mu_{2BPA}}{r_{P \rightarrow s/c}}} \begin{bmatrix} -\sin(E) \\ \sqrt{1 - e^2} \cos(E) \\ 0 \end{bmatrix}. \quad (2.25)$$

The position and velocity vectors need to be rotated relative to the inertial frame axes according to the inclination, RAAN, and argument of periapsis:

$$C = \begin{bmatrix} \cos(\Omega) \cos(\omega) - \cos(i) \sin(\Omega) \sin(\omega) & -\cos(\Omega) \sin(\omega) - \cos(i) \sin(\Omega) \cos(\omega) & 0 \\ \sin(\Omega) \cos(\omega) + \cos(i) \cos(\Omega) \sin(\omega) & -\sin(\Omega) \sin(\omega) + \cos(i) \cos(\Omega) \cos(\omega) & 0 \\ \sin(i) \sin(\omega) & \sin(i) \cos(\omega) & 0 \end{bmatrix}, \quad (2.26)$$

$$\bar{r}_{P \rightarrow s/c} = C \bar{r}_0, \quad (2.27)$$

$$\dot{\bar{r}}_{P \rightarrow s/c} = C \dot{\bar{r}}_0. \quad (2.28)$$

Finally, $\bar{r}_{P \rightarrow s/c}$ and $\dot{\bar{r}}_{P \rightarrow s/c}$ provide the six-dimensional relative state in Cartesian coordinates.

2.2.4 Kepler's Equation

If the difference in true anomaly between two points on an orbit is known, Kepler's equation becomes a valuable tool for calculating the time-of-flight between the two points. The mean anomaly M serves as a measure of the traversal of the orbit past periapsis with respect to time:

$$M = \frac{2\pi(t - t_p)}{\mathbb{P}}, \quad (2.29)$$

where $(t - t_p)$ represents the time since periapsis. Kepler's equation then establishes a connection between the mean and eccentric anomalies, thereby linking the eccentric anomaly to time:

$$M = E - e \sin(E). \quad (2.30)$$

To determine eccentric anomalies given corresponding true anomalies, employ Equation (2.22), and subsequently, with Kepler's equation (Equation (2.30)), convert them to mean anomalies. The difference in mean anomalies with Equation (2.29) provides the time-of-flight between the two points along the orbit.

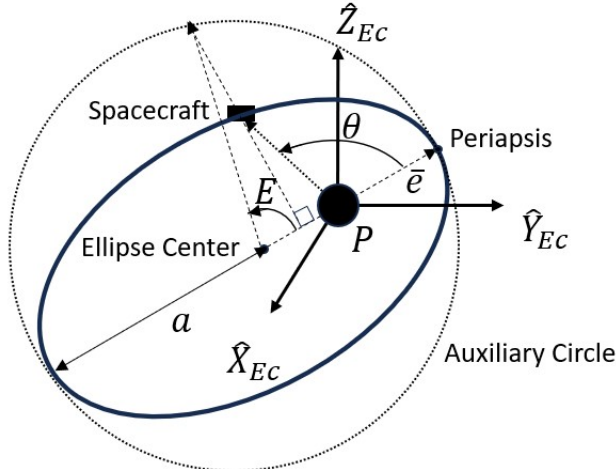


Figure 2.5. Definition of eccentric anomaly and the auxiliary circle.

2.3 The Circular Restricted Three-Body Problem

When a spacecraft is significantly impacted by the gravitational force of two celestial bodies, the circular restricted 3-body problem better approximates the spacecraft behavior compared to two-body problems. Consequently, this investigation employs the CR3BP to model the Earth-Moon and Sun-planet systems when appropriate. The CR3BP is a time-autonomous model (its dynamics are time-invariant) that provides insight into some of the dynamical structures present in the system without the additional complexities of a higher-fidelity ephemeris force model.

2.3.1 Equations of Motion

The CR3BP consists of three primary bodies, two celestial bodies and a massless spacecraft. The two celestial bodies exert gravitational forces on each other and the satellite; however, the satellite does not affect the behavior of the other two bodies. All three bodies are treated as point masses and assumed to move in circular orbits, with a constant angular velocity, around their barycenter B . Assuming that other forces are not acting on the system, B is considered an inertially-fixed point, and similar to the 2BP, Newton's Laws are expressed relative to that point. Unlike the 2BP however, there currently is not an analytical solution to represent the dynamics of the CR3BP. Consequently, all trajectories

in the CR3BP must be numerically propagated in time with nonlinear, coupled equations of motion. It is helpful and common practice to represent and visualize the equations of motion in a barycentric rotating coordinate frame, $\{\hat{x}, \hat{y}, \hat{z}\}$, indicated by the dashed lines in Figure 2.1 and described in Section 2.1. In the rotating frame, the two celestial primaries remain fixed, while the spacecraft moves relative to them in three-dimensional configuration space. This framework provides a foundational model for studying complex spacecraft trajectories, leveraging numerical methods to capture the intricate dynamics of the CR3BP.

A CR3BP system is defined by a single mass ratio μ that characterizes the gravitational interactions and forms the basis for deriving the system equations of motion in the barycentric rotating frame. This parameter is the ratio between the masses of the larger (m_1) and smaller (m_2) celestial primaries:

$$\mu = \frac{m_2}{m_1 + m_2}. \quad (2.31)$$

In the barycentric rotating frame, P_1 is located at $x = -\mu$ and P_2 is located at $x = 1 - \mu$. A pseudo-potential function U describes the gravitational forces on the system expressed in the barycentric rotating frame:

$$U = \frac{1}{2}(x^2 + y^2) + \frac{1 - \mu}{d} + \frac{\mu}{r}, \quad (2.32)$$

$$d = \sqrt{(x + \mu)^2 + y^2 + z^2}, \quad (2.33)$$

$$r = \sqrt{(x - 1 + \mu)^2 + y^2 + z^2}, \quad (2.34)$$

where here, d and r are the distances from P_1 and P_2 , respectively. The scalar nonlinear equations of motion are expressed in the barycentric rotating frame using the pseudo-potential:

$$\ddot{x} = 2\dot{y} + \frac{\partial U}{\partial x} = 2\dot{y} + x - \frac{(1 - \mu)(x + \mu)}{d^3} - \frac{\mu(x - 1 + \mu)}{r^3}, \quad (2.35)$$

$$\ddot{y} = -2\dot{x} + \frac{\partial U}{\partial y} = -2\dot{x} + y - \frac{(1-\mu)y}{d^3} - \frac{\mu y}{r^3}, \quad (2.36)$$

$$\ddot{z} = \frac{\partial U}{\partial z} = -\frac{(1-\mu)z}{d^3} - \frac{\mu z}{r^3}. \quad (2.37)$$

Many authors provide detailed derivations for the equations of motion; one such reference is Zimovan's Ph.D. dissertation[41].

2.3.2 Nondimensionalized Values

Since planetary systems often deal with incongruous distance and velocity scales, it is often helpful in computations to employ normalized length, time, and mass values with nondimensional units. Each CR3BP system has characteristic values that are utilized in the normalization process:

- **Characteristic length** l^* is the distance between the celestial primaries.
- **Characteristic time** t^* is selected so that the mean motion of the primaries is unity ($\tilde{n} = 1$). This results in the primaries having circular orbital periods of 2π nondimensional units.
- **Characteristic mass** m^* is the sum of the masses of the two primaries.

The above definitions result in the following equations:

$$l^* = r_{12}, \quad (2.38)$$

$$m^* = m_1 + m_2, \quad (2.39)$$

$$t^* = \sqrt{\frac{l^{*3}}{Gm^*}}, \quad (2.40)$$

$$\tilde{G} = G \frac{l^{*3}}{m^* t^{*2}} = 1, \quad (2.41)$$

that are employed to normalize all dimensional values in the problem. Table 2.2 provides the mass ratios and characteristic values for the three CR3BP systems in this investigation.

Table 2.2. Characteristic values of relevant CR3BP systems.

CR3BP System	μ	l^* [km]	t^* [s]	m^* [kg]
Earth-Moon	1.21506×10^{-2}	3.84748×10^5	3.75700×10^5	6.04604×10^{24}
Sun-Earth	3.00348×10^{-6}	1.49598×10^8	5.02264×10^6	1.98855×10^{30}
Sun-Mars	3.22715×10^{-7}	2.27941×10^8	9.44664×10^6	1.98855×10^{30}

2.3.3 Equilibrium Points

In the barycentric rotating frame, there are five equilibrium points (also called libration or Lagrange points) that do not experience any net acceleration, i.e., the pseudo-potential acceleration is balanced by the centrifugal acceleration. Consequently, a spacecraft at these positions without any initial velocity remains stationary under CR3BP dynamics. All five Lagrange points lie in the xy -plane. Three Lagrange points lie along the axis of the two celestial primaries and are called the collinear equilibrium points: L_1 is between the two bodies, L_2 is past the smaller body, and L_3 is past the larger body. A Newton-Raphson algorithm is employed to find the location of the equilibrium points for a given mass ratio. L_4 and L_5 are known as equilateral equilibrium points because they form equilateral triangles with the primary bodies. Their locations are determined through a geometric relationship. The energy level (or corresponding Jacobi constant, introduced in the next section) increases through points 1-4 (L_4 and L_5 are at the same energy level). Figure 2.6 provides the layout of the Lagrange points in a generic CR3BP barycentric rotating frame.

2.3.4 Jacobi Constant

One reason that the CR3BP does not have a closed-form analytical solution like the 2BP is that there are not enough integrals of the motion, at least that have been discovered to

date. However, there is one such constant of the motion in the rotating frame, denoted as the Jacobi constant, that is analogous to energy. The derivation is as follows[41]:

$$\nabla U \cdot \dot{\rho} = \frac{\partial U}{\partial x} \dot{x} + \frac{\partial U}{\partial y} \dot{y} + \frac{\partial U}{\partial z} \dot{z} = (\ddot{x} - 2\dot{y})\dot{x} + (\ddot{y} + 2\dot{x})\dot{y} + \ddot{z}\dot{z}, \quad (2.42)$$

where $\dot{\rho}$ is the rotating velocity vector. The middle of Equation (2.42) is equivalent to the total nondimensional time derivative of the pseudo-potential:

$$\frac{dU}{d\tau} = \ddot{x}\dot{x} + \ddot{y}\dot{y} + \ddot{z}\dot{z}, \quad (2.43)$$

where τ is nondimensional time. Integrating and rearranging this equation provides the Jacobi constant as a function of rotating position and velocity:

$$C = 2U - \dot{\rho}^2, \quad (2.44)$$

where C is the Jacobi constant. This definition of the Jacobi constant is consistent with the Hamiltonian of the system, which is time-invariant in the CR3BP[17]. Note also that as the Jacobi constant increases, the energy of the trajectory decreases.

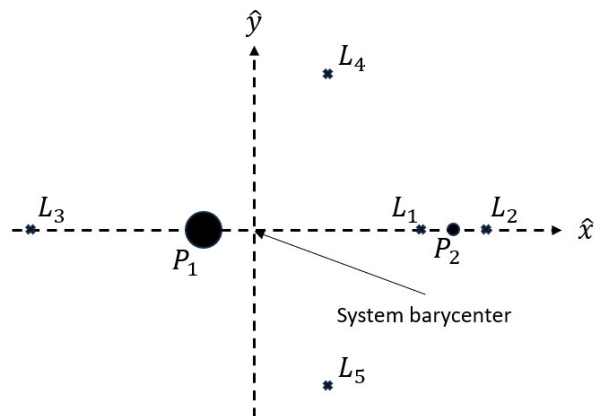


Figure 2.6. CR3BP barycentric rotating frame with Lagrange points.

2.4 Patched Dynamical Models

A variety of methods exist to model the gravitational forces of three (or more) celestial bodies in dynamical systems. While a high-fidelity ephemeris force model (HFEM) provides the most accuracy among these multi-body models, some utilize simplifying assumptions to reduce computations and gain more insight into the dynamics of the system while maintaining adequate fidelity. For including all of the bodies in one model, there exist several 4-body problems that differ in layout, coherency, and fidelity. Some of the more prominent options are the Bi-Circular Restricted 4-Body Problem (BCR4BP)[42], Hills Restricted 4-Body Problem (HR4BP)[43], and Quasi-Bicircular Restricted 4-Body Problem (QBCR4BP)[44]. A different approach, and the one employed in this investigation, is to patch together 2BP and CR3BP models to build a larger model to represent the dynamics. Two such patched models are outlined here.

2.4.1 The Patched 2BP-CR3BP Model

A patched 2BP-CR3BP model describes trajectories as they move between CR3BP systems through a 2BP system. An example from this investigation is leaving the Sun-Earth CR3BP into heliocentric space (modeled as a 2BP) before entering the Sun-Mars CR3BP. While the spacecraft is near a planet, it is modeled in the Sun-planet CR3BP system. But once it reaches a specified distance from that planet, it is modeled instead as Keplarian 2BP motion around the Sun[37]. The interface location between the two models is called the Sphere of Influence (SoI) since it represents where the gravitational influence of the planet becomes negligible compared to that of the Sun. This approach enables a seamless transition between dynamical systems, providing a robust framework for analyzing interplanetary trajectories with high fidelity.

Trajectories computed in this patched model are best represented in a coordinate frame centered at the focus of the 2BP, the Sun in this example. In this investigation, trajectories in the 2BP-CR3BP patched model are viewed in the Sun-centered Ecliptic J2000 frame, as described in Section 2.1. Although the Sun-Earth CR3BP is coplanar with the Ecliptic frame, the Sun-Mars CR3BP system is not, so the Martian orbit is considered to be at its

respective orbital inclination relative to the Sun-Earth ecliptic plane. The XY -projection of an example 2BP-CR3BP patched model system is provided in Figure 2.7. This representation ensures consistency and clarity in visualizing trajectories across different dynamical systems, accommodating the truly inclined orbital planes of celestial bodies.

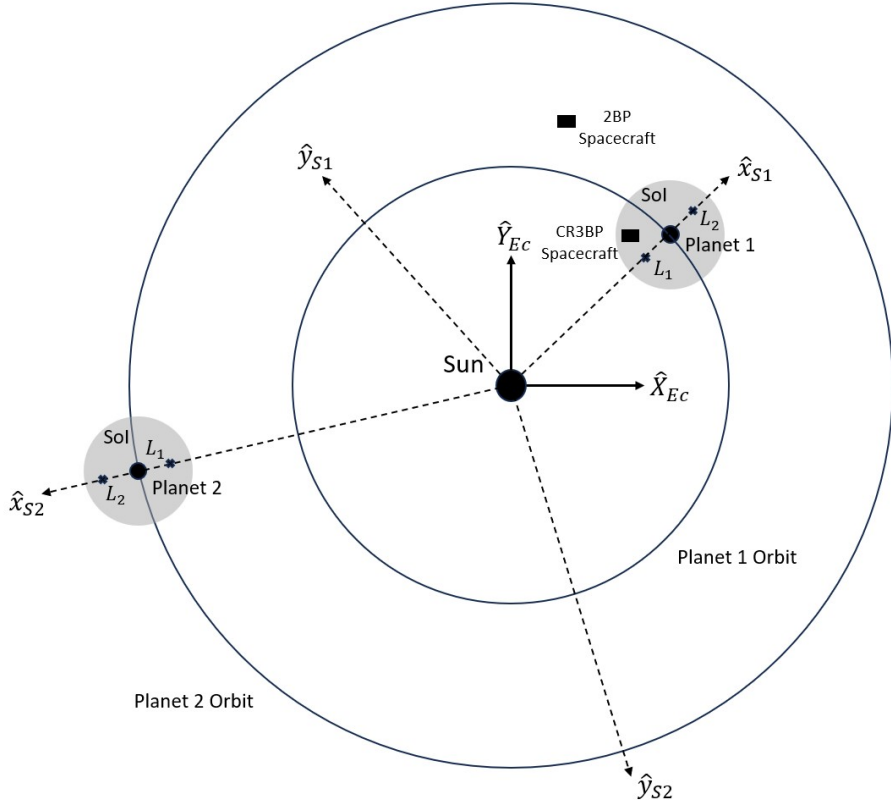


Figure 2.7. XY -Projection of the Patched 2BP-CR3BP Model

The radius of the SoI is a design parameter dependent on the application. For the patched model, an SoI is desired such that many of the CR3BP periodic orbits around the Lagrange points are included within the sphere, demonstrated in Figure 2.8. By defining a gravitational ratio:

$$d_{SoI} = \frac{g_2}{g_1}, \quad (2.45)$$

where g_i is the gravitational acceleration of the respective primary body at a specified location, an SoI radius from the planet is selected so that d_{SoI} is sufficiently small, i.e., the osculating (instantaneous) orbital elements remain near constant in the CR3BP[37]. This

approach ensures that the SoI is appropriately sized to encompass the relevant CR3BP dynamics near the planet.

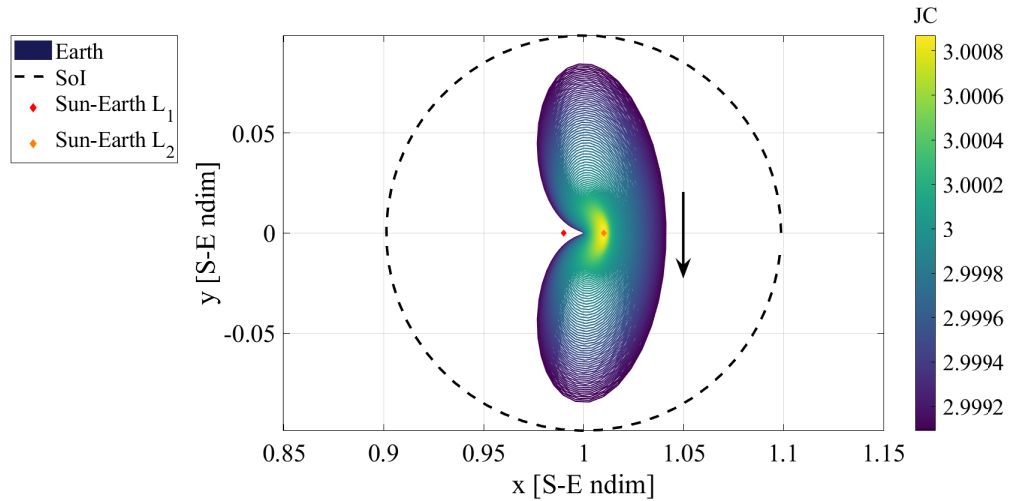


Figure 2.8. Patched 2BP-CR3BP sphere of influence around Earth, encompassing a large portion of the Sun-Earth L_2 Lyapunov family.

2.4.2 The Blended CR3BP Model

Two CR3BP models are also blended to form a 4-body model if one of the primary bodies is present in both models. For example, a Sun-Earth CR3BP is blended with an Earth-Moon CR3BP to form a Sun-Earth-Moon 4-body problem (here, the Earth is the common primary body). The blended model incorporates the difference in inclinations between the two CR3BP models but is now a time-dependent model[25]. Similar to the patched 2BP-CR3BP model, the boundary between the two models is at an SoI, now around the smaller primary of the smaller CR3BP model (the Moon in this example).

Unlike the patched model above, the blended model is best represented in the barycentric rotating frame of the larger CR3BP model (the Sun-Earth rotating frame in this example). Since the blended model is time-dependent, the portion of the trajectory computed in the

smaller CR3BP is shifted when represented in the larger model depending on the epoch. The xy -projection of an example blended system is provided in Figure 2.9.

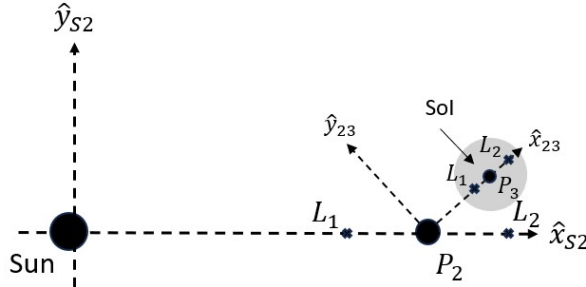


Figure 2.9. xy -Projection of the Blended CR3BP Model

The SoI radius employed for the blended model is different from that for the patched model. As mentioned before, the SoI in this model is centered around the second primary of the smaller system and the gravitational accelerations being compared are the first primary of the larger system and the smaller primary of the second system (e.g., the Sun and the Moon). A blended CR3BP SoI radius is defined as:

$$r_{SoI} = l_{12}^* \left(\frac{m_3}{m_1} \right)^{2/5}, \quad (2.46)$$

where the primaries are numbered in order of decreasing mass[45]. This formulation provides a SoI radius tailored to the blended model, ensuring an accurate representation of the gravitational interactions across the hierarchical systems.

2.5 Coordinate Frame Transformations

Since the patched and blended models in this investigation employ a variety of models centered around different bodies, it is helpful to be able to view any trajectories in multiple reference frames. As mentioned previously, reference frames can be rotating or stationary, and an important component of interplanetary trajectory design is the ability to transform states and trajectories between the two types of frames. A few representative examples of coordinate frame transformations employed in this investigation follow.

2.5.1 Barycentric Rotating Frame - Primary-Centered Arbitrary Inertial Frame

Most trajectories in a CR3BP are constructed in the barycentric rotating frame where Equation (2.35)-Equation (2.37) are defined (see Figure 2.1). However, it can also be beneficial to view trajectories in an inertial reference frame. An arbitrary inertial frame is defined where the inertial unit vectors $\{\hat{X}, \hat{Y}, \hat{Z}\}$ are equivalent to the rotating unit vectors $\{\hat{x}, \hat{y}, \hat{z}\}$ at time t_0 . The origin of the unit vectors is also translated to the center of the primary body.

The following steps transform (nondimensionalized) states from the barycentric rotating frame to the primary-centered arbitrary frame:

1. Translate the position states from barycentric to primary-centric:

$$\bar{\rho}_{P \rightarrow s/c} = \bar{\rho}_{s/c} - \bar{\rho}_P. \quad (2.47)$$

2. Rotate the states depending on time since t_0 . Recall that the mean motion n of the rotating frame is constant. When nondimensionalized in the CR3BP, $\tilde{n} = 1$ and consequently the rotation angle are just $\tau - \tau_0$. Since the \hat{z} - and \hat{Z} -axes coincide for an arbitrary inertial frame, a simple rotation matrix is utilized to rotate the position states:

$$\bar{P} = \begin{bmatrix} \cos(\tau - \tau_0) & -\sin(\tau - \tau_0) & 0 \\ \sin(\tau - \tau_0) & \cos(\tau - \tau_0) & 0 \\ 0 & 0 & 1 \end{bmatrix} \bar{\rho} = {}^I C^R \bar{\rho}, \quad (2.48)$$

where $\bar{\rho}$ is the rotating position and \bar{P} is the inertial position. The basic kinematic equation is then employed to compute the velocity in the rotating frame relative to an inertial observer:

$$\frac{{}^I d\bar{\rho}}{d\tau} = \frac{{}^R d\bar{\rho}}{d\tau} + {}^I \bar{\omega}^R \times \bar{\rho} = \dot{\bar{\rho}} + \hat{z} \times \bar{\rho}, \quad (2.49)$$

where ${}^I \bar{\omega}^R = \tilde{n} \hat{z}$ is the angular velocity relating the two frames. Consequently:

$$\frac{{}^I d\bar{\rho}}{d\tau} = (\dot{x} - y) \hat{x} + (\dot{y} + x) \hat{y} + \dot{z} \hat{z}. \quad (2.50)$$

Utilizing the rotation matrix ${}^I C^R$ from Equation (2.48), Equation (2.50) is expressed in matrix form and combined with the position rotation to achieve full state rotation:

$$\bar{Q} = \begin{bmatrix} {}^I C^R & \bar{0} \\ {}^I \dot{C}^R & {}^I C^R \end{bmatrix} \bar{q}, \quad (2.51)$$

where \bar{q} is the rotating state and \bar{Q} is the inertial state.

3. Dimensionalize the states if desired (see Section 2.3).

To transform a primary-centric arbitrary inertial state to a barycentric rotating state, just reverse the above process (nondimensionalizing the states if necessary), inverting the state rotation matrix.

2.5.2 Barycentric Rotating Frame - Ecliptic J2000 Frame

When designing a trajectory across multiple systems, it is often beneficial to view each part of the trajectory in a common reference frame. In this investigation, the Earth Ecliptic J2000 frame, introduced in Section 2.1 (Figure 2.2), is employed as the common frame for viewing interplanetary trajectories.

The transformation between barycentric rotating frame states and primary-centric Ecliptic J2000 frame states follows a similar process to that for the arbitrary inertial frame. However, since the Ecliptic J2000 frame is defined by a particular epoch (January 1, 2000), the frame rotation is epoch-dependent:

1. Determine the state vector of the second primary with respect to the first in the Ecliptic J2000 frame. To properly compare the two frames, the location of the second primary in its orbit at each epoch of the trajectory is required. This is obtained by retrieving the orbital elements of the second primary at a selected initial epoch from SPICE kernels[39]. The orbital elements are then modified to match the CR3BP orbit assumptions ($a = l^*$ and $e = 0$). Since the mean motion/angular velocity in the CR3BP is constant at $\tilde{n} = 1$:

$$\theta = \tau - \tau_0 + \theta_0, \quad (2.52)$$

where θ_0 is the true anomaly at the initial epoch t_0 obtained from the SPICE kernels. The updated orbital elements are then employed to calculate the full state vector (in dimensional units) of the second primary relative to the first with Equation (2.22)-Equation (2.28).

2. Dimensionalize the trajectory states, times, and angular velocity (see Section 2.3).
3. At each time, translate the position states from barycentric to primary-centric with Equation (2.47) (note that the values should be in dimensional units).
4. Define the instantaneous state rotation matrix utilizing the Ecliptic J2000 state vector of the second primary and angular momentum \bar{h} (Equation (2.6)) at each time:

$$\hat{x} = \frac{\bar{R}_{P_1 \rightarrow P_2}}{|\bar{R}_{P_1 \rightarrow P_2}|}, \quad (2.53)$$

$$\hat{z} = \frac{\bar{h}}{|\bar{h}|}, \quad (2.54)$$

$$\hat{y} = \hat{z} \times \hat{x}, \quad (2.55)$$

$${}^{Ec}C^R = \begin{bmatrix} \hat{x} & \hat{y} & \hat{z} \end{bmatrix}. \quad (2.56)$$

The full state rotation matrix is found through the same process as before, utilizing a dimensional angular velocity:

$${}^{Ec}\dot{C}^R = \begin{bmatrix} n\hat{y} & -n\hat{x} & \bar{0} \end{bmatrix}. \quad (2.57)$$

in Equation (2.51) with dimensional values.

5. Nondimensionalize the states if desired.

States are transformed from a primary-centric Ecliptic J2000 frame to a barycentric rotating frame by reversing the above steps, inverting the state rotation matrix.

3. CR3BP DYNAMICAL STRUCTURES

As mentioned previously, there is not an analytical solution to the CR3BP. Instead, trajectories are propagated with numerical methods. Various numerical techniques are applied to find existing dynamical structures in the model, such as periodic orbits and invariant manifolds, and obtain corresponding initial conditions for propagation. These include differential corrections, natural parameter continuation, eigen-decomposition, and Poincaré mapping.

3.1 Differential Corrections

Differential corrections are employed to compute solutions in targeting problems that satisfy the provided constraints on the initial condition and the trajectory arc. To do so, it is necessary to relate constraints on the trajectory to any parameters in the problem that are free to vary through Jacobians such as the state transition matrix. In this investigation, the targeting process is accomplished via multi-variable Newton-Raphson methods.

3.1.1 State Transition Matrix

The state transition matrix (STM) relates variations in an initial state, $\bar{q}_0 = \bar{q}(t_0)$, to variations in a downstream state $\bar{q}(t)$. Starting from a first-order Taylor series expansion about the baseline trajectory arc, the linear variational equation is derived:

$$\partial \dot{\bar{q}}(t) = A(t) \partial \bar{q}(t), \quad (3.1)$$

where $A(t)$ is the Jacobian matrix for the equations of motion with respect to the state at time t . A full derivation for the CR3BP $A(t)$ matrix is found in Zimovan, but the result is given here[41]:

$$A(t) = \begin{bmatrix} \frac{\partial x}{\partial x_0} & \frac{\partial x}{\partial y_0} & \frac{\partial x}{\partial z_0} & \frac{\partial x}{\partial \dot{x}_0} & \frac{\partial x}{\partial \dot{y}_0} & \frac{\partial x}{\partial \dot{z}_0} \\ \frac{\partial y}{\partial x_0} & \frac{\partial y}{\partial y_0} & \frac{\partial y}{\partial z_0} & \frac{\partial y}{\partial \dot{x}_0} & \frac{\partial y}{\partial \dot{y}_0} & \frac{\partial y}{\partial \dot{z}_0} \\ \frac{\partial z}{\partial x_0} & \frac{\partial z}{\partial y_0} & \frac{\partial z}{\partial z_0} & \frac{\partial z}{\partial \dot{x}_0} & \frac{\partial z}{\partial \dot{y}_0} & \frac{\partial z}{\partial \dot{z}_0} \\ \frac{\partial \dot{x}}{\partial x_0} & \frac{\partial \dot{x}}{\partial y_0} & \frac{\partial \dot{x}}{\partial z_0} & \frac{\partial \dot{x}}{\partial \dot{x}_0} & \frac{\partial \dot{x}}{\partial \dot{y}_0} & \frac{\partial \dot{x}}{\partial \dot{z}_0} \\ \frac{\partial \dot{y}}{\partial x_0} & \frac{\partial \dot{y}}{\partial y_0} & \frac{\partial \dot{y}}{\partial z_0} & \frac{\partial \dot{y}}{\partial \dot{x}_0} & \frac{\partial \dot{y}}{\partial \dot{y}_0} & \frac{\partial \dot{y}}{\partial \dot{z}_0} \\ \frac{\partial \dot{z}}{\partial x_0} & \frac{\partial \dot{z}}{\partial y_0} & \frac{\partial \dot{z}}{\partial z_0} & \frac{\partial \dot{z}}{\partial \dot{x}_0} & \frac{\partial \dot{z}}{\partial \dot{y}_0} & \frac{\partial \dot{z}}{\partial \dot{z}_0} \end{bmatrix} = \begin{bmatrix} 0 & 0 & 0 & 1 & 0 & 0 \\ 0 & 0 & 0 & 0 & 1 & 0 \\ 0 & 0 & 0 & 0 & 0 & 1 \\ \frac{\partial U}{\partial x \partial x} & \frac{\partial U}{\partial x \partial y} & \frac{\partial U}{\partial x \partial z} & 0 & 2n & 0 \\ \frac{\partial U}{\partial y \partial x} & \frac{\partial U}{\partial y \partial y} & \frac{\partial U}{\partial y \partial z} & -2n & 0 & 0 \\ \frac{\partial U}{\partial z \partial x} & \frac{\partial U}{\partial z \partial y} & \frac{\partial U}{\partial z \partial z} & 0 & 0 & 0 \end{bmatrix}, \quad (3.2)$$

$$\frac{\partial U}{\partial x \partial x} = 1 - \frac{1-\mu}{d^3} - \frac{\mu}{r^3} + \frac{3(1-\mu)(x+\mu)^2}{d^5} + \frac{3\mu(x-1+\mu)^2}{r^5}, \quad (3.3)$$

$$\frac{\partial U}{\partial x \partial y} = \frac{\partial U}{\partial y \partial x} = \frac{3(1-\mu)(x+\mu)y}{d^5} + \frac{3\mu(x-1+\mu)y}{r^5}, \quad (3.4)$$

$$\frac{\partial U}{\partial x \partial z} = \frac{\partial U}{\partial z \partial x} = \frac{3(1-\mu)(x+\mu)z}{d^5} + \frac{3\mu(x-1+\mu)z}{r^5}, \quad (3.5)$$

$$\frac{\partial U}{\partial y \partial y} = 1 - \frac{1-\mu}{d^3} - \frac{\mu}{r^3} + \frac{3(1-\mu)y^2}{d^5} + \frac{3\mu y^2}{r^5}, \quad (3.6)$$

$$\frac{\partial U}{\partial y \partial z} = \frac{\partial U}{\partial z \partial y} = \frac{3(1-\mu)yz}{d^5} + \frac{3\mu yz}{r^5}, \quad (3.7)$$

$$\frac{\partial U}{\partial z \partial z} = -\frac{1-\mu}{d^3} - \frac{\mu}{r^3} + \frac{3(1-\mu)z^2}{d^5} + \frac{3\mu z^2}{r^5}. \quad (3.8)$$

The solution to Equation (3.1):

$$\partial \bar{q}(t) = \frac{\partial \bar{q}(t)}{\partial \bar{q}_0} \partial \bar{q}_0, \quad (3.9)$$

is rearranged to provide the STM $\Phi(t, t_0)$:

$$\Phi(t, t_0) = \frac{\partial \bar{q}(t)}{\partial \bar{q}_0}. \quad (3.10)$$

The equation for the STM is appended to the CR3BP equations of motion when propagating:

$$\dot{\Phi}(t, t_0) = A(t)\Phi(t, t_0), \quad (3.11)$$

where the initial condition is $\Phi(t_0, t_0) = I_{6 \times 6}$.

3.1.2 Multi-Variable Newton-Raphson Method

Targeting problems require iterative approaches where an initial guess is updated until it meets a set of constraints to solve a boundary value problem. This investigation employs a multi-variable Newton-Raphson method as a differential corrections process for single-shooting targeting problems, applying analytical or numerical partial derivatives of constraints with respect to the initial conditions. The Newton-Raphson iterative approach facilitates convergence to local solutions that satisfy the boundary conditions.

If \bar{X} is a free variable vector and $\bar{F}(\bar{X})$ is a constraint vector that is dependent on the free variables, then the goal of the targeting problem is to find \bar{X} such that $\bar{F}(\bar{X}) = \bar{0}$ (to a selected tolerance). Example free variable and constraint vectors are introduced in future sections. Applying the Newton-Raphson method, the update equation is provided by a first-order Taylor series expansion about the initial condition \bar{X}_0 :

$$\bar{F}(\bar{X}) = \bar{F}(\bar{X}_0) + DF(\bar{X}_0)(\bar{X} - \bar{X}_0) = \bar{0}, \quad (3.12)$$

where $DF(\bar{X})$ is the Jacobian containing the partial derivatives of the constraints with respect to the free variables. With the update equation, the next iteration on the initial conditions is computed. If the number of free variables matches that of the constraints:

$$\bar{X} = \bar{X}_0 - DF(\bar{X}_0)^{-1}\bar{F}(\bar{X}_0), \quad (3.13)$$

and \bar{X} becomes the new iteration of the initial conditions. Ideally, upon each iteration, the norm of the constraint vector approaches closer to the tolerance. If the number of free variables is greater than the number of constraints, a minimum-norm solution is computed:

$$\bar{X} = \bar{X}_0 - DF(\bar{X}_0)^T (DF(\bar{X}_0)DF(\bar{X}_0)^T)^{-1} \bar{F}(\bar{X}_0). \quad (3.14)$$

When the number of free variables is less than the number of constraints, a least squares solution is employed, but that is not addressed in this investigation.

As a simple targeting example, consider the following planar boundary value problem in Figure 3.1. The objective is to vary the initial velocity and time-of-flight (TOF) to target a desired final position $\bar{\rho}_d$. This results in a free variable vector:

$$\bar{X} = \begin{bmatrix} \dot{x}_0 & \dot{y}_0 & \tau \end{bmatrix}^T, \quad (3.15)$$

and constraint vector:

$$\bar{F}(\bar{X}) = \begin{bmatrix} x_f - x_d & y_f - y_d \end{bmatrix}^T = \bar{0}. \quad (3.16)$$

The Jacobian is comprised of the partial derivatives of the constraint vector with respect to the free variable vector, in this example, a combination of the STM and time derivatives:

$$DF(\bar{X}) = \begin{bmatrix} \frac{\partial(x_f - x_d)}{\partial \dot{x}_0} & \frac{\partial(x_f - x_d)}{\partial \dot{y}_0} & \frac{\partial(x_f - x_d)}{\partial \tau} \\ \frac{\partial(y_f - y_d)}{\partial \dot{x}_0} & \frac{\partial(y_f - y_d)}{\partial \dot{y}_0} & \frac{\partial(y_f - y_d)}{\partial \tau} \end{bmatrix} = \begin{bmatrix} \phi_{14} & \phi_{15} & \dot{x}_f \\ \phi_{24} & \phi_{25} & \dot{y}_f \end{bmatrix}, \quad (3.17)$$

where ϕ are elements of the STM of the propagated arc. These vectors and the Jacobian matrix are then applied with Equation (3.14) to iteratively solve for the free variable vector that satisfies the constraint vector and solves the provided boundary value problem.

3.1.3 Central Difference Method

The Newton-Raphson method utilizes partial derivatives to solve a targeting problem iteratively. These partial derivatives can be provided analytically (like in the previous example) or numerically through an approximation method such as central differencing. The

numerical approach is employed in this investigation to check analytical partial derivatives or when the analytical partials are overly complicated.

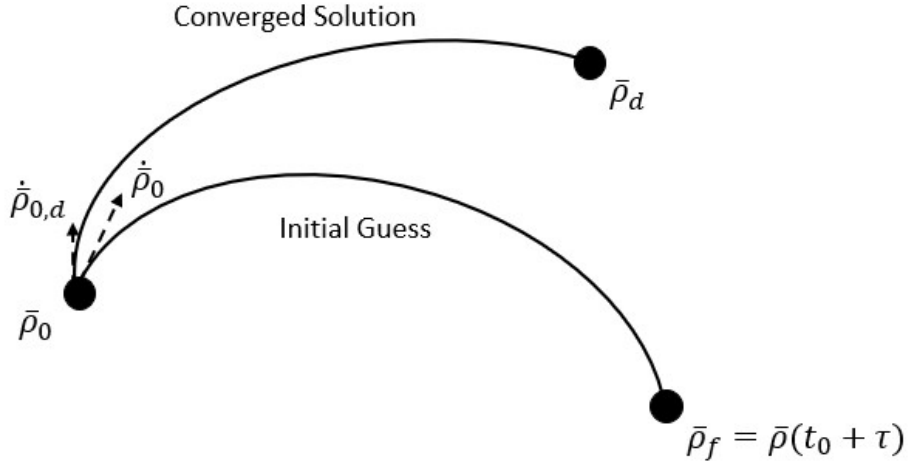


Figure 3.1. Simple Targeting Example.

The central difference method approximates the slope of the solution at discretized points just before and after the initial condition:

$$D\bar{F}_i(\bar{X}_0) = \frac{\partial \bar{F}(\bar{X}_0)}{\partial X_i} = \frac{\bar{F}(X_i + \kappa) - \bar{F}(X_i - \kappa)}{2\kappa}, \quad (3.18)$$

where X_i is one of the components of the free variable vector and κ is a small perturbation (this investigation selects the square root of the machine tolerance, $\sqrt{\epsilon}$). Each variable in the free variable vector is perturbed in both directions by κ , one at a time, and the constraint vector is evaluated at each new free variable vector and substituted into Equation (3.18) above. Perturbing all of the free variables individually makes up the numerical Jacobian:

$$DF(\bar{X}_0) = \begin{bmatrix} D\bar{F}_1(\bar{X}_0) & \dots & D\bar{F}_m(\bar{X}_0) \end{bmatrix}. \quad (3.19)$$

These numerical DF matrices can be compared to their analytical counterparts (such as the example Jacobian in Equation (3.17)) to verify partial derivatives or applied in isolation when analytical partial derivatives are either not available or exceedingly complex.

3.2 Periodic Orbits

With the multi-variable Newton-Raphson scheme described above, periodic solutions are targeted in a CR3BP system. In the CR3BP, these periodic solutions exist as members of families that share similar geometric characteristics. Some of these orbit families are symmetric about a plane or axis in the rotating frame and the symmetry is utilized in the targeting process. In addition, the initial conditions for these families can be obtained through a variety of methods including linear variational equations about the Lagrange points and bifurcations from other orbit families. All of the orbit families utilized in this investigation and that appear here are selected for their relative instability in the Earth-Moon CR3BP. For some example initial conditions and computation strategies for orbit families, see Grebow's[46] and Sadaka's[47] theses and the NASA Jet Propulsion Laboratory CR3BP orbit database[48].

3.2.1 Lyapunov Orbits

A Lyapunov Targeter

To demonstrate the periodic orbit targeting process, a Newton-Raphson scheme is employed to solve for a periodic orbit in the xy -plane of the rotating frame around the first Lagrange point. The family of solutions is known as the L_1 Lyapunov family and they are symmetric about the xz -plane. Consequently, instead of targeting the full orbit, it is only necessary to target half of it, from one perpendicular crossing of the xz -plane to the next. To target one of these orbits at a specified energy level (Jacobi constant), consider the free variable vector:

$$\bar{X} = \begin{bmatrix} x_0 & y_0 & \tau \end{bmatrix}^T. \quad (3.20)$$

Since the boundary value problem being solved starts from a perpendicular crossing, it is only necessary to allow x_0 and y_0 to vary as the rest of the initial states are all 0. In Equation (3.20), τ represents the nondimensional propagation time (TOF) of the initial

conditions. To target another perpendicular crossing for the endpoint of the trajectory arc, the following constraint vector is applied:

$$\bar{F}(\bar{X}) = \begin{bmatrix} y_f & \dot{x}_f & C - C_d \end{bmatrix}^T = \bar{0}, \quad (3.21)$$

where C is the Jacobi constant of the propagated arc and C_d is the desired Jacobi constant. The Jacobian matrix is then comprised of partial derivatives from the STM, time derivatives, and partial derivatives of the Jacobi constant with respect to state variables:

$$DF(\bar{X}) = \begin{bmatrix} \frac{\partial y_f}{\partial x_0} & \frac{\partial y_f}{\partial \dot{y}_0} & \frac{\partial y_f}{\partial \tau} \\ \frac{\partial \dot{x}_f}{\partial x_0} & \frac{\partial \dot{x}_f}{\partial \dot{y}_0} & \frac{\partial \dot{x}_f}{\partial \tau} \\ \frac{\partial(C-C_d)}{\partial x_0} & \frac{\partial(C-C_d)}{\partial \dot{y}_0} & \frac{\partial(C-C_d)}{\partial \tau} \end{bmatrix} = \begin{bmatrix} \phi_{21} & \phi_{25} & \dot{y}_f \\ \phi_{41} & \phi_{45} & \ddot{x}_f \\ 2x_0 - \frac{2(x_0+\mu)(1-\mu)}{d^3} - \frac{2\mu(x_0-1+\mu)}{r^3} & -2\dot{y}_0 & 0 \end{bmatrix}. \quad (3.22)$$

The Jacobian matrix is then inserted into Equation (3.13) to iteratively solve for the free variable vector \bar{X} that solves the provided problem, providing the initial state and half of the propagation time for a periodic Lyapunov orbit.

Lyapunov Initial Guess

An initial guess for a Lyapunov orbit close to the Lagrange point comes from the variational equations of motion, linearized about the equilibrium point:

$$x_0 = x_L + \xi, \quad (3.23)$$

$$\dot{y}_0 = -\beta_3 \xi s, \quad (3.24)$$

where ξ is a selected variation from the x -value of the Lagrange point,

$$\beta_1 = 2 - \frac{\frac{\partial U}{\partial x \partial x} + \frac{\partial U}{\partial y \partial y}}{2}, \quad (3.25)$$

$$\beta_2 = \sqrt{-\frac{\partial U}{\partial x \partial x} \frac{\partial U}{\partial y \partial y}}, \quad (3.26)$$

$$s = \sqrt{\beta_1 + \sqrt{\beta_1^2 + \beta_2^2}}, \quad (3.27)$$

$$\beta_3 = \frac{s^2 + \frac{\partial U}{\partial x \partial x}}{2s}. \quad (3.28)$$

The last part of the initial guess for the free variable vector is the half-period of the orbit τ , approximated by propagating the initial state guess until it reaches the x -axis. The full initial guess serves as the starting point for further refinement in the computation of the Lyapunov orbit.

Converged Lyapunov Orbit

The linear variational equations only approximate the dynamics very close to the Lagrange point. With $\xi = 0.005$ as the initial variation in the x -direction from the L_1 Lagrange point in the Earth-Moon system:

$$\bar{X}_0 = \begin{bmatrix} 0.841915 & -0.0418614 & 1.29755 \end{bmatrix}^T, \quad (3.29)$$

and from the guess for the initial state, $C_d = 3.186877$. The initial free variable guess is propagated under the CR3BP equations of motion and is represented by the dashed curve in Figure 3.2. After targeting a perpendicular crossing with the targeter described above, the solution is propagated (for 2τ) to obtain the full periodic Lyapunov orbit, appearing as a closed, solid curve in Figure 3.2. Note that while the energy of the converged solution matches that of the initial guess, the x - and y -values have shifted slightly.

Natural Parameter Continuation

The process described above produces a single periodic solution near the Lagrange point. To compute more solutions (orbits) in the family, especially further away from the Lagrange point where the linear variational equations no longer apply, converged solutions are utilized in a continuation scheme to compute other family members. This investigation utilizes nat-

ural parameter continuation, where one of the parameters of a converged solution is changed by a small amount. The new guess for an orbit is then converged, and a new solution is obtained. The continuation process is then repeated until the scheme reaches a natural/dynamical end or a desired orbit is reached. Natural parameters of the orbit family include (but are not limited to) components of the initial state, the period, or the Jacobi constant. Figure 3.3 portrays a large portion of the L_1 Lyapunov family in the Earth-Moon system, continued in Jacobi constant from the orbit in Figure 3.2. Lyapunov families also exist about L_2 and L_3 and are computed via the same process. Since L_2 Lyapunov orbits are also utilized in this investigation, they appear in Figure 3.4. This continuation method enables the systematic exploration of orbit families, providing a comprehensive understanding of their dynamics and characteristics within the CR3BP.

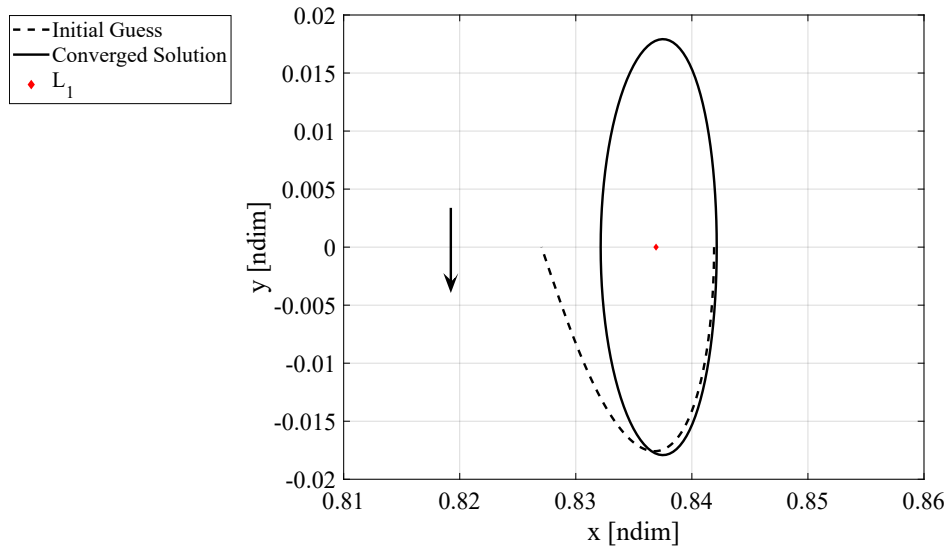


Figure 3.2. Converged periodic Lyapunov orbit in the Earth-Moon barycentric rotating frame.

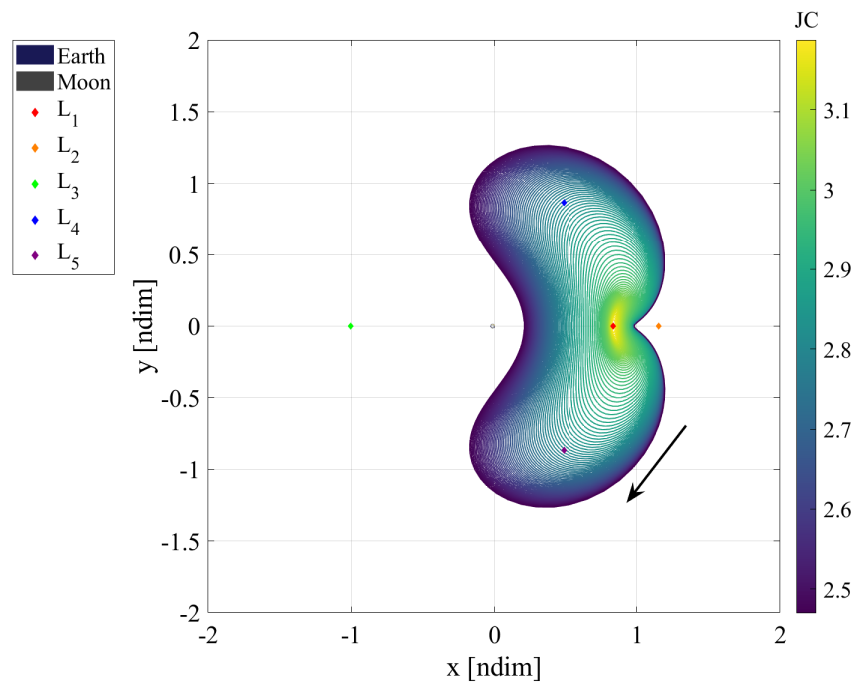


Figure 3.3. Earth-Moon L_1 Lyapunov orbit family.

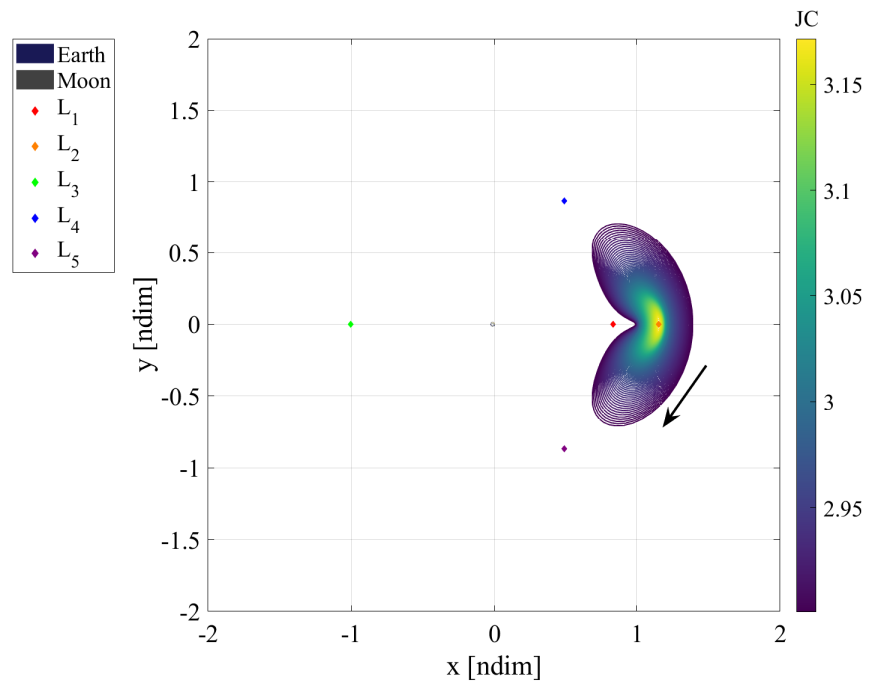


Figure 3.4. Earth-Moon L_2 Lyapunov orbit family.

3.2.2 Orbital Stability

Before discussing other orbit families, it is important to introduce orbital stability as it leads to orbit family bifurcations and another way to generate new orbit families. Orbital stability helps describe the characteristics of the orbit and the surrounding dynamics. The stability of an orbit also informs the best transfer design strategies to minimize the Δv cost. Understanding orbital stability and its consequences is crucial for identifying bifurcations, generating new orbit families, and designing efficient transfers.

The Monodromy Matrix

The STM of one revolution of a periodic orbit in the CR3BP, $\Phi(t_0 + \mathbb{P}, t_0)$, is called the monodromy matrix, and discretely maps the linear growth of perturbations from the periodic solution. Some beneficial properties of the monodromy matrix are that it is symplectic, it has a determinant of 1, and its eigenvalues occur in reciprocal pairs[49]. Since the trajectory is periodic in the CR3BP, two of the eigenvalues (one pair) are always 1, denoted as the trivial pair, and correspond to the periodicity of the trajectory and its membership in a family of solutions.

The stability of the orbit is characterized by the remaining two pairs of eigenvalues. Since the monodromy matrix is a discrete-time mapping of the flow, eigenvalues that lie within the unit circle (magnitude less than 1) in the complex plane are stable and those outside the unit circle are unstable. Perturbations in the stable subspace flow back toward the orbit, while perturbations in the unstable subspace depart the orbit. If the eigenvalues lie directly on the unit circle, then the corresponding flow is in the center subspace and remains bounded around the orbit. When the stability of an eigenvalue pair changes, it can indicate a change in the characteristics of orbits within a family and sometimes leads to a bifurcation in the family, discussed later.

The overall stability of the orbit is then determined by all of the eigenvalues of its monodromy matrix. If any of the eigenvalues are unstable (greater than 1), then the orbit is considered linearly unstable. Note that the existence of an unstable eigenvalue implies the existence of a stable eigenvalue because of the reciprocal pairs. Otherwise, the orbit is

considered marginally stable and all of the eigenvalues reside on the unit circle. Throughout an orbit family, while the stability of the members may change, the eigenvalues experience a smooth (but not necessarily monotonic) evolution.

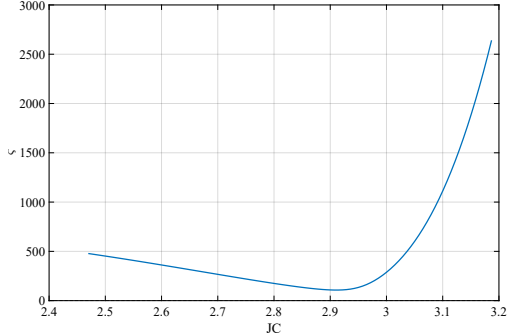
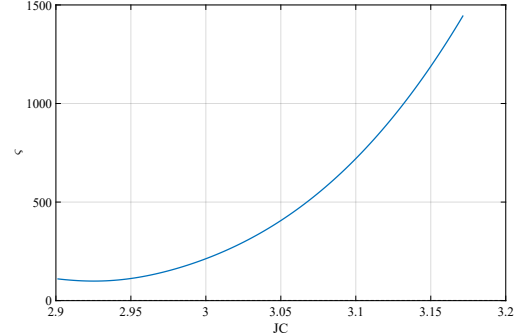
Stability Index

A variety of metrics exist to more succinctly portray the stability of orbits, rather than evaluating all of the eigenvalues. One such metric is a stability index, of which there are a variety of definitions whose utilities vary depending on the application. In this investigation, the focus is on just the overall stability of the orbit — whether it is unstable or marginally stable — so a metric that quickly differentiates between these behaviors suffices. Consequently, the following definition of the stability index is employed:

$$\varsigma = \|\bar{\lambda}\|_\infty, \quad (3.30)$$

where $\bar{\lambda}$ is a vector of the eigenvalues of the monodromy matrix and the infinity norm returns the magnitude of the largest (magnitude) element of the vector[50]. With this definition, $\varsigma > 1$ indicates an unstable orbit and $\varsigma = 1$ indicates one that is marginally stable. Other stability index definitions are utilized by Zimovan Spreen[49].

Like the eigenvalues themselves, the evolution of the stability index over an orbit family is smooth. Figure 3.5 provides the stability indices for the members of the L_1 (a) and L_2 (b) Lyapunov families from Figure 3.3 and Figure 3.4. A larger stability index means that the orbit has a higher instability and perturbations experience faster growth. Note that all of the members of both of these families are unstable. However, there are stability changes among individual eigenvalues within each family that can lead to bifurcations.

(a) L_1 (b) L_2 **Figure 3.5.** Earth-Moon Lyapunov family stability index evolution.

Time Constant

Another beneficial metric of stability is the time constant, which approximates the time it takes for a perturbation to grow by a factor of e. In terms of orbit revolutions:

$$\Upsilon = \frac{1}{\ln \varsigma}. \quad (3.31)$$

Equation (3.31) is multiplied by the period of the orbit \mathbb{P} to produce the time constant in time units. Figure 3.6 illustrates the time constant evolution of both Lyapunov families in orbit revolutions. Note that a larger time constant indicates that it takes longer for a perturbation to grow, indicating that the orbit is less unstable, and a marginally stable orbit has an infinite time constant. The time constant provides a valuable measure of orbital stability, offering insights into the susceptibility of an orbit to perturbations and its long-term dynamical behavior.

Bifurcations

Within the context of the CR3BP, bifurcation theory is applied to detect changes in the orbit stability characteristics within a family that sometimes lead to the generation of new orbit families. These new solutions branch off from the original family and generally have different characteristics. Zimovan Spreen provides a more thorough analysis of applying

bifurcation theory to the CR3BP, so only the information most relevant to this investigation is provided here[49].

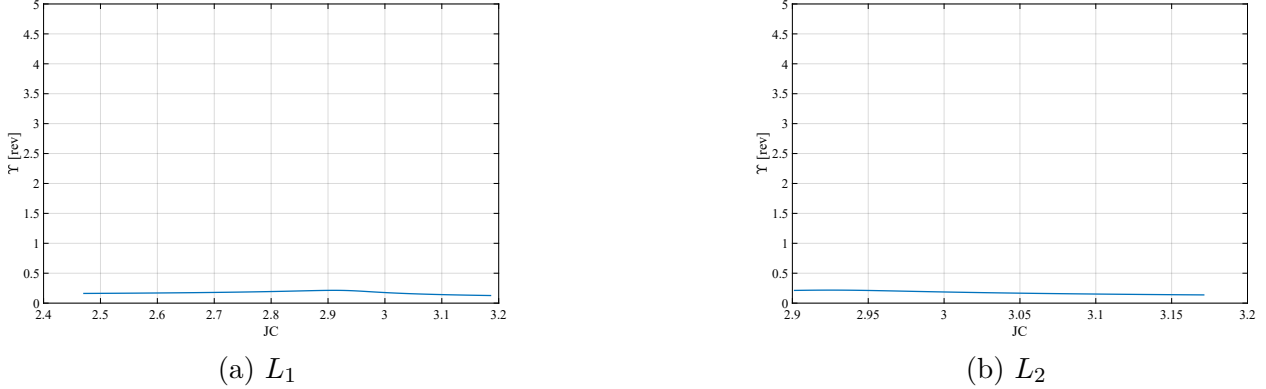


Figure 3.6. Earth-Moon Lyapunov family time constant evolution.

Two main bifurcation types are relevant to the orbits employed in this analysis:

- **Tangent bifurcations** occur when an eigenvalue pair reaches 1, either from the unit circle or the real axis. With a cyclic fold tangent bifurcation, occurring at an extremum in the Jacobi constant, the stability of the eigenvalues changes, but there is not a new family of solutions created. Pitchfork tangent bifurcations produce two new families that have the same stability as the original family. The last subtype, transcritical tangent bifurcations, produce a new family and a change in the eigenvalue stability of the original family.
- **Period-multiplying bifurcations** occur when an eigenvalue pair reaches a root of 1 ($\sqrt{1}$, $\sqrt[3]{1}$, $\sqrt[m]{1}$, etc.). In general, this bifurcation produces a new family with a period m times the original, but not necessarily a change in stability. The most commonly seen multiple is the period-doubling bifurcation, where the pair of eigenvalues meets at -1 either from the unit circle or the real axis. Period-doubling bifurcations result in a change in the stability of the eigenvalues and a new family whose bifurcating member has double the period of the original bifurcating orbit.

There are other methods of detecting bifurcations beyond examining the evolution of the eigenvalues such as Broucke stability or bifurcation diagrams that are also described by Zimovan Spreen[49].

New Family Generation from Bifurcation

To find the initial conditions of an orbit in a new bifurcated family, first the precise bifurcating orbit (within a specified tolerance) is obtained through a simple bisection algorithm. The Jacobian matrix of the bifurcating orbit has an additional nullspace compared to the other orbits in the family since another pair of eigenvalues (besides the trivial pair) have values of 1. Note that for a period-multiplying bifurcation, the orbit must be propagated for m revolutions to obtain the proper Jacobian matrix. After doing so, one of the nullspace vectors points in the direction of continuing the old family, while the other vector indicates a direction for the new family. The bifurcation process enables the precise identification of the orbit step-off, providing a foundation for exploring potential new orbit families.

To identify another orbit in a new bifurcated family, a singular value decomposition (SVD) of the monodromy matrix provides the new nullspace direction as the right singular vector of DF corresponding to the new singular value of 0. Stepping in the nullspace direction from the initial conditions of the bifurcating orbit and correcting for a periodic solution results in a new periodic orbit belonging to the new family. This approach is also known as pseudo-arclength continuation but the new member can then be continued utilizing any available scheme to obtain more of the new family.

3.2.3 Halo Orbits

A Halo Targeter

Similar to Lyapunov orbits, halo orbits are symmetric about the xz -plane, although they are spatial in the rotating frame and not limited to the xy -plane. The symmetry again allows for targeting only half of the periodic orbit, from one perpendicular crossing to the next. Since there is now a z -component to the orbits, it is helpful to introduce a new free variable and constraint for the halo targeter:

$$\bar{X} = \begin{bmatrix} x_0 & z_0 & y_0 & \tau \end{bmatrix}^T, \quad (3.32)$$

$$\bar{F}(\bar{X}) = \begin{bmatrix} y_f & \dot{x}_f & \dot{z}_f & C - C_d \end{bmatrix}^T = \bar{0}, \quad (3.33)$$

$$DF(\bar{X}) = \begin{bmatrix} \phi_{21} & \phi_{23} & \phi_{25} & \dot{y}_f \\ \phi_{41} & \phi_{43} & \phi_{45} & \ddot{x}_f \\ \phi_{61} & \phi_{63} & \phi_{65} & \ddot{z}_f \\ 2x_0 - \frac{2(x_0+\mu)(1-\mu)}{d^3} - \frac{2\mu(x_0-1+\mu)}{r^3} & -\frac{2z_0(1-\mu)}{d^3} - \frac{2z_0\mu}{r^3} & -2\dot{y}_0 & 0 \end{bmatrix}. \quad (3.34)$$

The result of the targeting provides the initial state ($y_0 = \dot{x}_0 = \dot{z}_0 = 0$) and half of the propagation time for a periodic halo orbit.

Converged Halo Families

An initial guess for a halo orbit comes from one of the bifurcating orbits in a Lyapunov family. At $C \approx 3.174352$, the L_1 Lyapunov family has a tangent bifurcation where the L_1 halo family is formed. The pseudo-arclength method for generating an initial guess is employed as described above to obtain the initial guess for the initial state, propagation time, and Jacobi constant. With natural parameter continuation, more of the family is produced, appearing in Figure 3.7. Since the Lyapunov orbit bifurcates above and below the xy -plane, two halves of the family are formed. Figure 3.7 is denoted the L_1 northern halo orbits because most of each orbit is spent north (in the rotating frame) of the Moon. This method efficiently generates and extends the halo families.

Figure 3.8 provides the L_2 northern halo family, generated in the same way as the L_1 halo orbits but from the L_2 Lyapunov family. Note that these halo families are not monotonic in Jacobi constant. The stability indices for both families appear in Figure 3.9. L_3 halo orbits also exist, but are not utilized in this investigation. The halo families also provide valuable insight into cislunar dynamics, complementing the analysis of the Lyapunov families.

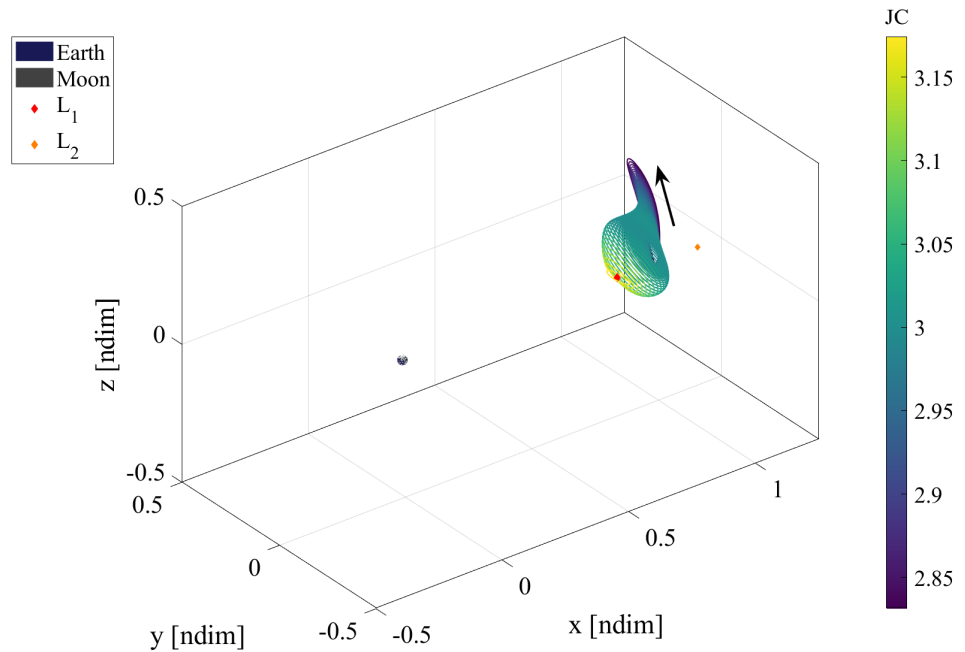


Figure 3.7. Earth-Moon L_1 northern halo orbit family.

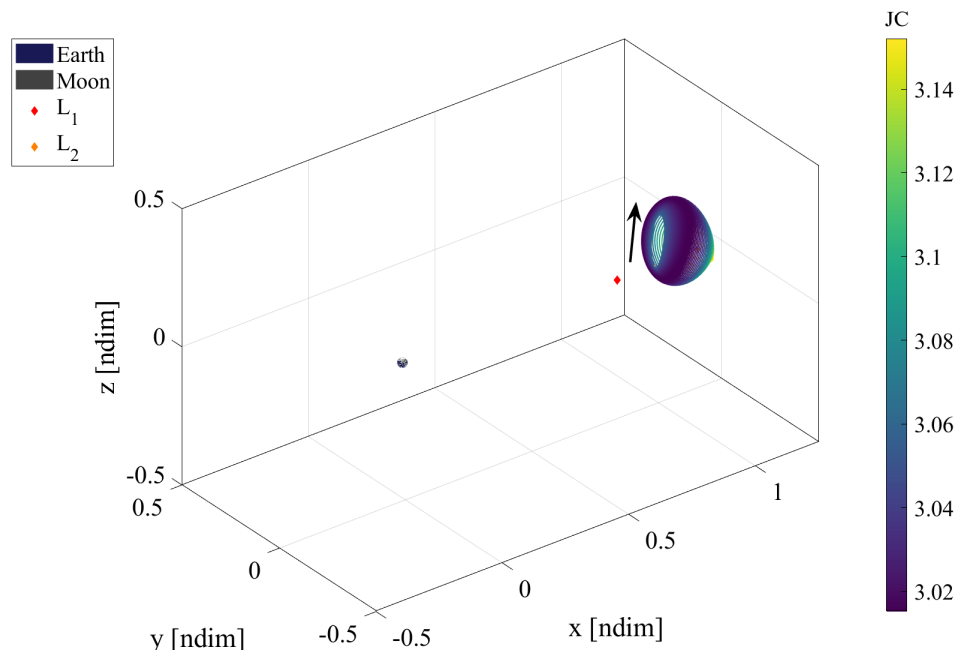


Figure 3.8. Earth-Moon L_2 northern halo orbit family.

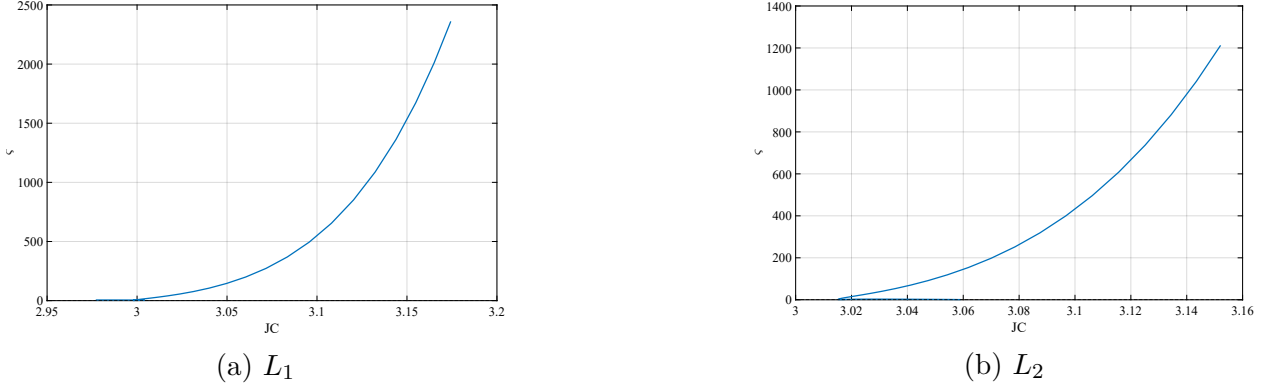


Figure 3.9. Earth-Moon Halo family stability index evolution.

3.2.4 Butterfly Orbits

Butterfly orbits is another name for the $P_2HO_1 L_2$ orbit family: the period-doubling bifurcation with the smallest perilune in the L_2 halo family[49]. Conveniently, the same targeter is applied for the butterfly family as with the halo orbits above. The same pseudo-arc length method is also applied to obtain the initial guess from the bifurcating halo orbit, remembering to double the period of the orbit first. Like the halo orbits, the butterfly family has a northern and southern half of the family, depending on the halo half-family that it bifurcates from. A portion of the southern family appears in Figure 3.10 and the stability indices appear in Figure 3.11. The butterfly orbits offer an extension of the halo family dynamics, showcasing bifurcation characteristics that enhance the understanding of the surrounding dynamics.

3.2.5 Axial Orbits

An Axial Targeter

Another spatial orbit family, the axial orbits, comes from a different tangent bifurcation in the Lyapunov families. These orbits have symmetry only about the x -axis; consequently, the perpendicular crossings must lie on the x -axis, unlike with the halo orbits:

$$\bar{X} = \begin{bmatrix} x_0 & \dot{y}_0 & \dot{z}_0 & \tau \end{bmatrix}^T, \quad (3.35)$$

$$\bar{F}(\bar{X}) = \begin{bmatrix} y_f & z_f & \dot{x}_f & C - C_d \end{bmatrix}^T = \bar{0}, \quad (3.36)$$

$$DF(\bar{X}) = \begin{bmatrix} \phi_{21} & \phi_{25} & \phi_{26} & \dot{y}_f \\ \phi_{31} & \phi_{35} & \phi_{36} & \dot{z}_f \\ \phi_{41} & \phi_{45} & \phi_{46} & \ddot{x}_f \\ 2x_0 - \frac{2(x_0 + \mu)(1 - \mu)}{d^3} - \frac{2\mu(x_0 - 1 + \mu)}{r^3} & -2\dot{y}_0 & -2\dot{z}_0 & 0 \end{bmatrix}. \quad (3.37)$$

The result of the targeting provides the initial state ($y_0 = z_0 = \dot{x}_0 = 0$) and half of the propagation time for a periodic axial orbit.

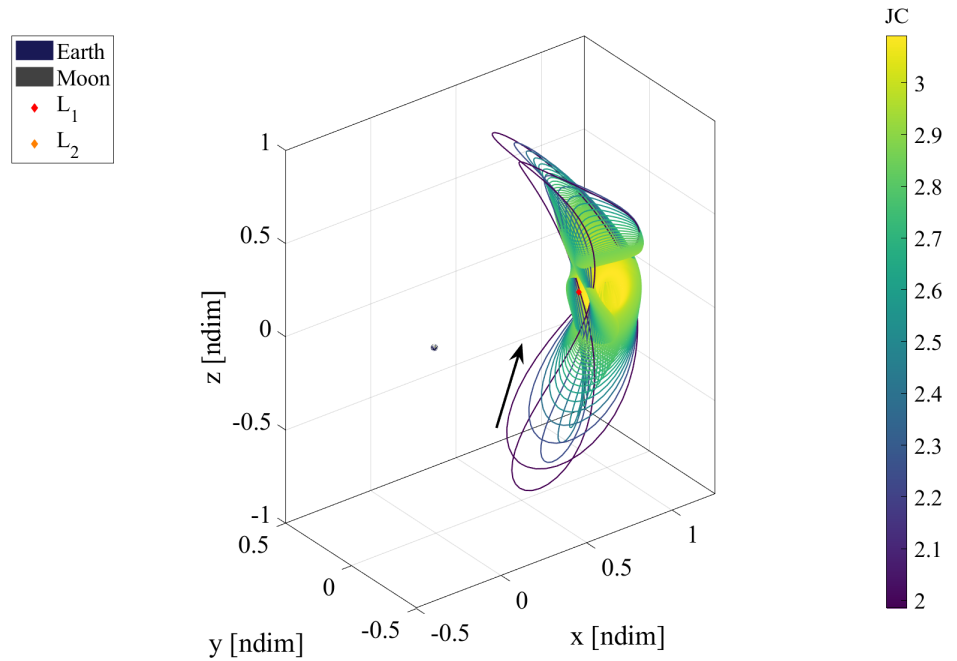


Figure 3.10. Earth-Moon southern butterfly family.

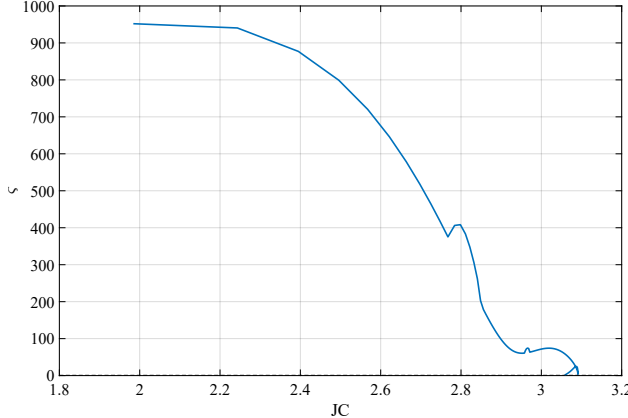


Figure 3.11. Earth-Moon butterfly family stability index evolution.

Converged Axial Families

From the methods employed to obtain the halo families, the L_1 and L_2 axial families are also obtained, appearing in Figure 3.12 and Figure 3.13, respectively. Similar to the halo orbits, two halves of the family are obtained by bifurcating above or below the xy -plane, making these the L_1 northwest and L_2 northeast axial families. Their stability indices follow in Figure 3.14. Again, there is an L_3 axial family, but it is not employed in this investigation. The axial families further enrich the dynamical framework explored in this investigation, exploiting the symmetry of the CR3BP dynamics.

3.2.6 Vertical Orbits

A Vertical Targeter

Vertical orbits benefit from double symmetry about both the xz - and xy -planes, allowing for targeting only a quarter of the orbit, with a perpendicular crossing of the xz -plane on one end of the arc and a perpendicular crossing of the x -axis on the other. Starting from the xz -plane crossing:

$$\bar{X} = \begin{bmatrix} x_0 & z_0 & \dot{y}_0 & \tau \end{bmatrix}^T, \quad (3.38)$$

$$\bar{F}(\bar{X}) = \begin{bmatrix} y_f & z_f & \dot{x}_f & C - C_d \end{bmatrix}^T = \bar{0}, \quad (3.39)$$

$$DF(\bar{X}) = \begin{bmatrix} \phi_{21} & \phi_{23} & \phi_{25} & \dot{y}_f \\ \phi_{31} & \phi_{33} & \phi_{35} & \dot{z}_f \\ \phi_{41} & \phi_{43} & \phi_{45} & \ddot{x}_f \\ 2x_0 - \frac{2(x_0+\mu)(1-\mu)}{d^3} - \frac{2\mu(x_0-1+\mu)}{r^3} & -\frac{2z_0(1-\mu)}{d^3} - \frac{2z_0\mu}{r^3} & -2\dot{y}_0 & 0 \end{bmatrix}. \quad (3.40)$$

The result of the targeting provides the initial state ($y_0 = \dot{x}_0 = \dot{z}_0 = 0$) at the perpendicular crossing of the xz -plane (top/bottom of the orbit) and one-quarter of the propagation time for a periodic vertical orbit.

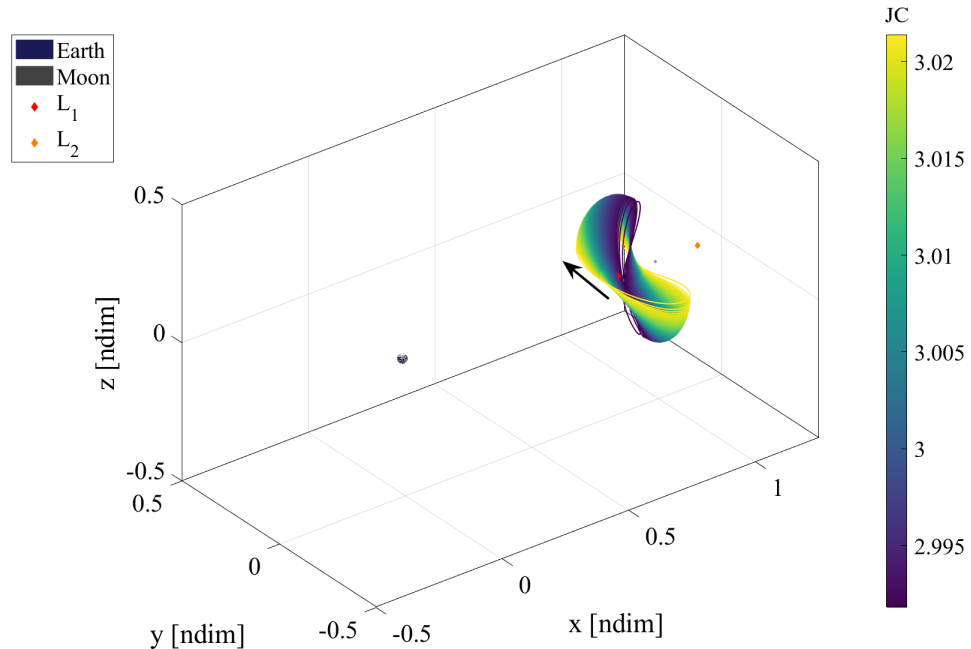


Figure 3.12. Earth-Moon L_1 northwest axial orbit family.

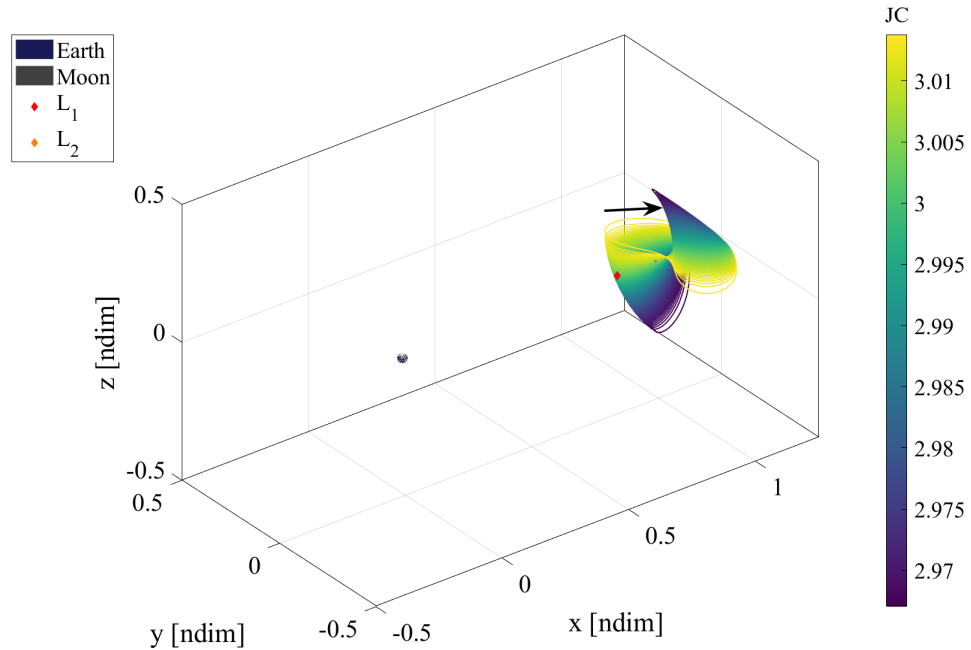


Figure 3.13. Earth-Moon L_2 northeast axial orbit family.

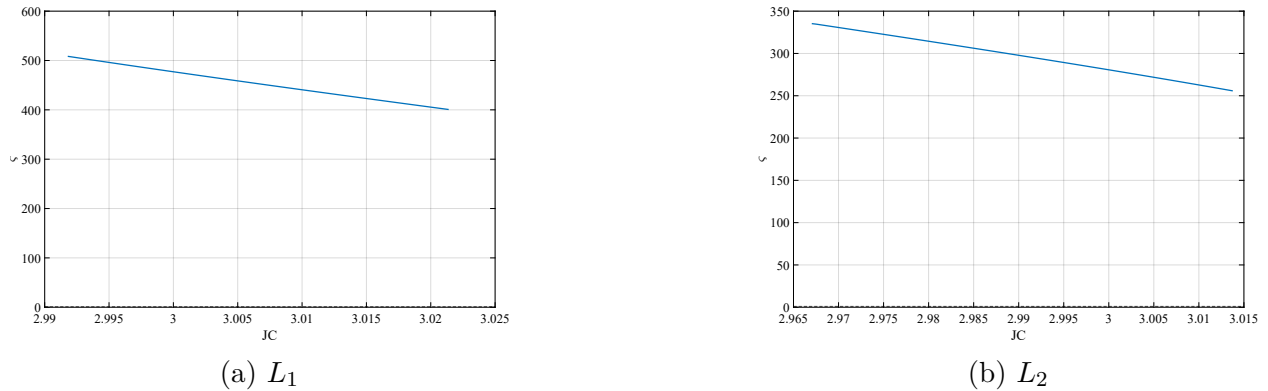


Figure 3.14. Earth-Moon axial family stability index evolution.

Converged Vertical Families

The vertical orbit family bifurcates from the end of the axial family where the axial orbit intersects itself and resembles a figure-eight. Stepping in one direction shrinks the orbits as the family collapses down to its origin at the Lagrange point. The other direction expands the orbits until they look like clam shells, demonstrated for the L_1 family in Figure 3.15.

Similar behavior occurs with the L_2 vertical family in Figure 3.16. Figure 3.17 provides the stability indices for these two families, while L_3 vertical orbits are not utilized in this investigation. The vertical families illustrate more of the diverse geometric orbit options near the Lagrange points, contributing to a broader understanding of the dynamical behavior of the system.

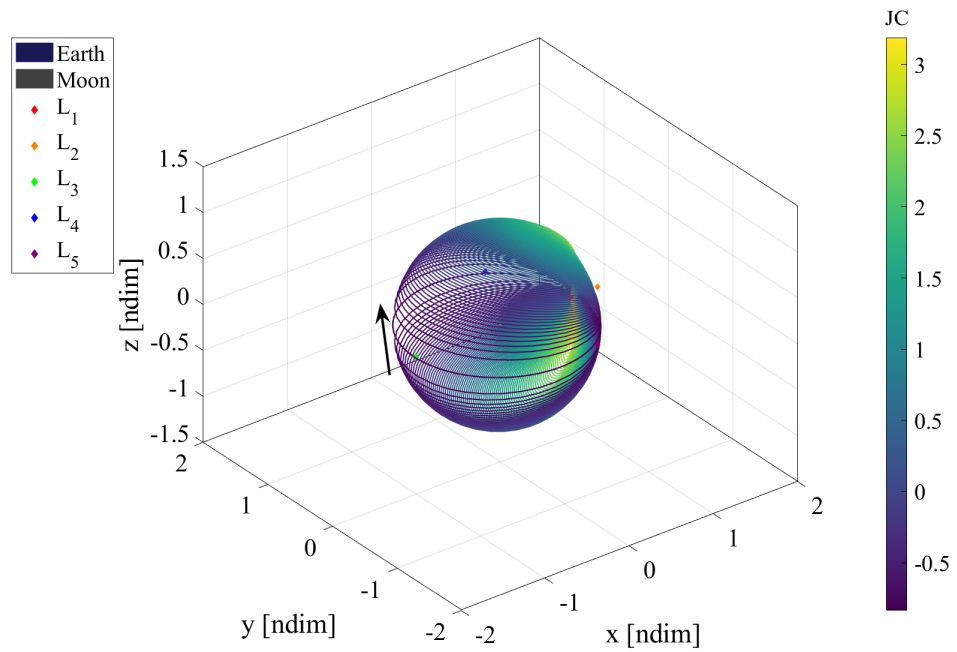


Figure 3.15. Earth-Moon L_1 vertical orbit family.

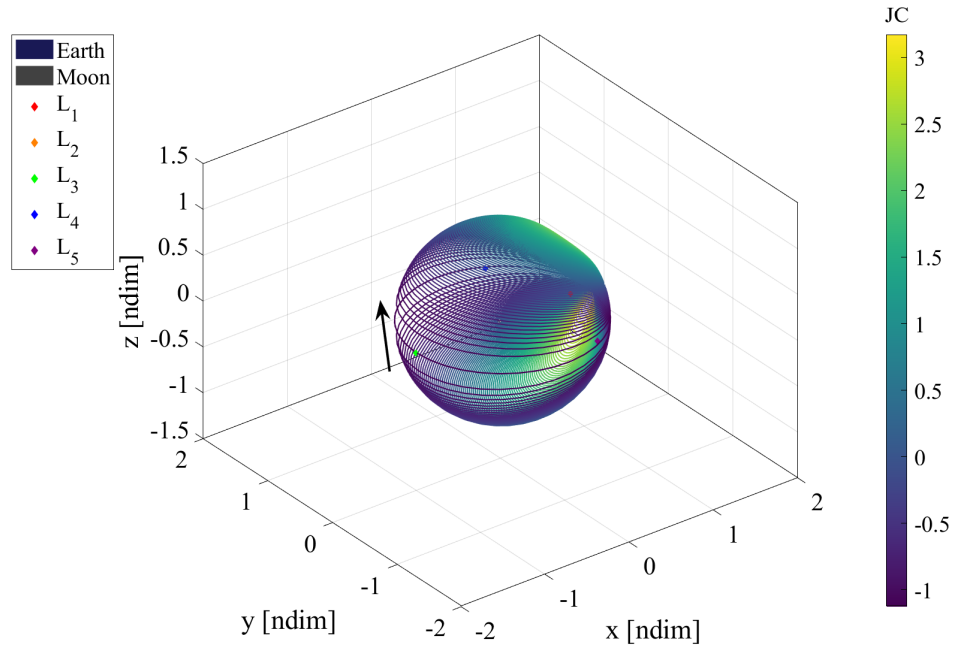


Figure 3.16. Earth-Moon L_2 vertical orbit family.

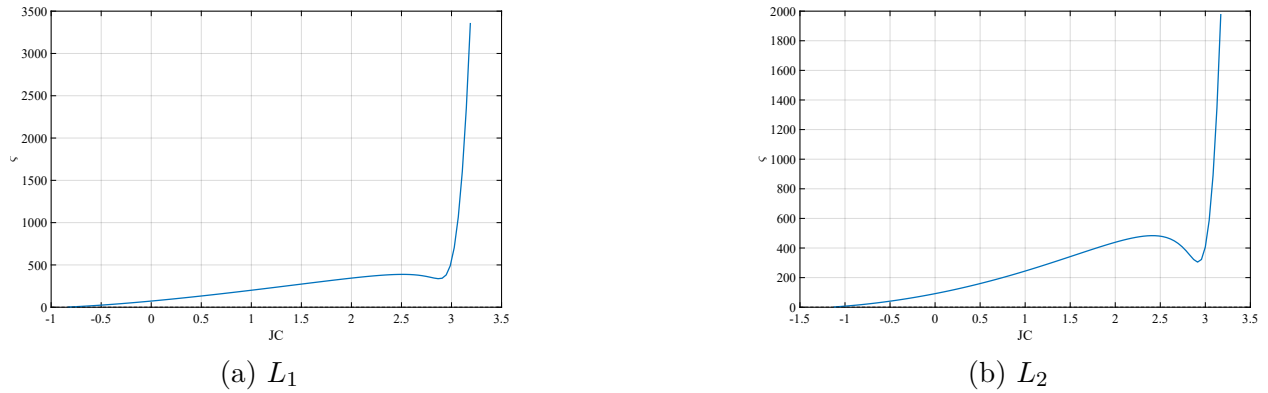


Figure 3.17. Earth-Moon vertical family stability index evolution.

3.3 Invariant Manifolds

Dynamically unstable periodic orbits in the CR3BP have valuable structures called invariant manifolds that represent a combination of the hyperbolic and oscillatory local flow near the orbit. With applications for transfer design, trajectories along these manifold sur-

faces asymptotically arrive at or depart from the periodic orbit ballistically. Perko provides the following theorem for stable/unstable manifolds for periodic orbits[51]:

Let $f \in C^1(E)$ where E is an open subset of R^n containing a periodic orbit,

$$\Gamma : \bar{x} = \gamma(t), \quad (3.41)$$

of $\dot{x} = f(\bar{x})$ of period T . Let ϕ_t be the flow of $\dot{x} = f(\bar{x})$ and $\gamma(t) = \phi_t(\bar{x}_0)$. If k of the characteristic exponents of $\gamma(t)$ have negative real part where $0 \leq k \leq n - 1$ and $n - k - 1$ of them have positive real part then there is a $\delta > 0$ such that the stable manifold of Γ ,

$$S(\Gamma) = \{\bar{x} \in N_\delta(\Gamma) | d(\phi_t(\bar{x}), \Gamma) \rightarrow 0 \text{ as } t \rightarrow \infty \text{ and } \phi_t(\bar{x}) \in N_\delta(\Gamma) \text{ for } t \geq 0\}, \quad (3.42)$$

is a $(k + 1)$ -dimensional, differentiable manifold that is positively invariant under the flow ϕ_t and the unstable manifold of Γ ,

$$U(\Gamma) = \{\bar{x} \in N_\delta(\Gamma) | d(\phi_t(\bar{x}), \Gamma) \rightarrow 0 \text{ as } t \rightarrow -\infty \text{ and } \phi_t(\bar{x}) \in N_\delta(\Gamma) \text{ for } t \leq 0\}, \quad (3.43)$$

is an $(n - k)$ -dimensional, differentiable manifold that is negatively invariant under the flow ϕ_t . Furthermore, the stable and unstable manifolds of Γ intersect transversally in Γ .

In layman's terms, if a periodic orbit is unstable (it has eigenvalues with magnitudes greater than and lesser than 1), then stable/unstable manifold surfaces exist that approach/leave the orbit asymptotically.

3.3.1 Approximating a Manifold Arc

Numerical methods are essential for approximating stable and unstable manifold arcs of periodic orbits. Since invariant manifold structures naturally depart the periodic solution asymptotically, a deterministic maneuver is not required to transfer onto them from the

orbit. However, a consequence of the asymptotic behavior is that it is not trivial to identify the exact location along the orbit from where a manifold trajectory departs. Consequently, a numerical process is necessary to approximate the stable/unstable subspaces of the orbit to determine an appropriate initial condition for an arc along the manifold surface.

Near the periodic orbit, the manifolds are tangent to their corresponding eigenspaces of the orbit. For a selected point on the periodic orbit:

$$\bar{\nu}(t_0 + t) = \Phi(t_0 + t, t_0)\bar{\nu}(t_0), \quad (3.44)$$

where $\bar{\nu}(t_0)$ is the eigenvector at the initial condition corresponding to the stable or unstable eigenvalue of the monodromy matrix. Once the stable/unstable eigenvector at the selected point is obtained:

$$\bar{\nu}_n = \frac{\bar{\nu}}{\sqrt{\nu_x^2 + \nu_y^2 + \nu_z^2}}, \quad (3.45)$$

where ν_x is the x -component of the eigenvector and $\bar{\nu}_n$ is the eigenvector normalized by the nondimensional distance from the selected point. Utilizing the normalized stable eigenvector to approximate the initial condition for a stable manifold arc:

$$\bar{q}^S = \bar{q}^\Gamma \pm d\bar{\nu}_n^S, \quad (3.46)$$

where \bar{q}^Γ is the state vector at the selected point along the periodic orbit and d is a step-off distance, generally selected based on the specific CR3BP system. The scaled eigenvector is either added to or subtracted from the periodic state as the eigenspace is bi-directional, creating two half-manifolds for each stability. To compute an initial condition for an unstable manifold arc, employ Equation (3.44)-Equation (3.46), replacing the stable components for unstable ones. Stable manifold arcs are then propagated backward in time from the initial condition (arriving at the orbit in forward time) while unstable arcs are propagated forward in time from their initial condition. This step-off approach enables the approximation of initial conditions for invariant manifold arcs, facilitating their propagation in the CR3BP.

As mentioned, the step-off value d depends on the CR3BP system. The step-off parameter needs to be sufficiently small to approximate the manifold structure well. However, if d is

too small, the trajectory takes longer than reasonable to arrive at/depart from the orbit since the dynamics are asymptotic[38]. Table 3.1 provides the values of d employed for the systems in this investigation. As some examples of manifold structures, Figure 3.18 and Figure 3.19 illustrate the stable and unstable manifolds for a planar Lyapunov orbit and a spatial halo orbit, respectively, in the Earth-Moon system. Each figure also provides a single manifold arc overlayed on the full structure for reference. A more thorough explanation of manifold theory is found in Perko[51]. These examples illustrate how appropriate selection of the step-off value ensures accurate representation of the manifold structures.

Table 3.1. Manifold-related values of relevant CR3BP systems.

CR3BP System	d [km]	ΔMI Threshold
Earth-Moon	25	1×10^{-3}
Sun-Earth	1000	5×10^{-5}
Sun-Mars	1000	1×10^{-5}

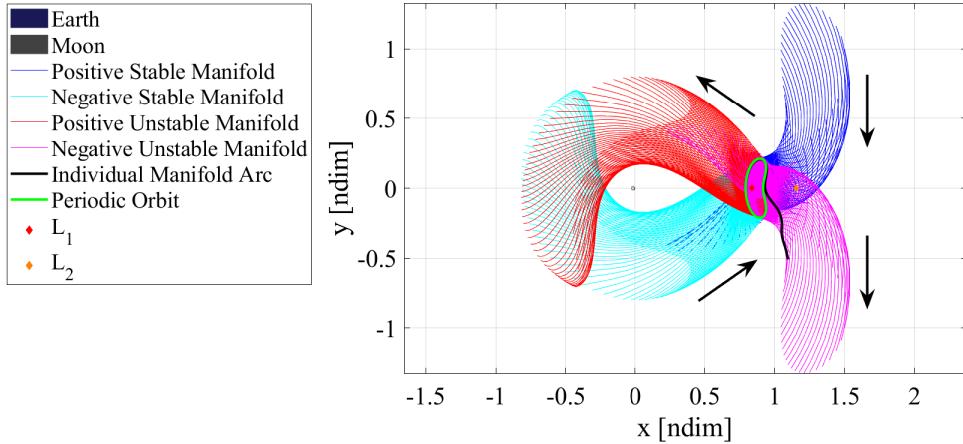


Figure 3.18. Earth-Moon L_1 Lyapunov Manifolds ($C = 3.05$).

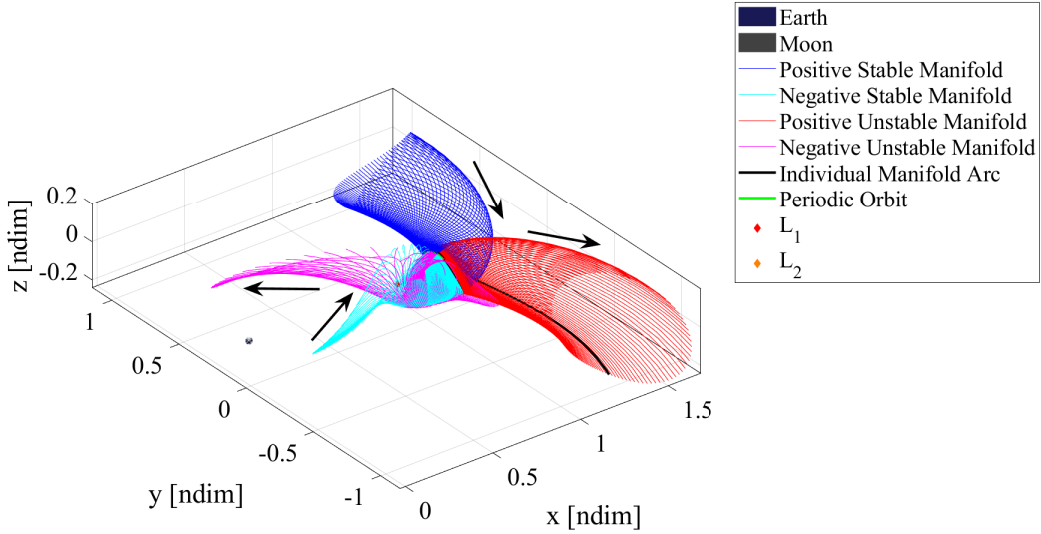


Figure 3.19. Earth-Moon L_2 Halo Manifolds ($C = 3.08$).

3.3.2 Manifold Time-of-Flight

Since manifolds asymptotically arrive at/depart from their orbit, even with a reasonable step-off distance, they take a long time to depart from the orbit vicinity. Under higher-fidelity dynamics, the period of time spent near the orbit is often absorbed by the dynamics, so it is beneficial to have a metric to determine when the manifold has departed the orbit vicinity. In this investigation, the momentum integral, or more specifically the momentum integral difference, is employed to indicate orbit departure:

$$MI = \int_{t_0}^t (x\dot{x} + y\dot{y} + z\dot{z}) d\tau, \quad (3.47)$$

where all of the values are nondimensional. Starting from $MI_0 = 0$ at the step-off location, the momentum integral is calculated for both the orbit and the manifold arc and the difference between the two values measures the similarity of the two trajectories:

$$\Delta MI = |MI - MI^\Gamma|. \quad (3.48)$$

Once ΔMI has reached a threshold value (determined for each system), the trajectory is considered departed from the orbit[52]. Consequently, the time it takes for the manifold to depart is subtracted from the time-of-flight along the manifold arc starting from the step-off. Table 3.1 provides the threshold values selected for each system in this investigation. The momentum integral difference approach ensures consistent identification of manifold departure, enabling accurate trajectory modeling under different dynamics.

3.4 Poincaré Maps

Since plots of invariant manifolds in configuration space can be complex and do not display any velocity information about the trajectories, a different visualization technique is advantageous. Poincaré mapping is an approach that concisely visualizes trajectories by reducing the dimension of the problem through an intersection surface. These surfaces can be physical, like a plane or sphere in configuration space, or more abstract, like an apse or velocity map. As initial conditions are propagated, whenever a trajectory passes through the surface, its crossing is marked on the Poincaré map. A simple example appears in Figure 3.20. The mapping technique provides an intuitive representation of complex trajectory behaviors, aiding in the analysis and interpretation of manifold dynamics.

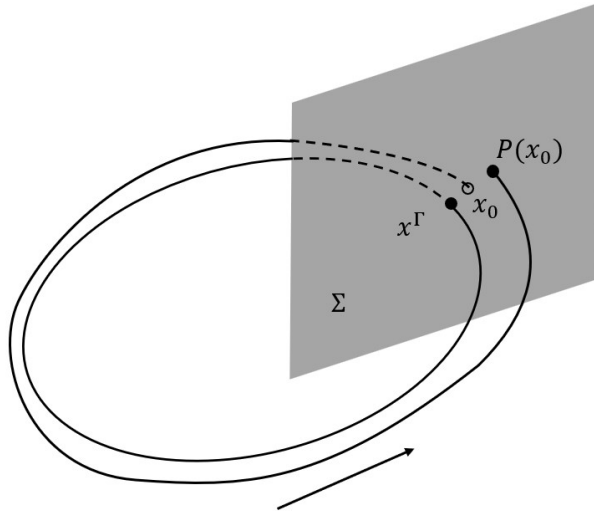


Figure 3.20. Poincaré map.

Poincaré mapping provides a powerful method for visualizing and analyzing trajectory behavior by reducing the dimensionality of the problem through surface intersections. Starting from an initial condition x_0 on the intersection surface Σ , after propagation, the trajectory returns to the surface at $P(x_0)$. If the trajectory is precisely periodic, the trajectory returns to the same point, x^Γ . The Poincaré map then is the 2-dimensional representation of the surface, displaying only the trajectory crossings. Note that the axes of the map need not be position components but could also be velocity, energy, etc. Similar mappings are employed in this investigation to more efficiently analyze and compare different trajectories.

4. CISLUNAR-MARS TRAJECTORY CONSTRUCTION

Many of the techniques introduced in the previous chapter are employed in this investigation to design end-to-end transfers between orbits in the Earth-Moon and Sun-Mars CR3BP systems. Two categories of transfers are designed and compared: trajectories that include an intermediate Sun-Earth staging halo orbit and those that do not. For the transfers utilizing a staging orbit, a strategy is adapted from Kakoi to compute near-ballistic transfer solutions between Earth-Moon unstable orbits and Sun-Earth halos via invariant manifolds[38]. Both sets of transfers then utilize a variation of the moon-to-moon analytical transfer methodology developed by Canales to bridge the gap between the Sun-Earth trajectories (either Sun-Earth manifolds or Earth-Moon manifolds propagated under Sun-Earth dynamics) and the Sun-Mars manifolds[37]. Note that the transfer design process does not result in optimized interplanetary transfers, but instead provides families of low-energy solutions to facilitate the comparison between cislunar departure orbits. As a baseline comparison metric, a Keplerian Hohmann transfer with a built-in plane change is also introduced here to represent the current standard for non-coplanar direct Earth-Mars transfers. The methods introduced here establish a framework for creating low-energy interplanetary transfer trajectories.

4.1 Near-Ballistic Transfers between the Earth-Moon and Sun-Earth Systems

While both categories of trajectories travel through the Sun-Earth CR3BP region, only those with an intermediate staging orbit have a constrained path. For the staging orbit trajectories, the Earth-Moon unstable manifold arc, propagated under the Sun-Earth CR3BP dynamics once it reaches the lunar sphere of influence, must intersect with a stable manifold arc from the Sun-Earth staging L_2 halo orbit. An unstable manifold arc from the staging orbit is then utilized to depart the Sun-Earth system (compared to the more direct transfer type that employs the Earth-Moon manifold to depart the system). Kakoi developed a design methodology for maneuver-free transfers between orbits in the two systems, treating them as non-coplanar, where the required respective initial orientations of the three bodies (the Sun, Earth, and Moon) are represented by two angles and the interface between the CR3BP systems occurs at the intersection of the manifold arcs[25], [38]. Parker and

Anderson developed a similar approach utilizing the Sun-Earth stable and unstable manifolds to design low-energy transfers between Earth and lunar libration orbits[45]. The two previous methodologies inspire the approach employed in this investigation, where the orientations are determined by a specified epoch date and the two systems interface before the arc intersection.

4.1.1 Methodology

To find a connection between the orbits in the two different CR3BP systems, discretized arcs of the manifold surface of the Earth-Moon departure orbit are propagated to the SoI of the Moon, as defined in Equation (2.46). At the SoI distance from the Moon, its gravitational influence becomes negligible compared to those of the Earth and the Sun. At the interface of the two CR3BP systems, the Earth-Moon barycentric rotating frame state of each arc is transformed to a Sun-Earth barycentric rotating frame state by rotation to the Earth-centered Ecliptic J2000 frame and back as described in Section 2.5. The rotation depends on the epoch date when the state reaches the SoI, determining the relative orientations of the celestial bodies. While the orientations change slightly month-to-month due to the different planes, the transfer characteristics tend to repeat each month, so this investigation only analyzes transfers that depart during January 2026[45]. Note that although the SoI intersection states all have the same Earth-Moon Jacobi constant values, now that they are in the Sun-Earth system, their Sun-Earth Jacobi constant values vary. Since the new values remain constant as the states are now propagated with the Sun-Earth CR3BP equations of motion, it is necessary that the Jacobi constant of the Sun-Earth staging halo orbit lies within that range of Jacobi constant values. The process ensures that the manifold arcs are seamlessly transitioned between the Earth-Moon and Sun-Earth CR3BP systems for consistent trajectory analysis.

The manifold arcs are now propagated until they reach the manifold intersection surface, selected as an angle measured from the x -axis in the Sun-Earth rotating frame, centered at the Earth, that extends as a plane perpendicular to the xy -plane. According to Kakoi, plane angles between -85° and 70° are desirable for transfers between Earth-Moon L_2 and Sun-

Earth L_2 orbits[38]. In the Earth-centered Sun-Earth rotating frame, the stable manifolds from the Sun-Earth L_2 halo orbits utilized in this investigation arrive in the Earth-Moon vicinity in the fourth quadrant (southeast) that encompasses that range of angles. A plane angle of -80° is selected for this investigation. At the same time, the discretized stable manifold surface from the Sun-Earth L_2 halo orbit is propagated to the same plane, appearing in Figure 4.1. The approach ensures that the manifold arcs from both CR3BP systems align at a common intersection surface, facilitating the identification of potential transfers.

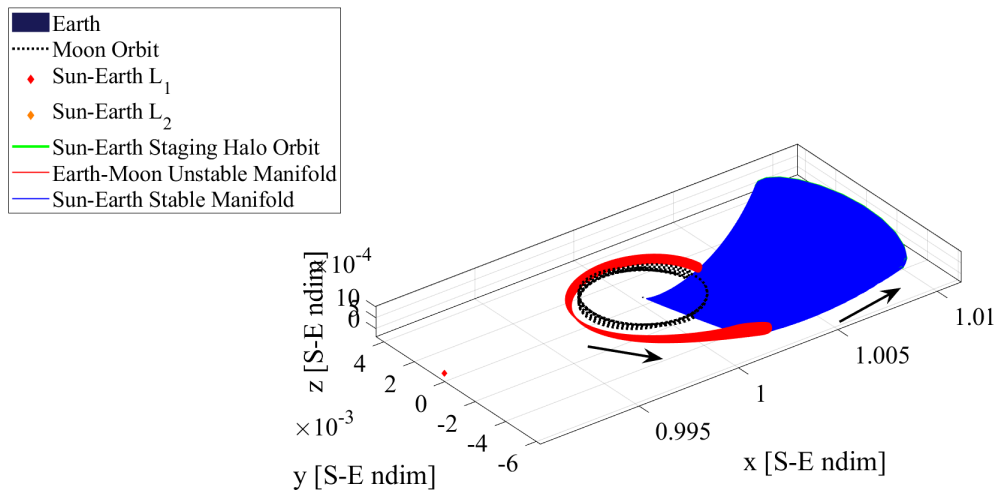


Figure 4.1. Earth-Moon and Sun-Earth manifolds at the intersection surface in the Sun-Earth rotating frame.

At the intersection surface, mappings of both manifolds are applied to form phase plots that inform the transfer initial guess selection. Following Kakoi's approach, the plots represent \dot{x} vs. x , z vs. x , and \dot{z} vs. z . The y -value is defined by the x -value and the intersection surface angle, while the \dot{y} -value is determined by the Jacobi constant[38]. A black dot along the Earth-Moon manifold curve denotes the arc that matches the Sun-Earth manifold in Jacobi constant. The two sets of manifold arcs form curves on the plots and the goal is to find an intersection between the curves that occurs at the black point in all three phase plots

simultaneously. Figure 4.2 provides an example of the phase plots, where the red curve is the unstable Earth-Moon manifold arcs and the blue curve is the stable Sun-Earth manifold arcs. Note that there are two black markers representing two individual arcs that match the Sun-Earth Jacobi constant. The phase plots provide a clear visualization of potential transfer connections and serve as a critical tool for identifying initial guesses that satisfy the required dynamical conditions.

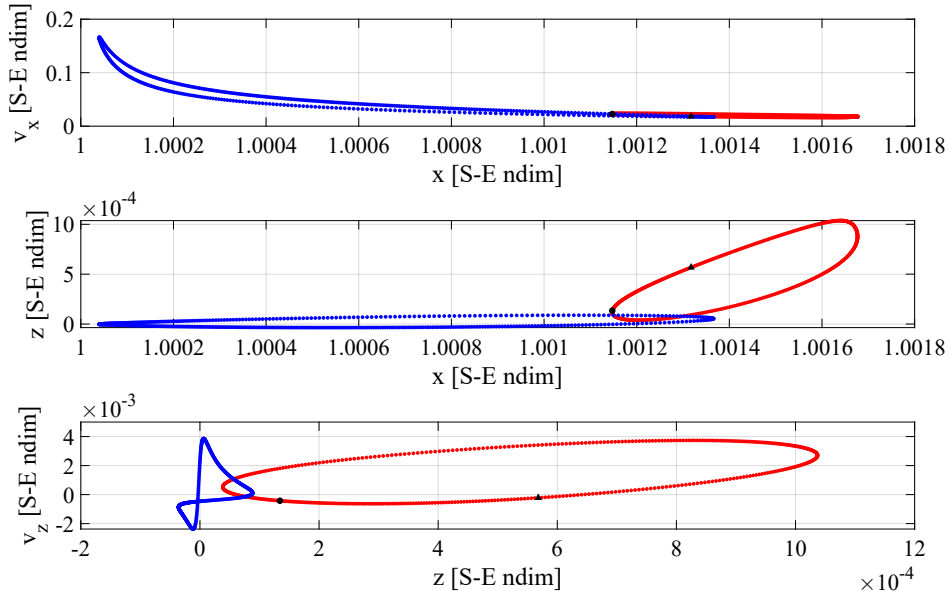


Figure 4.2. The intersection surface phase plots for Figure 4.1.

The initial epoch of the Earth-Moon manifold departure, the intersection surface angle, and the Sun-Earth halo orbit Jacobi constant are all varied to shift the curves on the phase plots and find an intersection; Kakoi provides some guidelines for doing so[38]. Once a suitable point is determined, like the black circle marker in Figure 4.3, the resulting information is utilized to generate an initial guess for the transfer between the systems, appearing in Figure 4.4. The initial guess is then corrected to find a position intersection (a maneuver is allowed at the intersection) employing an iterative Newton-Raphson scheme:

$$\bar{X} = \begin{bmatrix} T_0 & \tau_1 & t_1 & \tau_2 & t_2 \end{bmatrix}^T, \quad (4.1)$$

$$\bar{F}(\bar{X}) = \begin{bmatrix} \bar{r}_2 - \bar{r}_1 & \|\bar{v}_2 - \bar{v}_1\| \end{bmatrix}^T. \quad (4.2)$$

where T_0 is the initial epoch, τ_1 and τ_2 are the phase along the Earth-Moon and Sun-Earth orbits where the manifold steps-off, respectively, t_1 and t_2 are the times-of-flight along each manifold arc, \bar{r}_1 and \bar{r}_2 are the manifold arc positions at the end of the propagation, and \bar{v}_1 and \bar{v}_2 are the velocity vectors at those points, respectively. The central difference method from Section 3.1 is applied to determine the DF Jacobian matrix. Note that the magnitude of the maneuver is included as the second constraint in the targeting problem. For the first implementation of the targeter, the Δv of the initial guess is the constraint value. Then, each time a solution is converged, the constraint value is decreased and the targeting problem is repeated to find a near-ballistic solution with a local minimum in Δv . Also note that during the process, the intersection location of the two manifold arcs is free to shift from the designated intersection surface. The result of the process is a near-ballistic transfer between an Earth-Moon orbit and a Sun-Earth halo orbit utilizing their invariant manifolds. The transfers have low maneuver costs that are often absorbed by the dynamics once the solution is transferred to a higher-fidelity dynamical model. The iterative process ensures the generation of efficient transfer trajectories with minimal Δv , serving as a robust foundation for preliminary transfer design.

4.1.2 Example

As an example, consider the phase plots in Figure 4.3 and the resulting initial guess in Figure 4.4. The unstable manifold arc departs from an Earth-Moon L_2 northern halo orbit with an Earth-Moon Jacobi constant of 3.13 on January 2, 2026 at 07:12:00, while the stable manifold arc arrives at a Sun-Earth northern halo orbit with a Sun-Earth Jacobi constant of 3.0008189. At the intersection surface, the two arcs have a position discontinuity of 8.768×10^{-6} Sun-Earth nondimensional units (1312 km) and a Δv of 57.4 m/s. The iterative corrections process outlined above produces a position continuous trajectory with a Δv of 14.6 m/s, a negligible amount in comparison to the rest of the end-to-end transfer. The initial departure epoch has also shifted slightly, to January 2, 2026 at 07:32:35. The corrected trajectory appears in Figure 4.5. Note that the location of the maneuver has

shifted from the defined intersection surface to earlier along the Earth-Moon manifold arc. While this exact solution is only available for the given epoch, every month a similar solution presents itself, so this represents potential near-ballistic transfer solutions in every month. The example highlights the effectiveness of the iterative corrections process in refining initial guesses into near-ballistic transfer solutions.

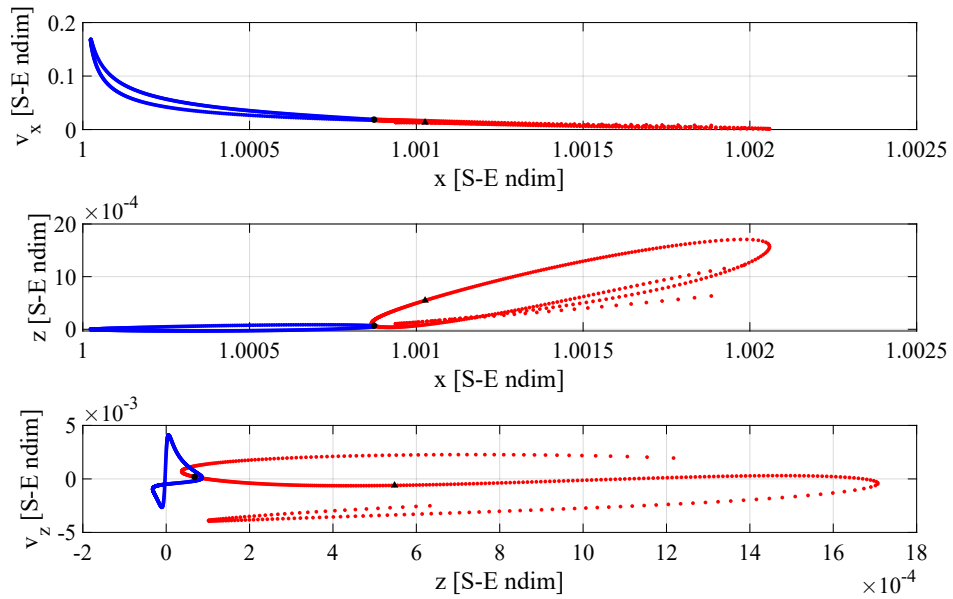


Figure 4.3. Intersection surface phase plots with a near intersection after varying the parameters.

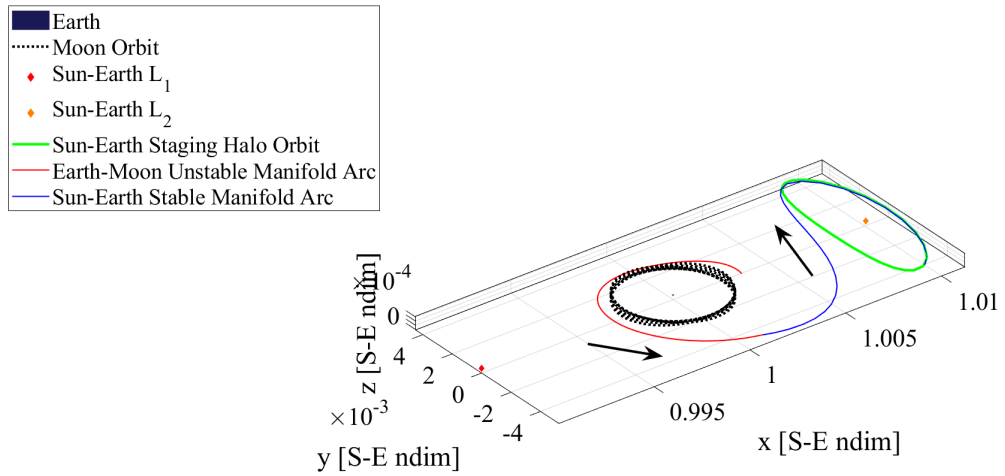


Figure 4.4. Initial guess for near-ballistic Earth-Moon to Sun-Earth transfer from phase plots in the Sun-Earth rotating frame.

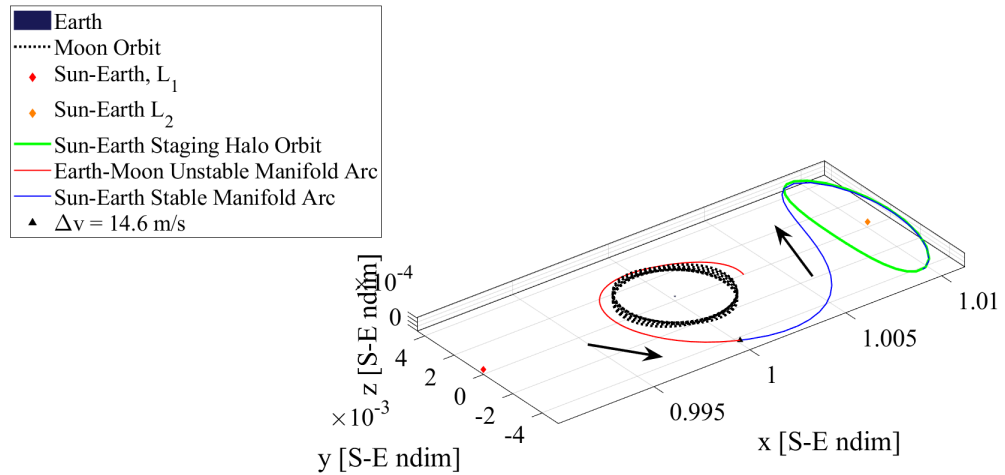


Figure 4.5. Converged near-ballistic tranfer between Earth-Moon and Sun-Earth halo orbits in the Sun-Earth rotating frame.

4.2 The Moon-to-Moon Analytical Transfer Method

The MMAT method was created to design tours between the moons of a planet such as Jupiter or Saturn. However, Canales also demonstrated that it can be similarly applied to interplanetary transfers by treating the planets as "moons" of the Sun. He provides detailed derivations, analyses, and examples of the basic MMAT strategy, as well as some extensions relevant to this investigation[28], [29], [37]. More specifically, the end-to-end cislunar-Mars transfer methodology presented here employs a distant, two-burn MMAT with a plane change, bridging the gap between manifolds of Sun-planet CR3BP systems and the true inclinations of the planetary orbital planes.

4.2.1 Methodology

First, a departure and an arrival CR3BP manifold arc are needed. In this investigation, the departure CR3BP arc is either a Sun-Earth halo orbit unstable manifold arc or an Earth-Moon orbit unstable manifold arc propagated within the Sun-Earth dynamics, depending on the transfer category. Either the departure epoch or the selected manifold arc are varied to determine the departure CR3BP arc. The arrival CR3BP arc is a Sun-Mars halo orbit stable manifold trajectory. Since an interplanetary transfer from Earth to Mars is an outward journey, to minimize the Δv of the MMAT solution, the Sun-Mars stable manifold arc with the smallest periapsis (relative to the Sun) is utilized[37]. For an inward journey, say to Venus, the manifold with the largest apoapsis is selected, minimizing the Keplerian angular momentum and energy difference between the departure and arrival CR3BP arcs. The selection process ensures that the departure and arrival manifold arcs minimize the transfer cost and achieve efficient interplanetary trajectories.

The arcs are propagated under the CR3BP dynamics until they reach a specified distance from their smaller primary (Earth or Mars), their sphere of influence. Various definitions exist, but for the MMAT method, the SoI radius is defined as the distance where the ratio of the gravitational accelerations of the two primaries d_{SoI} is equal to a selected small quantity (see Equation (2.45))[37]. To ensure that the SoI encompasses most of the Lyapunov orbit family but also accurately represents when the gravitational effects of that body can be

neglected, the values of d_{SoI} in Table 4.1 are selected, resulting in their corresponding radii. Canales provides more details on selecting of appropriate values for d_{SoI} [37].

Table 4.1. MMAT sphere of influence radii of relevant CR3BP systems.

CR3BP System	d_{SoI}	r_{SoI}
Sun-Earth	2.5×10^{-4}	0.09877
Sun-Mars	1×10^{-4}	0.05375

Once the CR3BP manifold arc has reached the edge of the SoI, it is treated as a 2BP trajectory with the Sun as its focus (refer to the patched 2BP-CR3BP model introduced in Section 2.4). The barycentric rotating frame state that intersects the SoI is transformed to the heliocentric Ecliptic J2000 frame state applying the procedure outlined in Section 2.5. The resulting state now defines a Keplerian heliocentric ellipse in the instantaneous plane of motion of the trajectory at the SoI intersection, the continued path for either the departure or arrival conic arc. Equation (2.13)-Equation (2.21) are applied to retrieve the equivalent Keplerian orbital elements. The Keplerian elements fully characterize the heliocentric behavior of the trajectory, serving as a critical step in connecting the CR3BP manifold dynamics to the interplanetary transfer framework.

In the distant, two-burn MMAT strategy, for an outward journey, the first maneuver is placed at the periapsis of the departure conic. Given the true anomaly $\theta = 0$ at periapsis, Equation (2.22)-Equation (2.28) are applied to compute the inertial state at periapsis while Equation (2.29) and Equation (2.30) are employed to compute the time-of-flight along the departure conic:

$$TOF_d = \mathbb{P}_d - (t - t_p), \quad (4.3)$$

where \mathbb{P}_d is the period of the departure conic and $(t - t_p)$ is the time since periapsis of the SoI state. An inward journey departs from the apoapsis of the departure conic. The approach aligns the departure conic with the interplanetary bridging trajectory at minimum fuel cost.

As mentioned previously, a bridge arc is needed to connect the departure and arrival conic arcs, with a maneuver at both ends. The distant, two-burn MMAT bridge arc for

an outward transfer has the same periapsis radius as the departure conic arc and the same apoapsis as the arrival conic arc (and vice versa for an inward transfer). The values form a ratio that is utilized to compute the semimajor axis and eccentricity of the bridge conic:

$$\mathcal{P}_b = \frac{r_{p_b}}{r_{a_b}} = \frac{1 - e_b}{1 + e_b}, \quad (4.4)$$

$$e_b = \frac{1 - \mathcal{P}_b}{1 + \mathcal{P}_b}, \quad (4.5)$$

$$a_b = \frac{r_{p_b}}{1 - e_b}. \quad (4.6)$$

For an outward journey, the bridge arc lies in the same plane as the departure conic arc, since Keplerian inclination changes are more efficient the further away they are from the primary, implying that the remaining three angles of the bridge conic (i , Ω , ω) are identical to those of the departure conic. Since only the semimajor axis and eccentricity change between the departure and bridge conics, the first maneuver is tangential to the motion at periapsis, only changing the energy, and is calculated by the difference in the velocity states at the periapsis. An inward journey combines the inclination change with the first maneuver, so the bridge conic lies in the same plane as the arrival conic. The following methodology is similar for the inward case but flipped so that the constraints are on the intersection between the departure and bridge conic arcs. The associated equations are also slightly different since the transfer geometry is flipped. The construction of the bridge arc ensures a smooth and efficient transition between the departure and arrival conics.

The non-coplanar MMAT methodology revolves around the following analytical constraint derived by Canales[37]:

As long as the geometrical properties of two conics located in different planes fulfill the inequality constraint represented by

$$a_a(1 - e_a) \leq \frac{a_b(1 - e_b^2)}{1 + e_b \cos(\theta_{b_{int}} + n\pi)} \leq a_a(1 + e_a), \text{ being } n = 0, 1, \quad (4.7)$$

either one of the two conics can be reoriented such that they intersect in space. Consequently, the ideal phase of the arrival [planet] at arrival, $\theta_{5_{Mars}}$, for the moon-to-moon transfer to occur is obtained considering that the departure epoch, $\theta_{0_{Earth}}$, is fixed.

In the constraint, $\theta_{5_{Mars}}$ and $\theta_{0_{Earth}}$ correspond to T_0 and T_5 in Figure 4.6. The figure is a schematic of the distant, two-burn MMAT transfer with a plane change, where the departure and bridge conics are on the same plane but the arrival conic is not. With the semimajor axes and eccentricities of the bridge and arrival arcs already determined, the only value still needed for Equation (4.7) is $\theta_{b_{int}}$, the bridge conic true anomaly at the intersection location between the bridge and arrival conics (T_3 in Figure 4.6):

$$\theta_{b_{int}} = u_b - \omega_b, \quad (4.8)$$

$$\sin u_b = \frac{\sin(\pi - i_a) \sin \Delta\Omega}{\sin \psi}, \quad (4.9)$$

$$\cos u_b = \frac{\frac{\sin i_a \cos \Delta\Omega}{\cos i_b} - \cos \psi \tan i_b}{\sin \psi}, \quad (4.10)$$

$$\cos \psi = \cos i_a \cos i_b + \sin i_a \sin i_b \cos \Delta\Omega, \quad (4.11)$$

where $\Delta\Omega = \Omega_a - \Omega_b$. Note that the value of n that satisfies the inequality defines the orientation of the bridge conic and is needed later to properly orient the arrival conic. The center of the inequality in Equation (4.7) is the intersection distance from the Sun:

$$r_{int} = \frac{a_b(1 - e_b^2)}{1 + e_b \cos(\theta_{b_{int}} + n\pi)} = \frac{a_a(1 - e_a^2)}{1 + e_a \cos(\theta_{a_{int}} + o\pi)}, \text{ being } o = 0, 1. \quad (4.12)$$

Unfortunately, if the arrival conic arc is not in the same plane as the orbital plane of the arrival planet, i_a and Ω_a cannot be determined prior to the MMAT phasing. As a result, the arrival phasing needs to be iteratively targeted, making the approach only semi-analytical.

For an initial guess to check the MMAT constraint in Equation (4.7), the inclination and RAAN of the arrival planet orbital plane are selected. The methodology establishes the foundation for accurately phasing the arrival trajectory in the non-coplanar MMAT framework, though it requires iterative refinement due to the complexity of aligning orbital planes.

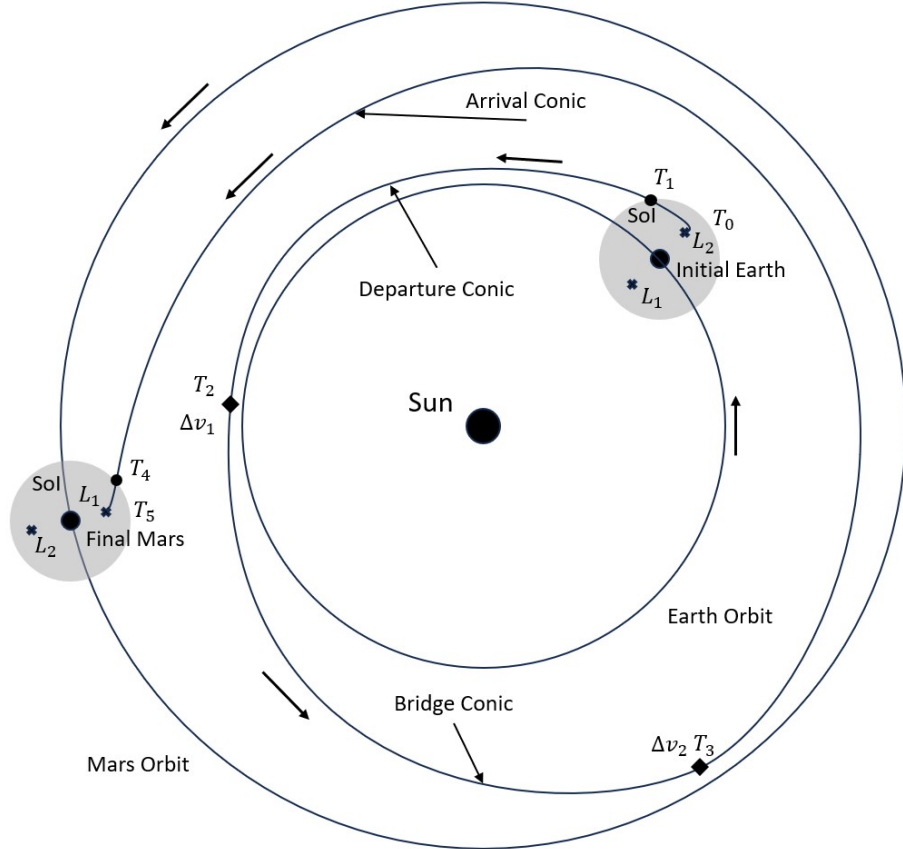


Figure 4.6. Representation of the distant, two-burn MMAT with a plane change (adapted from Canales[37]).

The arrival conic true anomaly at the intersection is computed similarly from r_{int} , with the caveat that it is dependent on the arrival phasing and needs to be targeted:

$$\theta_{a_{int}} = 2\pi o + (-1)^o \arccos\left(\frac{\frac{a_a(1-e_a^2)}{r_{int}} - 1}{e_a}\right), \text{ being } o = 0, 1. \quad (4.13)$$

For every feasible $\theta_{b_{int}}$, there are then two possible phasing solutions ($\theta_{a_{int}}$) that correspond to the two arrival ellipse orientations (ω_a) that intersect the bridge ellipse at the line of nodes.

A schematic representing the two orientations appears in Figure 4.7, where the dashed part of the ellipses are under the XY -plane and the arrows indicate the direction of motion along each ellipse. The angles for the orientation are calculated similarly to before:

$$\omega_a = u_a - (\theta_{a_{int}} + n\pi), \quad (4.14)$$

$$\sin u_a = \frac{\sin i_b \sin \Delta\Omega}{\sin \psi}, \quad (4.15)$$

$$\cos u_a = \cos \Delta\Omega \cos u_b + \sin \Delta\Omega \sin u_b \cos i_b. \quad (4.16)$$

Equation (4.14) is dependent on the orientation of the arrival CR3BP arc, that in turn depends on a properly phased arrival. Consequently, to solve for the proper phasing and orientation, an iterative Newton-Raphson differential corrections scheme is applied:

$$\bar{X} = \begin{bmatrix} \theta_{b_{int}} & \theta_{4_{Mars}} & \theta_{a_{int}} \end{bmatrix}^T, \quad (4.17)$$

$$\bar{F}(\bar{X}) = \bar{r}_a - \bar{r}_b, \quad (4.18)$$

where $\theta_{4_{Mars}}$ corresponds to the true anomaly of Mars when the trajectory intersects the Mars SoI. For an initial guess:

$$\theta_{4_{Mars}} = \arctan(\cos i_{Mars} \tan \Omega_{Mars}) + \omega_a + \theta_a - (\Omega_{Mars} + \omega_{Mars} + \theta_{Mars,J2000}) - \arctan\left(\frac{y_4}{|x_4|}\right), \quad (4.19)$$

where θ_a is the true anomaly of the arrival conic at the SoI intersection, $\theta_{Mars,J2000}$ is the true anomaly of Mars when the Ecliptic J2000 frame is defined, and x_4 and y_4 are the rotating frame coordinates of the trajectory at the SoI intersection. For the targeting problem, the DF Jacobian matrix is determined with the central difference method (see Section 3.1). Consequently, the iterative process ensures that the arrival phasing is accurately targeted, enabling a precise transfer solution between the departure and arrival conics.

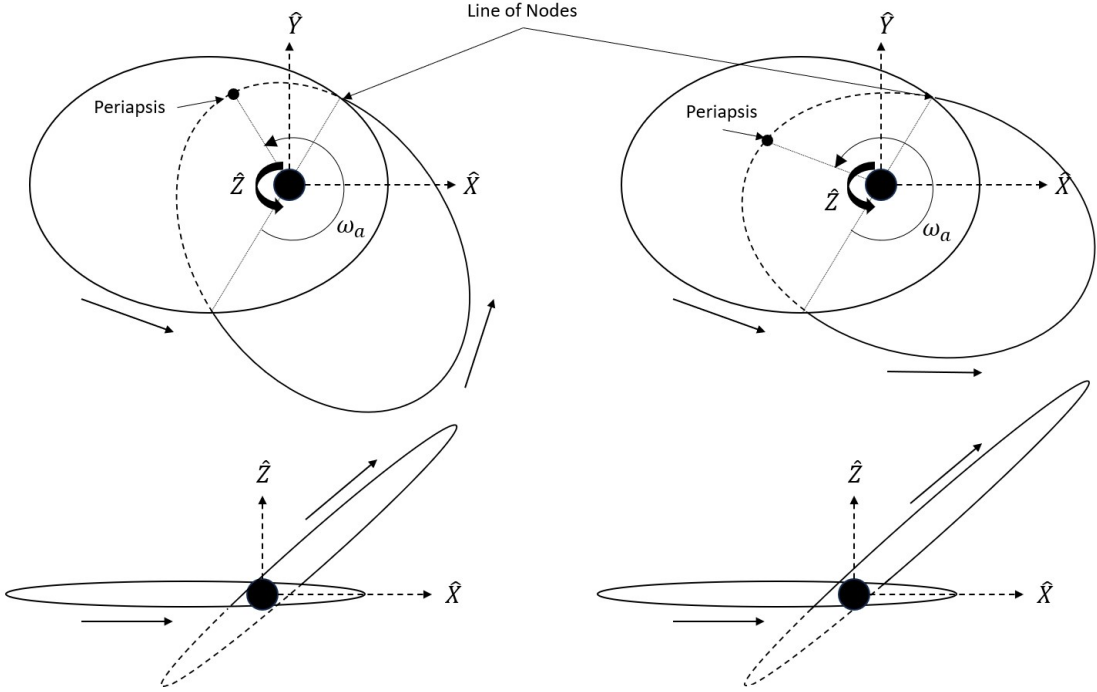


Figure 4.7. Representation of the two feasible arrival ellipse orientations. The top images are XY -plane views while the bottom are XZ -plane views.

Once \bar{X} has been solved, the true anomaly angles are utilized to compute the Cartesian states at each location and the times-of-flight of each segment as was done for the departure conic arc. At the intersection of the bridge and arrival conics, the second maneuver applies an inclination change on top of the energy change so it is not tangential like the first burn. The Δv is still calculated from the difference in the velocity states at the intersection. The second MMAT maneuver, incorporating both the energy and inclination changes, completes the transfer.

The transfer solution between the Sun-Earth CR3BP manifold arc and the Sun-Mars CR3BP manifold arc is now complete. The trajectory is position-continuous throughout, with a maneuver at the beginning and end of the bridge conic arc to account for the velocity discontinuities. For every feasible $\theta_{b_{int}}$, there are two corresponding $\theta_{a_{int}}$ that provide transfer solutions. The two solutions have different maneuver costs and times-of-flight. By continuing in the departure epoch or the selected manifold arc as discussed, a family of MMAT solutions

is obtained and compared, each offering varying maneuver costs and times-of-flight, that can be further analyzed based on mission requirements.

4.2.2 Example

What follows is an example MMAT family between a Sun-Earth CR3BP northern halo orbit at a Jacobi constant of 3.0008189 and a Sun-Mars CR3BP northern halo orbit at a Jacobi constant of 3.0001857. Each transfer in the family starts at a different initial epoch, representing each day in an Earth year. The initial epochs correspond to $\theta_{0_{Earth}}$ values (that span 0° - 360° in a year). All of the trajectories utilize the same departure CR3BP manifold arc, that is the Sun-Earth halo unstable manifold arc with the largest apoapsis, appearing in Figure 4.8. Similarly, all of the trajectories employ the same Sun-Mars halo stable manifold arc with the smallest periapsis as the arrival CR3BP arc, appearing in Figure 4.9. In both figures, the trajectory is propagated to the edge of the sphere of influence. In between, the departure and arrival conic arcs are determined by the osculating Keplerian orbital elements when the manifolds reach their respective spheres of influence and the bridge conic arc joins them as described above, forming a continuous MMAT solution.

In Figure 4.10(a), the times-of-flight and maneuver magnitudes of the family members appear with respect to their initial phasing. Note that there are areas of the initial epochs where transfers could not be computed because the inequality in Equation (4.7) is not satisfied by those orientations. Each successful epoch also has two transfer solutions corresponding to the two arrival phasing solutions described previously. The two groups of transfers in the figure correspond to the two solutions where $n = 0$ or $n = 1$ satisfy Equation (4.7) and are similar due to the symmetry of the possible bridge conic orientations for an intersection. The full time-of-flight for the transfers is generally bounded between 3 and 5.5 years, while the magnitude of the two maneuvers combined is between 4 and 6 km/s. The analysis highlights the impact of initial phasing on transfer feasibility and maneuver costs, revealing a range of solutions that satisfy the MMAT constraints and provide insight into possible interplanetary transfer configurations.

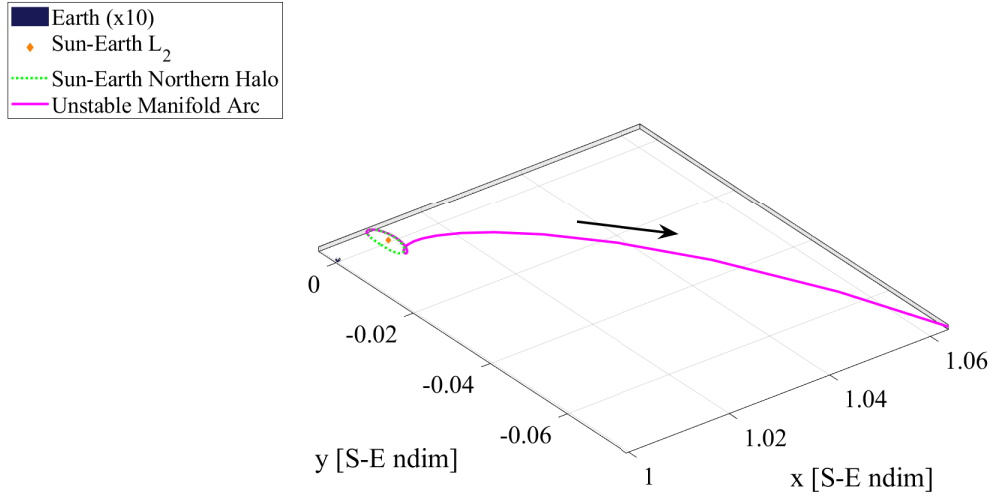


Figure 4.8. MMAT departure CR3BP arc in the Sun-Earth barycentric rotating frame.

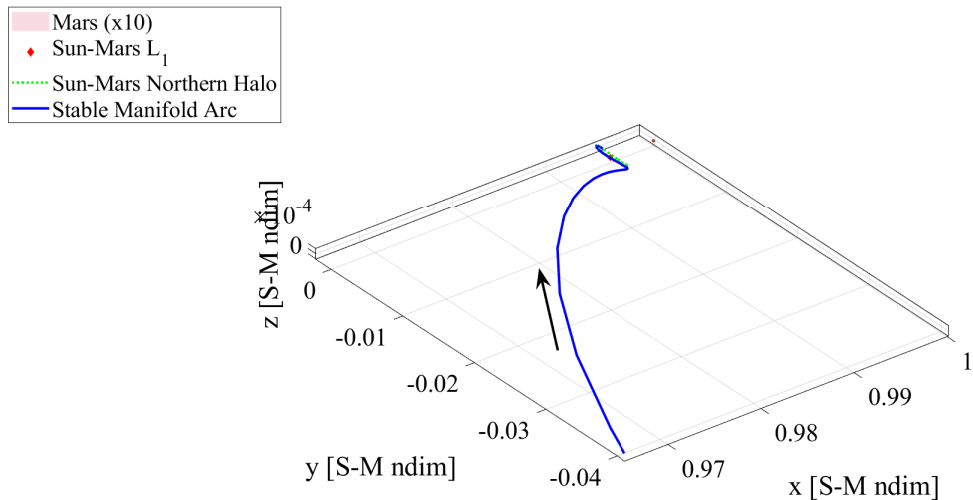


Figure 4.9. MMAT arrival CR3BP arc in the Sun-Mars barycentric rotating frame.

Figure 4.10(b) portrays the same transfers, now with their associated initial Mars phasing $\theta_{0_{Mars}}$. The figure is employed to associate each transfer with an actual launch epoch where the Earth and Mars are in the specified locations in their respective orbits. Varying the selected manifold departure arc while keeping the initial epoch fixed creates families that would appear as vertical lines in Figure 4.10(b), providing additional launch date flexibility, potentially at the cost of maneuver Δv , allowing for a range of transfer solutions, while emphasizing the trade-off between maneuver cost and timing flexibility.

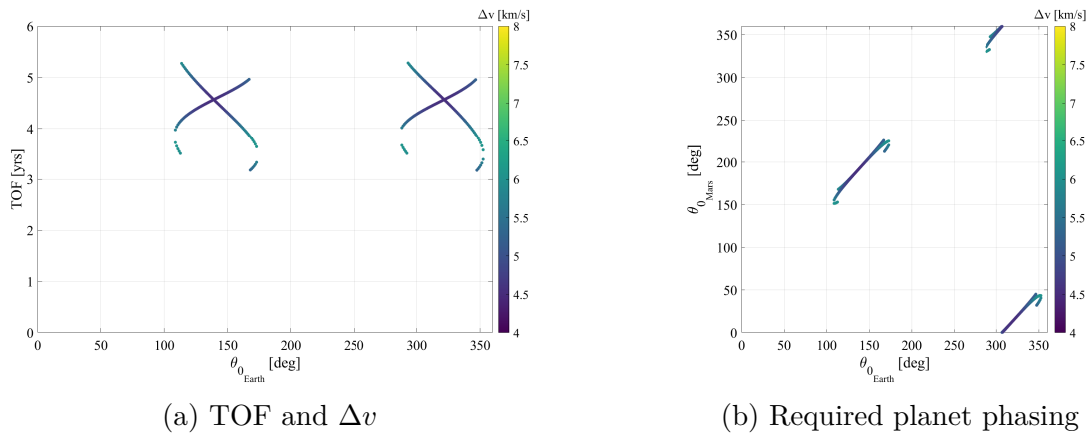


Figure 4.10. Evolution along the MMAT family continued by the initial epoch.

The minimum- Δv transfer from the family appears in Figure 4.11. The total TOF of the transfer is 1670 days or 4.57 years, with a total Δv of 4.537 km/s. In the figure, the various arcs of the MMAT method are color-coded and the maneuvers are marked at the beginning and end of the bridge conic arc. Note that the magenta departure CR3BP arc and the blue arrival CR3BP arc are the same trajectories from Figure 4.8 and Figure 4.9, respectively, just portrayed in the Ecliptic J2000 frame. The minimum- Δv transfer is compared to the minimum-TOF transfer in Figure 4.12. The total TOF has decreased to 1160 days or 3.18 years, but the Δv has increased to 5.298 km/s. Note that the first maneuver has the same magnitude; the increase comes from the second maneuver where the minimum-TOF burn is less tangential to the bridge arc than the minimum- Δv burn to shorten the arrival conic arc time-of-flight. All of the other transfers in the MMAT transfer family have similar geometries and characteristics.

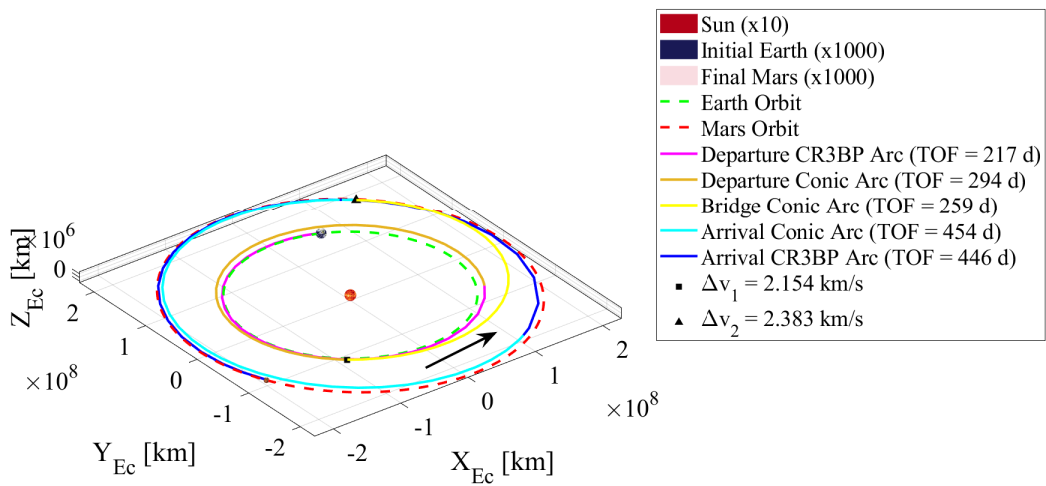


Figure 4.11. Minimum- Δv MMAT in the Sun-centered Ecliptic J2000 frame.

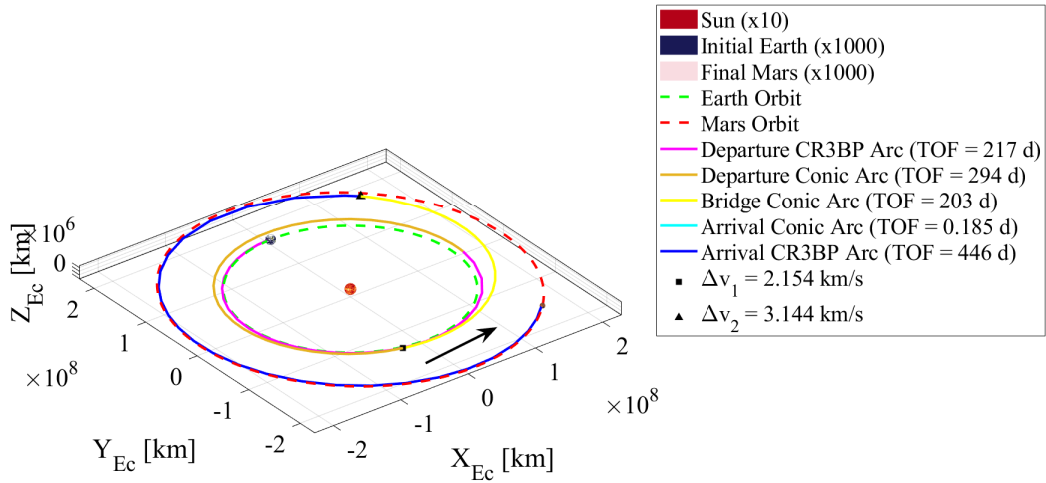


Figure 4.12. Minimum-TOF MMAT in the Sun-centered Ecliptic J2000 frame.

4.3 End-to-End Transfers

All of the transfers analyzed in this investigation arrive into the same Sun-Mars northern halo orbit ($JC = 3.0001857$) via the smallest periapsis stable manifold arc as the MMAT example in Figure 4.9. However, the departure orbit in the Earth-Moon system varies, as well as the unstable manifold arc departing the orbit. The arc selected depends on the category of transfer being employed, and the end-to-end methodology for constructing both categories of transfers is as follows:

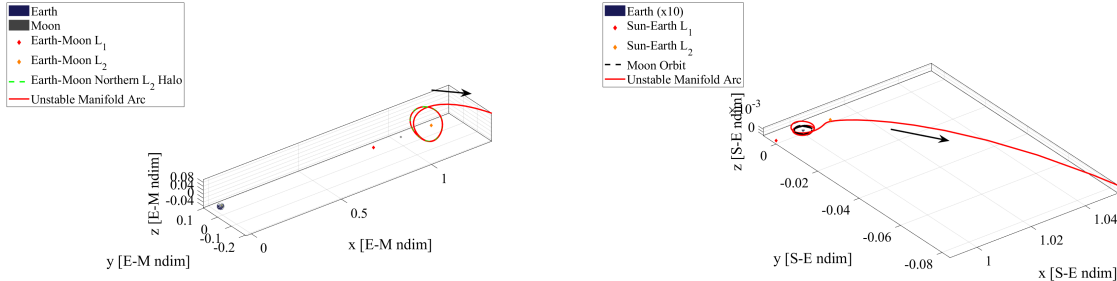
4.3.1 Transfers with Direct System Departure

"Direct" transfers depart from the system directly along an Earth-Moon unstable invariant manifold arc instead of utilizing a staging orbit, not to be confused with direct patched conic transfers between the Earth and Mars.

1. Starting from the Earth-Moon CR3BP departure orbit, both unstable half-manifolds are propagated to the edge of the Earth SoI (ignoring those that crash into the Earth or Moon), where they are transformed into heliocentric Ecliptic J2000 states and propagated under Keplerian dynamics. The step is repeated for several different epochs during January 2026.
2. Each of the feasible manifold arcs then serves as a departure CR3BP arc and departure conic arc for the MMAT methodology introduced in Section 4.2. If they meet the MMAT inequality constraint (Equation (4.7)), then they produce two end-to-end direct transfers between an Earth-Moon and Sun-Mars orbit.

An example direct transfer appears in Figure 4.13 and Figure 4.14. The departure CR3BP arc originates from an Earth-Moon northern L_2 halo with a Jacobi constant of 3.13 in Figure 4.13(a), appearing in the Earth-Moon rotating frame, and continues under the Sun-Earth dynamics until it reaches the Earth SoI in Figure 4.13(b). Note that the trajectory is not optimized, nor is it the minimum-TOF or minimum- Δv solution in the MMAT family originating from that Earth-Moon departure orbit. This particular direct transfer has a total maneuver cost of 5.544 km/s with a total time-of-flight of 3.26 years. The example

direct transfer highlights the potential of the transfer type, demonstrating the viability of employing Earth-Moon unstable manifold arcs for efficient interplanetary transfers.



(a) Earth-Moon barycentric rotating frame.

(b) Sun-Earth barycentric rotating frame.

Figure 4.13. Direct departure CR3BP arc.

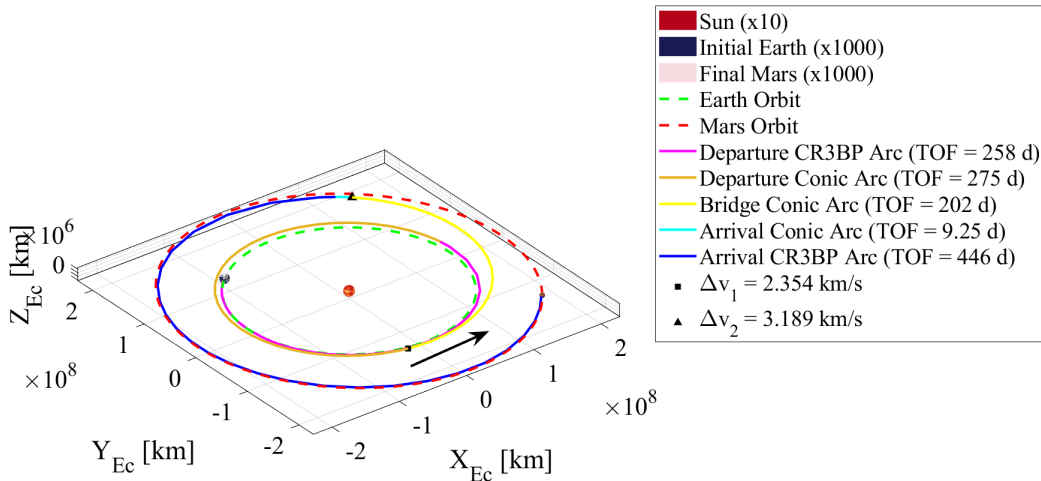


Figure 4.14. "Direct" MMAT in the Sun-centered Ecliptic J2000 frame.

4.3.2 Transfers with an Intermediate Staging Orbit

The staging orbit transfers connect Earth-Moon unstable invariant manifold arcs to Sun-Earth stable manifold arcs before staging in a Sun-Earth L_2 northern halo orbit. After utilizing the orbit to properly phase, the transfers depart from the system along a Sun-Earth unstable invariant manifold arc.

1. Starting from the Earth-Moon CR3BP departure orbit, a near-ballistic transfer to a Sun-Earth CR3BP northern halo orbit is computed via the methodology introduced in Section 4.1. The particular Sun-Earth halo orbit is free to change to decrease the Δv of the maneuver. The Earth-Moon to Sun-Earth portion of the trajectory dictates the initial epoch for the whole transfer.
2. Once in the Sun-Earth staging orbit, since the phase along the orbit is determined by the spacecraft arrival onto the orbit, unstable manifold arcs of the Sun-Earth halo orbit are propagated to the edge of the Earth SoI according to the time-correspondent location along the orbit. Each departure CR3BP manifold arc is then associated with a departure epoch from the Sun-Earth halo orbit.
3. Now, similar to the direct transfers, the arcs serve as the departure CR3BP arc and eventually the departure conic arc for the MMAT methodology (Section 4.2), producing two end-to-end transfers between the Earth-Moon and Sun-Mars orbits with an intermediate staging Sun-Earth halo orbit for each feasible manifold arc.

Figure 4.15-Figure 4.17 provide a sample transfer employing an intermediate Sun-Earth staging halo orbit. The departure from the Earth-Moon orbit in Figure 4.15 is similar to the direct transfer example, utilizing the same L_2 halo orbit. However, a different manifold arc is employed for this transfer. The near-ballistic transfer appears in Figure 4.16, where the Earth-Moon orbit is connected to the Sun-Earth northern halo staging orbit. The departure CR3BP arc is also provided leaving the staging orbit along the unstable manifold, that is then employed in the MMAT in Figure 4.17. Once again, the solution is not optimized, with a total maneuver cost of 5.481 km/s and a time-of-flight of 4.59 years. The example staging

orbit trajectory highlights the potential application of the transfer type, demonstrating the viability of Sun-Earth intermediate orbits to properly phase interplanetary transfers.

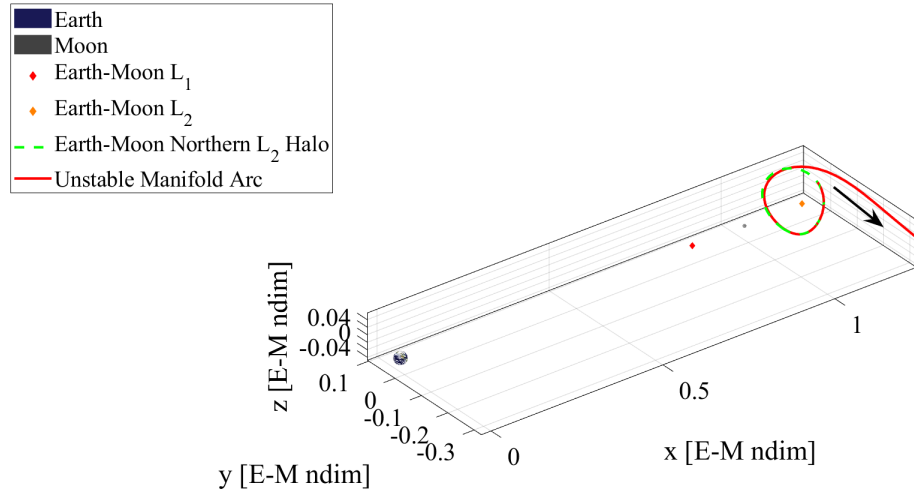


Figure 4.15. Departure unstable manifold arc in the Earth-Moon barycentric rotating frame.

4.3.3 Transfer Tradespace

As mentioned, both categories of transfers exist in families, so the available solutions have a range of total maneuver Δv costs and times-of-flight. Figure 4.18 provides one such tradespace for transfers originating from a $JC = 3.13$ Earth-Moon northern L_2 halo orbit (the same employed in the previous examples). In the figure, the red points represent the family of transfers that include a staging orbit, while the blue points represent the family of direct transfers. The black modified Hohmann transfer line serves as a Δv baseline for comparison. The tradespaces provide valuable insight into the performance of the two transfer strategies, enabling mission designers to balance maneuver costs and time-of-flight against mission requirements and constraints.

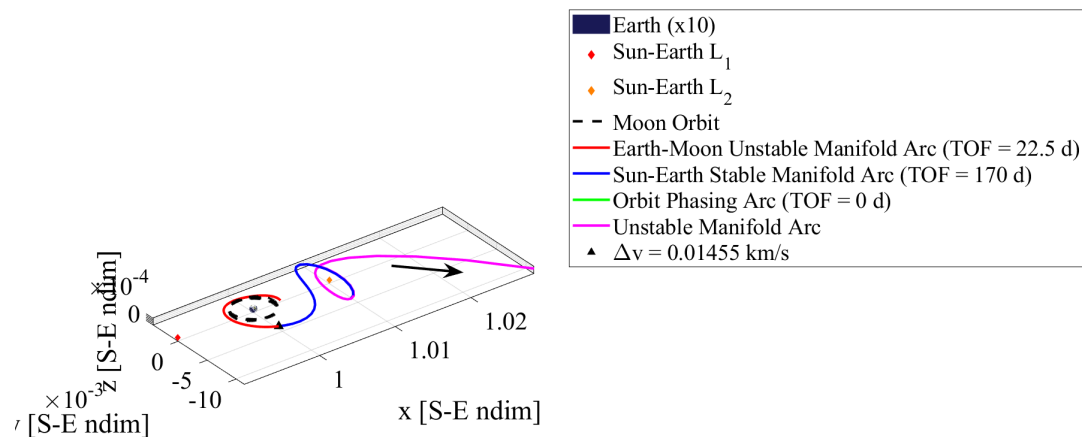


Figure 4.16. Departure CR3BP arc with staging orbit in the Sun-Earth barycentric rotating frame.

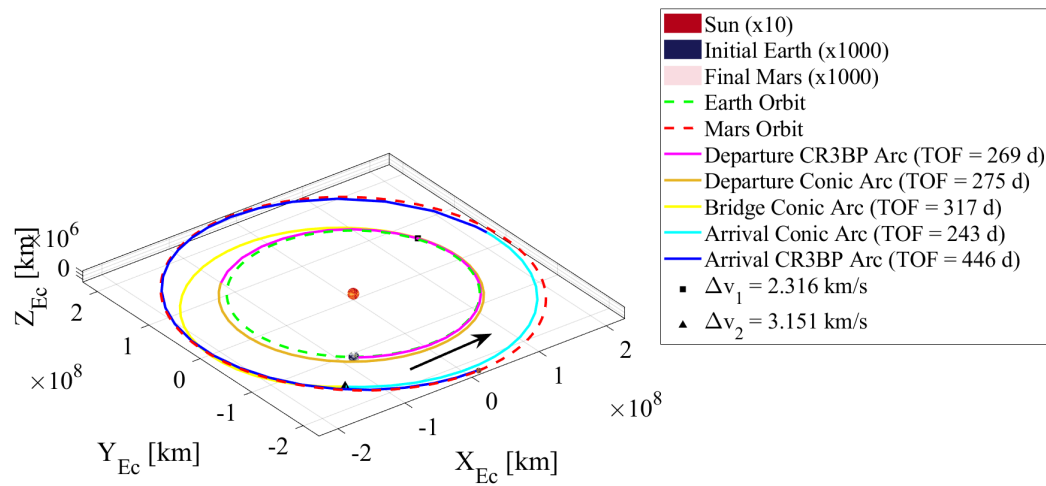


Figure 4.17. MMAT with staging orbit in the Sun-centered Ecliptic J2000 frame.

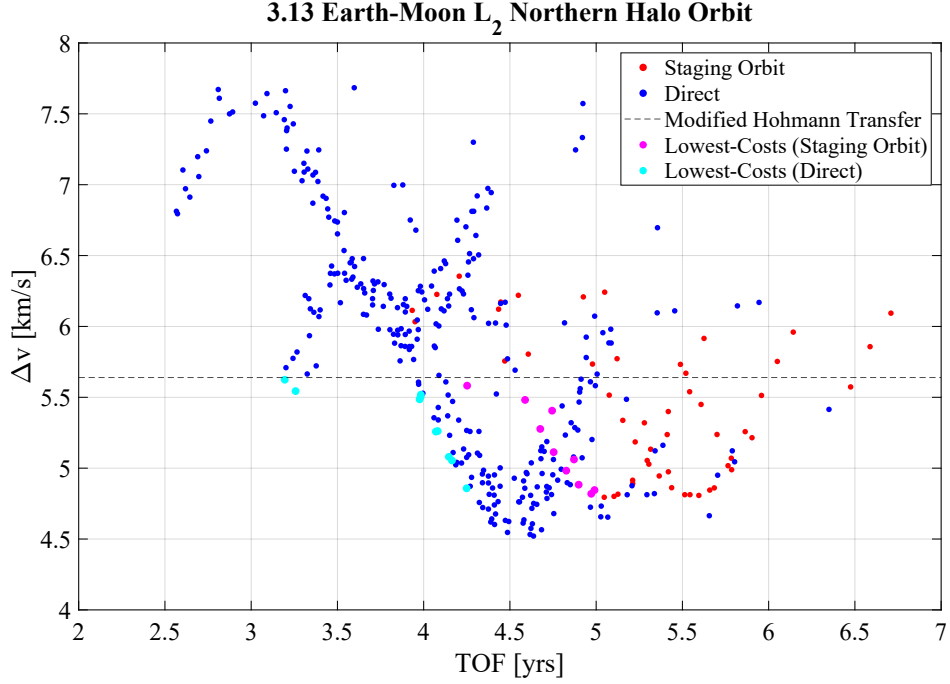


Figure 4.18. Tradespace of both solution categories originating from the same Earth-Moon departure orbit.

4.4 Modified Keplerian Hohmann Transfer

Since the orbits of both Earth and Mars are assumed circular in this investigation, the lowest maneuver cost transfer between the two bodies under Keplerian dynamics is a Hohmann transfer, appearing in Figure 4.19. However, the Hohmann equations only apply when the orbits are coplanar. Hence, a plane change maneuver is introduced to account for the difference in the planetary orbital planes. Inclination change maneuvers have the lowest magnitude at apoapsis, achieved here by including the plane change in the maneuver cost of the second Hohmann burn (Δv_2 in Figure 4.19) to form a modified Hohmann transfer that serves as the baseline Δv cost for Keplerian patched conic transfers between Earth and Mars.

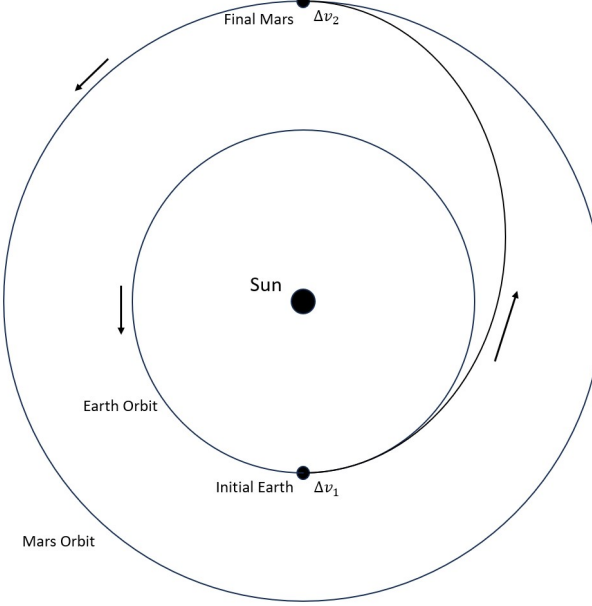


Figure 4.19. Hohmann transfer between Earth and Mars.

To serve as a baseline transfer between cislunar orbits and a Sun-Mars L_1 halo orbit for this investigation, a Hohmann transfer between the Earth orbit (assumed circular at a radius of 1.49598×10^8) and the Sun-Mars L_1 distance (2.26858×10^8) is constructed. The following equations are applied to calculate the modified Hohmann transfer with a plane change:

$$\Delta v_1 = \sqrt{\frac{\mu_{2BP}}{r_1}} \left(\sqrt{\frac{2r_2}{r_1 + r_2}} - 1 \right), \quad (4.20)$$

$$\Delta v_2 = \sqrt{v_H^2 + v_2^2 - 2v_H v_2 \cos \Delta i}, \quad (4.21)$$

$$v_H = \sqrt{\frac{\mu_{2BP}}{r_2} \left(\frac{2r_1}{r_1 + r_2} \right)}, \quad (4.22)$$

$$v_2 = \sqrt{\frac{\mu_{2BP}}{r_2}}, \quad (4.23)$$

where Δv_1 and Δv_2 are the two burns of the transfer, μ_{2BP} is the gravitational parameter of the Sun, r_1 and r_2 are the Earth orbit and Sun-Mars L_1 radii, respectively, v_H is the velocity

at apoapsis of the Hohmann transfer ellipse, v_2 is the circular velocity at Sun-Mars L_1 , and Δi is the difference in inclination between the two orbital planes. The framework results in a total Δv for the modified Hohmann transfer of 5.639 km/s, that is directly compared to the total maneuver costs of the two categories of transfers developed in this investigation to find transfers with lower costs. Note that the minimum Δv required to reach the Sun-Mars L_1 radius from Earth orbit, assuming that a maneuver-less strategy is implemented to decelerate upon arrival, is 2.914 km/s. The comparison highlights the potential for more efficient transfer strategies that reduce the overall maneuver cost compared to a baseline modified Hohmann transfer, while also providing a benchmark for evaluating the effectiveness of alternative approaches.

As stated previously, the modified Hohmann transfer performs the plane change maneuver at the apoapsis of the transfer ellipse, implying that the lowest cost MMAT transfers occur when their second burn is located at the apoapsis of the bridge conic arc. The TOF of the Hohmann transfer arc is calculated analytically:

$$TOF = \pi \sqrt{\frac{(r_1 + r_2)^2}{7\mu_{2BP}}}, \quad (4.24)$$

which is analogous to the times-of-flight of the MMAT bridge conic arcs. The minimum- Δv transfer has a TOF of 258 days. The time-of-flight serves as a reference point for evaluating the temporal efficiency of MMAT bridge arcs relative to the modified Hohmann transfer.

5. CISLUNAR DEPARTURE ORBIT COMPARISON

The two approaches introduced in the previous chapter for designing end-to-end transfers from the cislunar region to Mars are used to generate families of transfers from various departure periodic orbits in Earth-Moon CR3BP unstable families. For given departure orbits, the transfers that stage in an intermediate Sun-Earth halo orbit are compared to the transfers with "direct" departures from the Sun-Earth system to determine the usefulness of a staging orbit. A cost function is introduced to aid in the selection of desirable transfers in each transfer group. Then these selected transfers are compared across the various cislunar departure orbits to analyze trends in the departure characteristics across orbit families and energy levels. Finally, the maneuver Δv and TOF costs of the transfer strategies developed in this investigation are compared to existing literature and methodologies to show that this approach reduces the maneuver costs for a Mars mission.

5.1 Comparing Transfers via Intermediate Sun-Earth Halos to Direct Transfers

Just like the example tradespace provided in Section 4.3.3 with Figure 4.18, for a given cislunar departure orbit, the "direct" transfers are compared to the staging orbit ones. The tradespaces for all of the cislunar departure orbits used in this investigation are provided in Appendix A, along with figures showing the departure orbits themselves, but some are introduced in this section to facilitate the comparison.

In general, for the scenarios examined in this investigation, transfers with lower times-of-flight tend to have higher maneuver costs and vice versa. This is not a strict rule, but as shown in the example of Figure 4.18, the transfer points lie mostly in the upper-left and bottom-right sections of the tradespace.

In all of the tradespaces computed in this investigation, the blue points representing the "direct" transfers mostly lie to the left of the red staging orbit transfers but well above the modified Hohmann transfer baseline. These correspond to direct transfers with lower TOF but much higher Δv compared to the staging orbit transfers. However, there are often some transfers in the tradespace where the Δv lies below the baseline of the modified Hohmann transfer and even below those of the staging orbit transfers.

5.1.1 A Simple Cost Function

In the example of Figure 4.18, the transfer family that directly departs the system contains the minimum-TOF and minimum- Δv solutions. In this specific case, the minimum- Δv solution of the direct transfers has a lower TOF than most of the staging orbit transfers. However, this is not always the case, as shown in Figure 5.1. Here, while the direct transfers still have a lower TOF, the staging orbit transfer family reaches a lower Δv . As a result, often a transfer choice needs to be made balancing TOF and maneuver Δv cost. A cost function can help select desirable transfers that balance these two parameters.

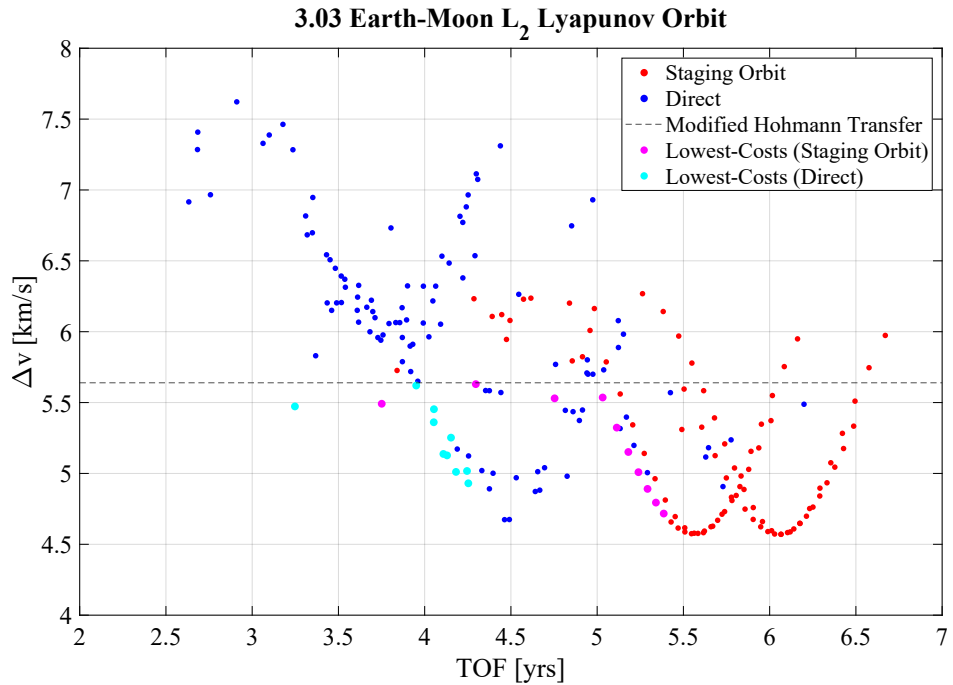


Figure 5.1. Transfer tradespace departing from an Earth-Moon L_2 Lyapunov orbit ($JC = 3.03$).

If total TOF and total maneuver Δv are considered to have units of years and km/s, respectively, then these values have similar orders of magnitude for these transfers. Therefore, an appropriate cost function places weights on the two parameters according to the desired transfer characteristics for a given mission:

$$J = \alpha TOF + \beta \Delta v, \quad (5.1)$$

where J is the cost function value and α and β are design variables to adjust the cost function. α and β can be adjusted to place higher priority on TOF or Δv , depending on the particular application. This investigation uses $\alpha = 5$ and $\beta = 2$ as a representative cost function to prioritize lowering the TOF while still looking for decreased maneuver costs. This cost function is applied to transfers in the tradespace that are below the modified Hohmann transfer Δv baseline, and the ten transfers that have the lowest J -value from each transfer category are determined to be the lowest-cost transfers for this application. In Figure 5.1, these are cyan points for the "direct" transfers and magenta ones for the "staging orbit" transfers.

5.1.2 Comparing Lowest-Cost Solutions between Transfer Types

In Figure 5.1, among the lowest-cost solutions selected using the cost function, the direct options have a lower average TOF than the staging orbit ones, 4.04 and 4.94 years, respectively, while the transfers with staging orbits achieve a slightly lower average Δv cost, 5.207 km/s compared to 5.238. The earlier example from Figure 4.18, now shown including the lowest-cost solutions from the cost function in Figure 5.2, produces similar results. In contrast, the "direct" options in Figure 5.3 have both lower times-of-flight and maneuver costs when compared to the staging orbit transfers, 4.33 years and 4.869 km/s average for direct transfers versus 4.82 years and 5.148 km/s for those with a staging orbit. In all of the tradespaces computed in this investigation, the lowest-cost direct solutions perform better than the lowest-cost staging orbit transfers with regards to TOF. While the lowest-cost staging orbit solutions often have slightly lower Δv costs on average, the significantly longer times-of-flight outweigh those benefits, and there are still many cases where the direct options require lower maneuver costs.

One downside to the direct departure method is that it relies on the spread and rapid departure of the Earth-Moon unstable manifolds. A major contributing factor is the cis-lunar orbit's proximity to the Moon or Earth. If manifold arcs crash into one of the primaries or get captured by their gravitational effects, it can delay the arcs' departure from the system and also impact their distribution in position space, leading to fewer available transfers. The

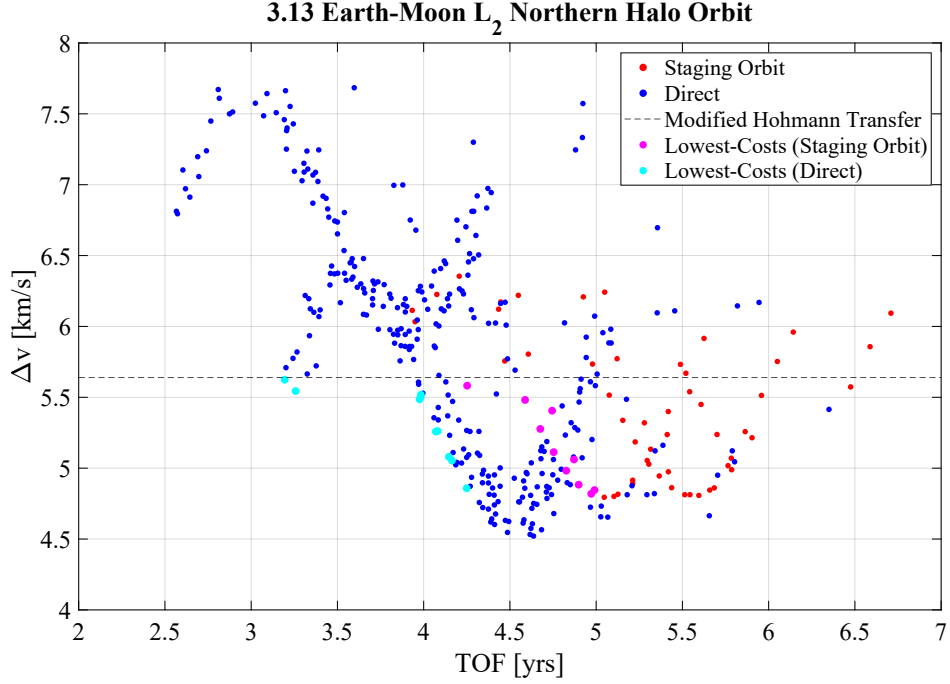


Figure 5.2. Transfer tradespace departing from an Earth-Moon L_2 northern halo orbit ($JC = 3.13$).

stability of the orbit also plays a role in affecting the departure time since more unstable orbits have manifolds that depart the orbit vicinity faster. When there are fewer departure arcs available, it leads to fewer successful end-to-end transfers with direct departures, as shown in Figure 5.4. Note that there is a significantly decreased number of available "direct" solutions and that the ones that do exist no longer follow a familial pattern similar to the previous examples. Since the staging orbit transfers only require one manifold arc to interface with the Sun-Earth orbit stable manifold, there is still a full range of staging orbit transfers available for this case. However, the lowest-cost direct solutions still outperform the staging orbit ones in this specific scenario.

The results of this investigation and the provided observations demonstrate that the methodology developed to construct end-to-end cislunar-to-Mars transfers that directly depart the Sun-Earth system performs better overall than the strategy that incorporates an intermediate Sun-Earth halo staging orbit. The lowest-cost solutions that directly depart the cislunar orbits used in this investigation always have a faster average TOF than the lowest-cost staging orbit transfers. While the direct options only sometimes have a lower

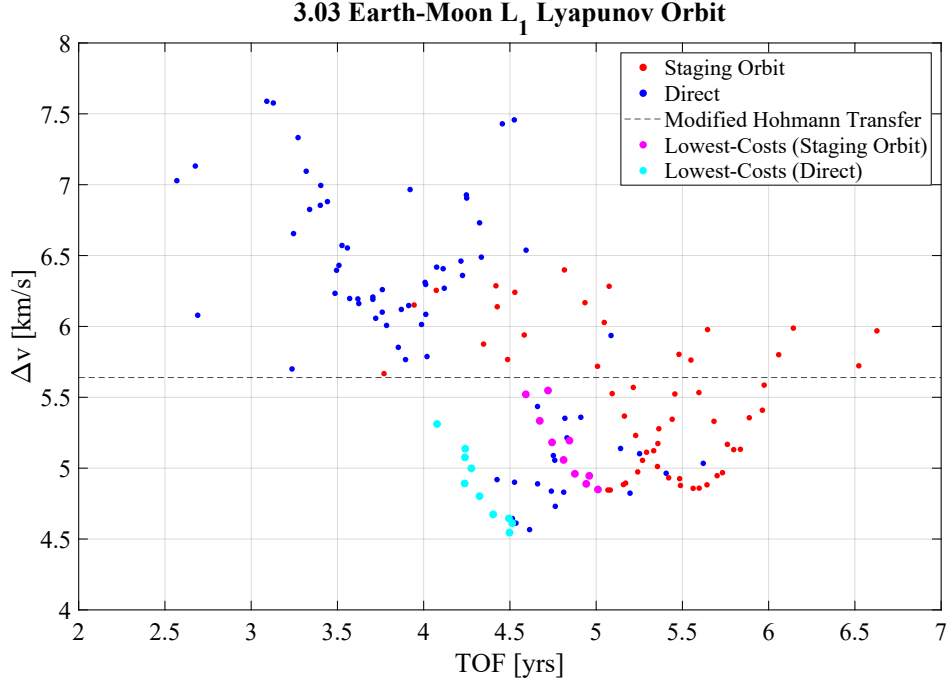


Figure 5.3. Transfer tradespace departing from an Earth-Moon L_1 Lyapunov orbit ($JC = 3.03$).

Δv maneuver cost than the staging orbit ones, the decrease in TOF is significant enough to outweigh the potential slight increases in maneuver cost.

5.2 Comparing Cislunar Departure Families

In this investigation, unstable periodic orbits in the Earth-Moon CR3BP are considered as potential departure orbits for deep-space transfers. Several orbit families with unstable members are introduced in Section 3.2 and from these families, unstable orbits between Jacobi constants of 2.98 and 3.13 are analyzed to determine their feasibility for these transfers. This range was chosen since the upper energy bound of 2.98 is slightly above the energy level of the L_4 and L_5 Lagrange points, while the lower bound includes a large number of the unstable libration orbits[41]. Note that not all of the included families have unstable orbits at these energy levels. Additionally, in some instances, even though the orbits existed, their stability, energy, or location prevented their unstable invariant manifolds from interfacing with the stable manifolds of the staging orbit or departing the system promptly. Several

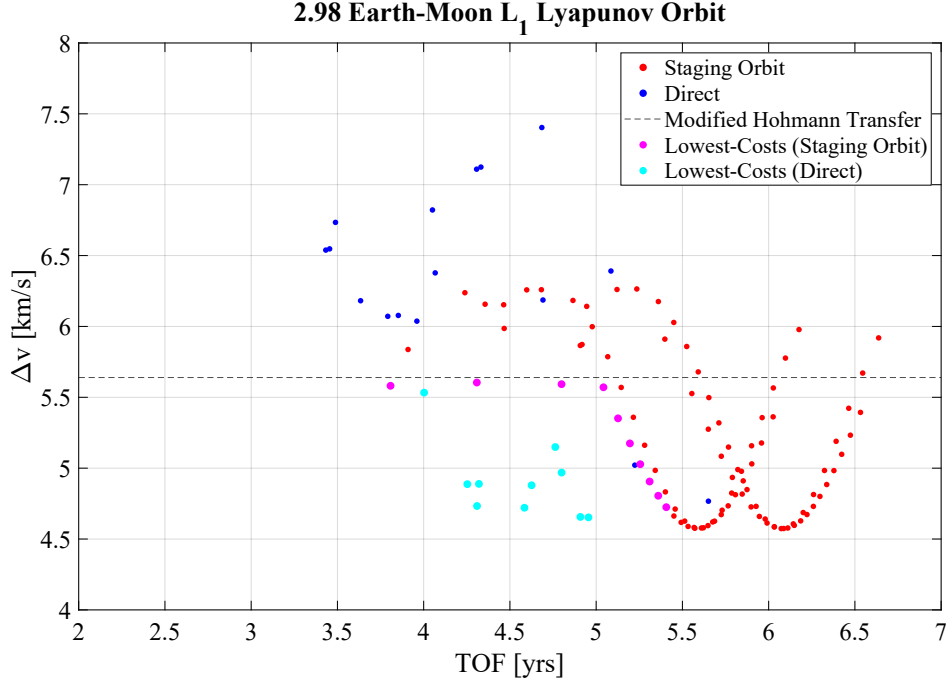


Figure 5.4. Transfer tradespace departing from an Earth-Moon L_1 Lyapunov orbit ($JC = 2.98$).

other periodic orbit families were also investigated, including L_4 and L_5 long-period orbits and some unstable resonant orbit families. However, invariant manifolds from orbits in these families also took too long to depart the system for this investigation.

For the feasible departure orbits, the cost function described previously is used to determine the most desirable end-to-end transfers in the orbit's tradespace, and then the average total maneuver Δv and TOF costs are compared between the various departure orbits in this investigation. While no one orbit or family of orbits provides the lowest-cost transfers across the different energy levels, some trends can be extracted from the results to inform cislunar departure orbit selection for these types of missions.

5.2.1 Contributing Factors for Lower Total Maneuver Costs

Of the two maneuvers, or three if using a staging orbit, in the end-to-end transfer, the largest is the final burn that includes the inclination change between the Sun-Earth and Sun-Mars planes. Plane change maneuvers are most efficient at a conic orbit's apoapsis, so

this maneuver Δv is lower when the MMAT bridge conic true anomaly at the intersection of the conic sections, $\theta_{b_{int}}$, is near 180° . This also requires that the departure and bridge conics are oriented such that their apoapses are near the line of nodes since the inclination change must occur at either the ascending or descending node. The conic intersection location is a function of the relative orientations of the departure and arrival conics, which are dependent on the phasing of the departure from and arrival at the two planetary systems.

As mentioned, the cost function identifies the transfers with the lowest cost, considering both the maneuver cost and TOF. Therefore, among the ten lowest-cost transfers in a tradespace, there will be ones with lower total Δv and ones with a lower TOF. Figure 5.5-Figure 5.7 show an example staging orbit low- Δv case departing from a northern L_1 halo orbit, with a total maneuver cost of 4.781 km/s and TOF of 5.21 years. Likewise, Figure 5.8 and Figure 5.9 show a direct example departing from an L_1 Lyapunov orbit, with a total maneuver cost of 4.55 km/s and TOF of 4.49 years. In both MMAT figures, Figure 5.7 and Figure 5.9, the two maneuvers occur approximately 180° apart from each other, and since the first burn is constrained to be at the periapsis of the bridge conic, the second burn is near apoapsis. Note that in the transfer example with direct departure, the manifold arc chosen departs on the L_2 side of the Sun-Earth system. This is consistent for lower- Δv direct transfers across all the departure orbits analyzed in this investigation.

Beyond the relative orientation between the two MMAT maneuvers, the energy gap between the departure and arrival arcs (and thereby the Sun-Earth and Sun-Mars CR3BP arcs, respectively) also contributes to the total Δv . A larger difference requires a higher-cost maneuver to change the Keplerian conic energy from the departure arc to that of the arrival arc; these energies are determined by the manifold arcs chosen and the phasing of the two planetary systems. This highlights the importance of families of transfer solutions. Since several interdependent factors affect the total maneuver cost, it is necessary to search through the results across families of solutions to find low- Δv solution basins.

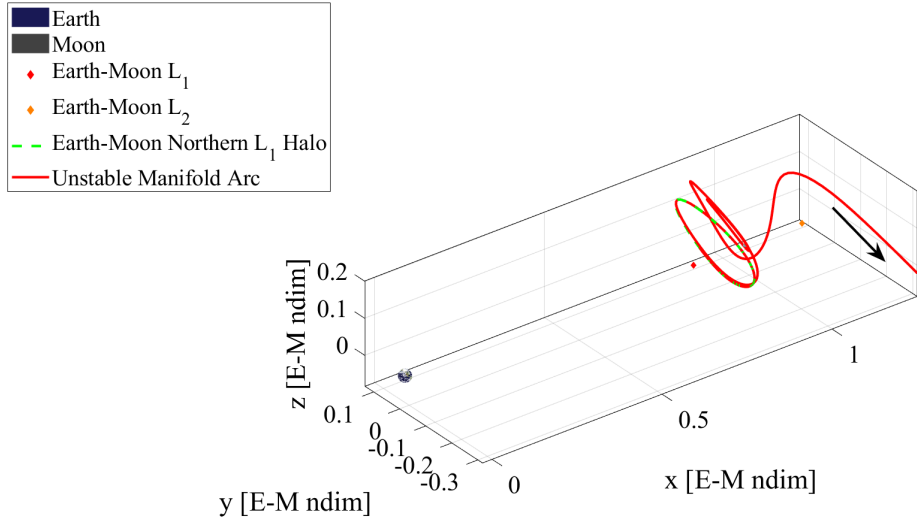


Figure 5.5. Northern L_1 halo orbit ($JC = 3.03$) departure manifold arc in the Earth-Moon barycentric rotating frame for a low- Δv case.

5.2.2 Contributing Factors for Lower Total Times-of-Flight

While Δv is primarily dependent on the final MMAT maneuver location, the biggest factor affecting time-of-flight is the relative orientation of the departure and arrival conic arcs. Since these are dependent on their respective CR3BP manifold arcs, the phasing of the two planetary systems at departure and arrival largely dictate the total transfer TOF. As mentioned, the first MMAT maneuver occurs at the periapsis of the departure conic arc. Therefore, to minimize the time along the departure conic arc, its periapsis should be just after the Sun-Earth CR3BP SoI intersection. Similarly, although the true anomaly of the intersection between the bridge and arrival arcs can vary, it should be just before the Sun-Mars CR3BP SoI intersection true anomaly to minimize the time along the arrival conic arc.

As it turns out, the time along the arrival conic arc is easier to decrease than that of the departure conic arc. Figure 5.10–Figure 5.12 show a low-TOF case from the lowest-cost staging orbit transfers of a northern L_2 halo orbit, with a total maneuver cost of 5.582 km/s

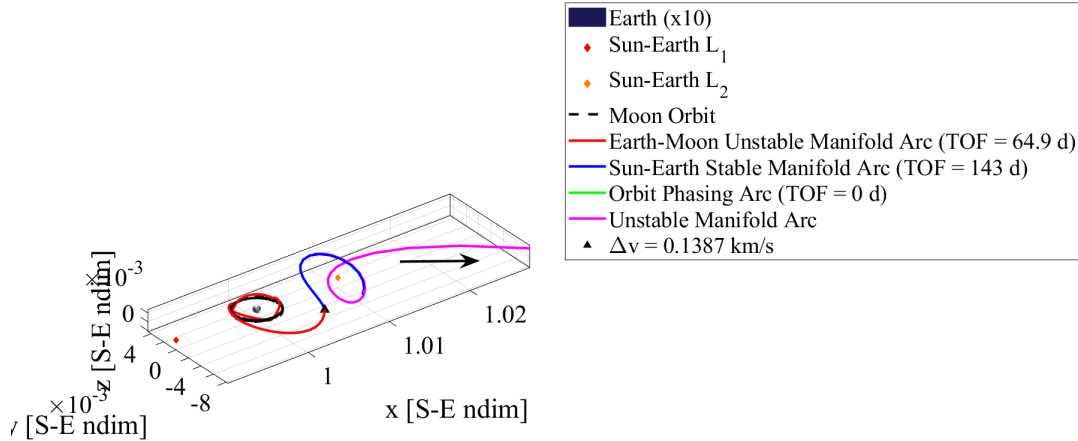


Figure 5.6. Departure CR3BP arc with northern L_2 halo staging orbit ($JC = 3.000808$) in the Sun-Earth barycentric rotating frame for a low- Δv case.

and TOF of 4.25 years. Departing from the same $JC = 3.13$ northern L_1 halo orbit, the transfer shown in Figure 5.13 and Figure 5.14 has a total maneuver cost of 5.624 km/s and TOF of 3.19 years. In Figure 5.12 and Figure 5.14, the TOF of the arrival conic arc is minimal compared to the other legs of the transfer, while the departure conic arc TOF remains about as large as the other solutions. In the Sun-Earth rotating frame representation of the direct departure transfer, Figure 5.13(b), the manifold arc again departs on the L_2 side of the Sun-Earth system. This is because the lowest-cost solutions chosen with the cost function tend to be closer to the minimum- Δv cases instead of the minimum-TOF transfers. So the lowest-TOF transfer among the lowest-cost solutions is still closer to a minimum- Δv case. For the truly minimum-TOF transfers, with maneuver costs much higher than the modified Hohmann transfer baseline, the unstable manifold arcs depart on the Sun-Earth L_1 side.

A few other ways to reduce the total transfer TOF involve the other three legs of the transfer. Although the minimum- Δv transfers occur when the bridge and arrival conic arc

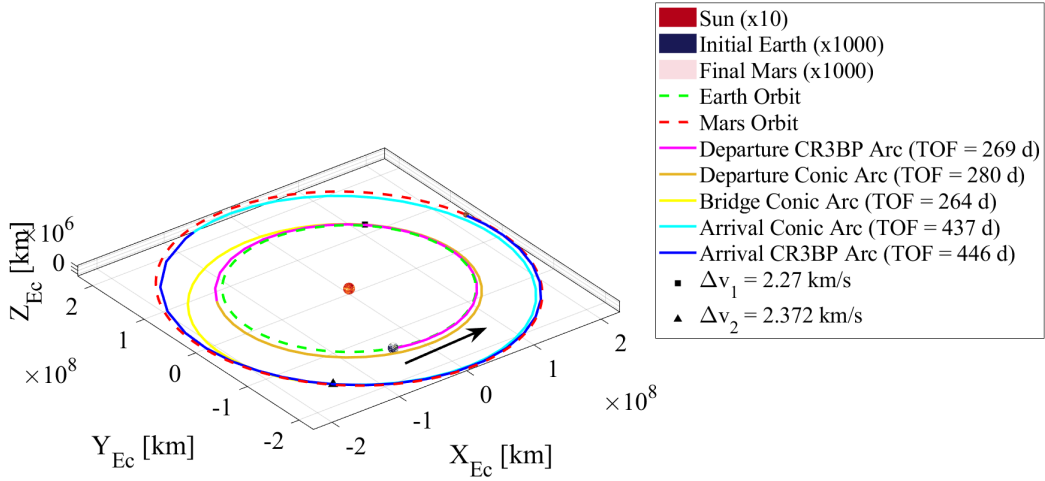
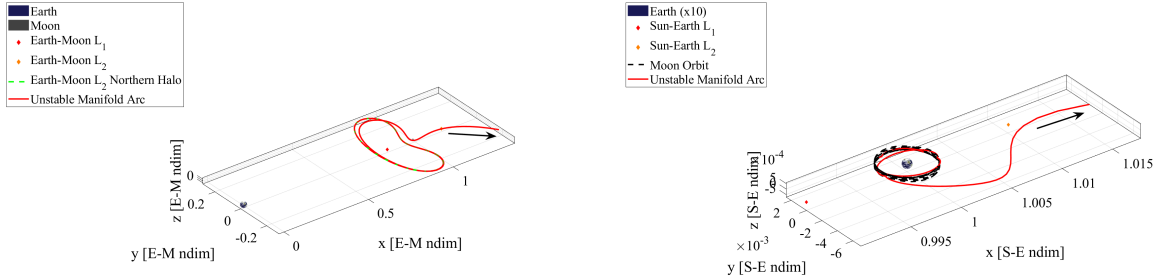


Figure 5.7. MMAT in the Sun-centered Ecliptic J2000 frame for a staging orbit low- Δv case.



(a) Earth-Moon barycentric rotating frame.

(b) Sun-Earth barycentric rotating frame.

Figure 5.8. L_1 Lyapunov orbit ($JC = 3.0$) departure CR3BP arc for a low- Δv case.

intersection is 180° from the first MMAT maneuver, the bridge arc TOF can be decreased by moving the final maneuver closer to the periapsis. While this will increase the maneuver cost, it can sometimes be worth the flight time savings. Another option is to decrease the departure and arrival CR3BP arc times-of-flight via the invariant manifold arc selections.

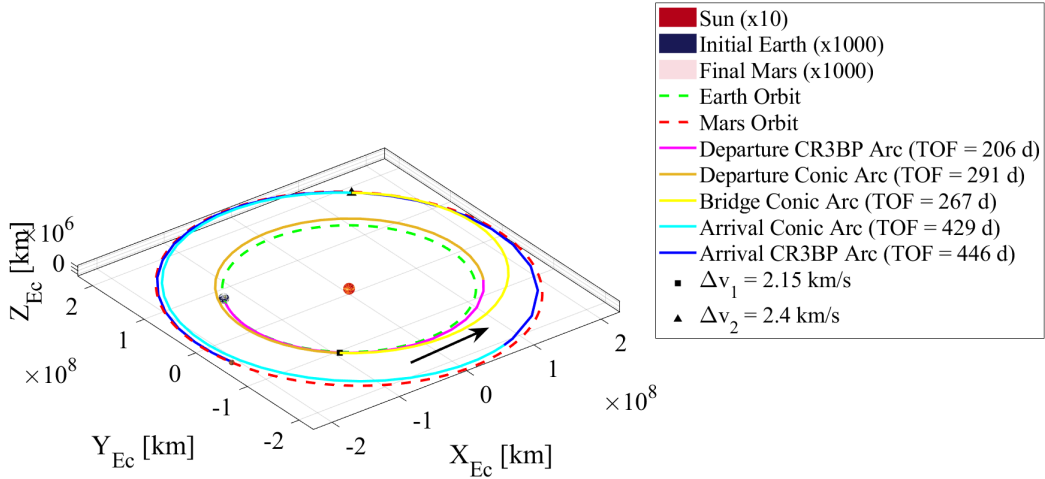


Figure 5.9. MMAT in the Sun-centered Ecliptic J2000 frame for a direct low- Δv case.

Since some manifold arcs depart faster from the system than others from the same orbit, this can lead to slight decreases in TOF.

5.2.3 Comparison between Departure Orbits

Since both categories of transfers have similar average Maneuver Δv costs among their lowest-cost solutions, it is easiest to evaluate the two types separately for that metric. Figure 5.15 compares the average Δv values for the lowest-cost departures using staging orbits from the orbits used in this investigation. As mentioned previously, no one orbit family performs the best across the range of Jacobi constant values; however, some general trends can be identified. Overall, these transfers perform better than the baseline modified Hohmann transfer in terms of maneuver cost by around 0.5 km/s while at each energy value, the spread between the families is on the order of 0.2 km/s. Some families show significant cost fluctuation across energy levels while others do not. The families that seem to perform the best overall are the L_1 halo and L_1 vertical families, although they are not necessarily the best

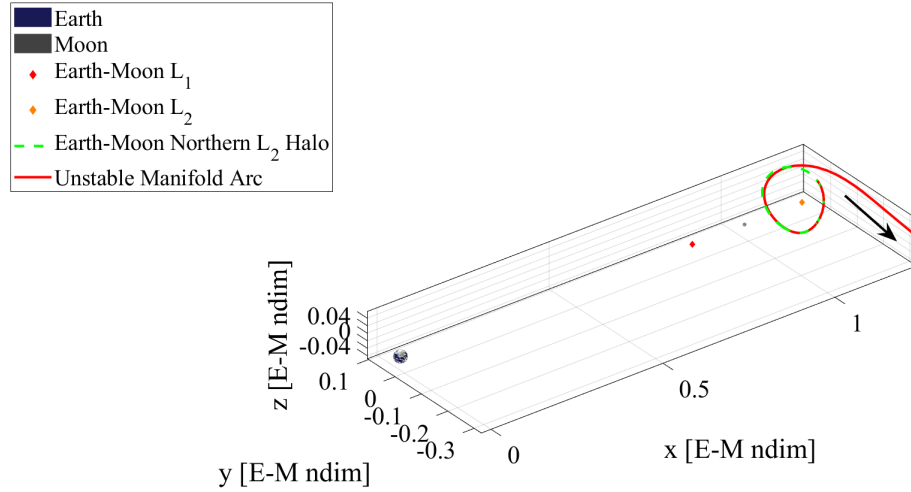


Figure 5.10. Northern L_2 halo orbit ($JC = 3.13$) departure manifold arc in the Earth-Moon barycentric rotating frame for a low-TOF case.

choice at each Jacobi constant. The L_2 axial family also performs well, but unfortunately, unstable members only exist at lower Jacobi constant values. While it may not be the optimal choice in every mission scenario, the lowest maneuver cost staging orbit transfers in this investigation originate from the 3.03 L_1 northern halo orbit, with an average total Δv of 4.978 km/s. Figure 5.5-Figure 5.7 show one such transfer from this specific departure orbit. On the other hand, the L_1 and L_2 Lyapunov families, as well as the butterfly family, all have higher maneuver costs compared to the others.

Similarly, Figure 5.16 shows the average Δv values for the lowest-cost direct departures. These orbits display similar performance on average to the staging orbit transfers in comparison to the baseline modified Hohmann transfer. However, the lowest Δv cases reach nearly 0.8 km/s improvement. The spread between the families is larger, reaching 0.5 km/s for some Jacobi values, but the variation across families is just as inconsistent as with the staging orbit transfers. For these direct transfers, the L_1 Lyapunov orbit family performs the best by far at every Jacobi constant value except 3.1 (where it is one of the worst options).

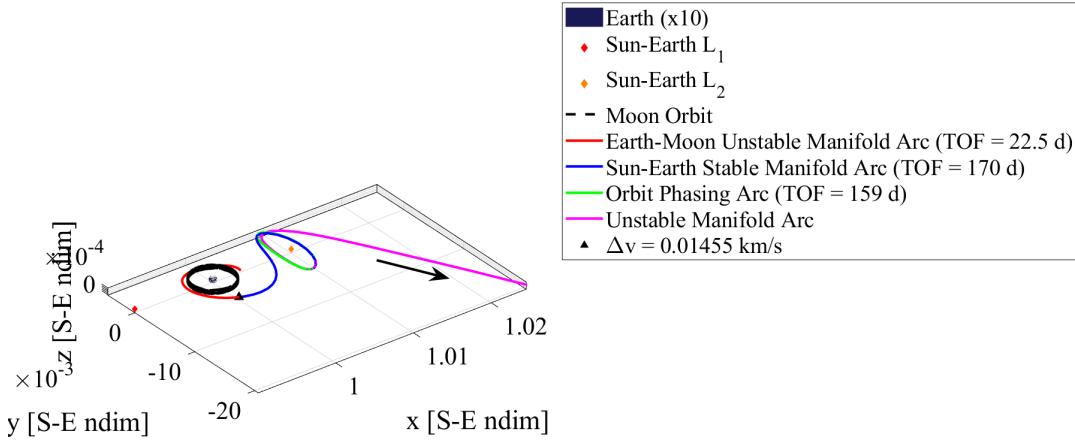


Figure 5.11. Departure CR3BP arc with northern L_2 halo staging orbit ($JC = 3.0008189$) in the Sun-Earth barycentric rotating frame for a low-TOF case.

The L_1 halo family also performs well overall. The 3.0 L_1 Lyapunov orbit provides the lowest maneuver cost direct transfer with an average total Δv of 4.791 km/s. An example transfer from this orbit is shown in Figure 5.8 and Figure 5.9. The L_2 halo and vertical families have the highest maneuver costs of the families.

For both categories of transfers, L_1 orbit families seem to produce lower- Δv transfers. It is likely that many of these transfers with invariant manifolds originating from Earth-Moon L_1 departure families leverage close passes by the Moon to lessen the eventual energy gap between the planetary systems, resulting in decreased maneuver costs. Again comparing the two transfer types, in general, the lowest-cost transfers with direct departures outperform the lowest-cost transfers with staging orbits in terms of maneuver costs. Nevertheless, both types see cost reduction compared to the baseline modified Hohmann transfer.

When comparing the total transfer TOF between the two categories, the differences are large enough to be evaluated directly in a single figure. Figure 5.17 shows the average lowest-cost TOF values for both staging orbit transfers and those with direct departures. The

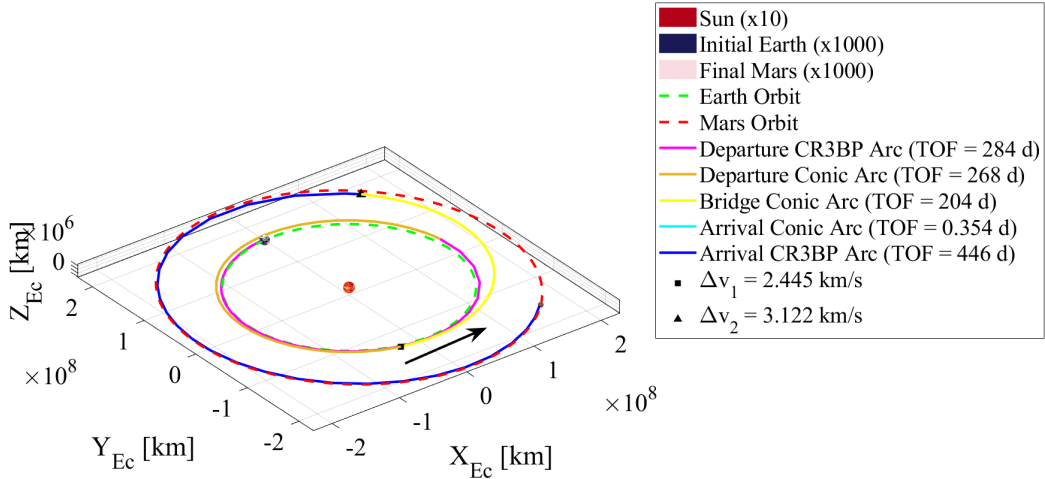
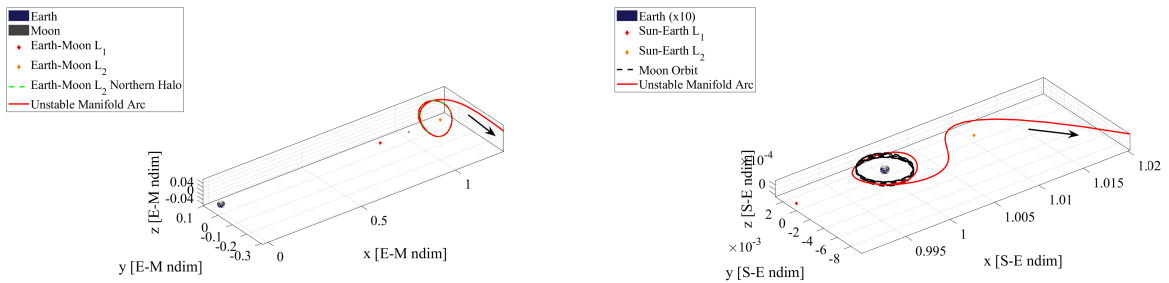


Figure 5.12. MMAT in the Sun-centered Ecliptic J2000 frame for a staging orbit low-TOF case.



(a) Earth-Moon barycentric rotating frame. (b) Sun-Earth barycentric rotating frame.

Figure 5.13. Northern L_2 halo orbit ($JC = 3.13$) departure CR3BP arc for a low-TOF case.

staging orbit transfers all lie in the range of 4.7-5.5 years, while the direct transfer times-of-flight are significantly lower in comparison: 3.9-4.6 years. It is interesting to note that the energy levels with higher times-of-flight for the staging orbit transfers are not the same as the higher TOF options for direct transfers. The spread in TOF between the families at each

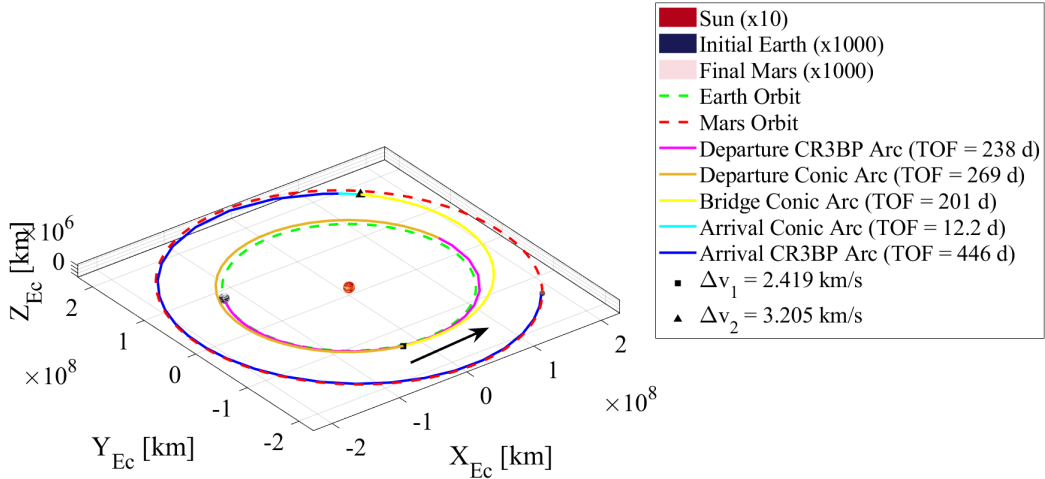


Figure 5.14. MMAT in the Sun-centered Ecliptic J2000 frame for a direct low-TOF case.

Jacobi constant value fluctuates both within each transfer type and overall. For instance, the 3.1 direct transfers have a spread of about 0.15 years while it is 0.6 at a Jacobi constant of 2.98, and the spread is near 0.3 years for staged orbits at a Jacobi constant of 3.03 but 0.6 years for 3.07.

Like with the total Δv costs, the lowest-cost total TOF values fluctuate unpredictably across each family of orbits. Regardless, for the transfers with staging orbits, the L_2 Lyapunov and L_2 halo orbits perform the best overall in TOF, although the results are a little less clear than when comparing Δv costs. The lowest TOF option investigated is the 3.13 L_2 northern halo orbit, with an average total TOF of 4.76 years, shown in Figure 5.10–Figure 5.12. With this transfer type, the families that perform the worst are the L_1 vertical and L_2 axial families. For the direct transfers, the L_2 halo and L_2 vertical orbits have the lowest times-of-flight. The L_2 axial orbits also perform well at their limited energy values as with the Δv . In this category, the 3.13 L_2 northern halo orbit again performs the best with an average total TOF of 3.91 years, shown in Figure 5.8 and Figure 5.9. The ones that have the longest times-of-flight are the L_1 Lyapunov and halo families. While L_1 departure

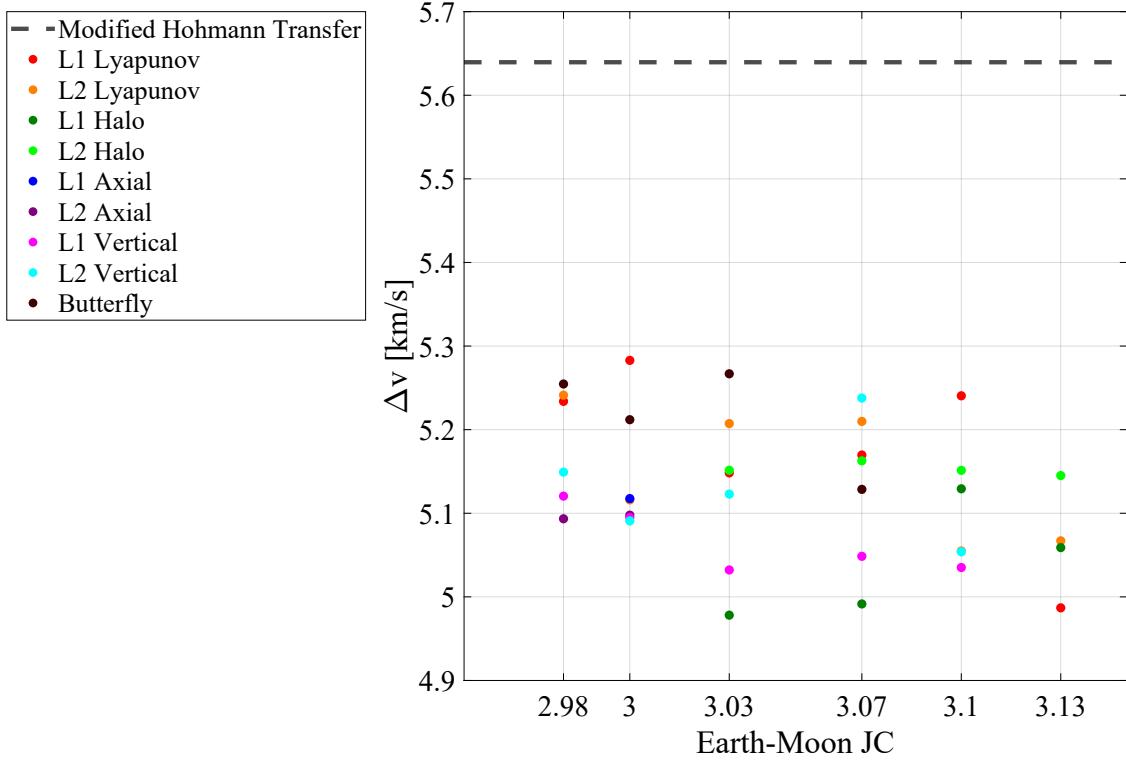


Figure 5.15. Average Δv comparison between lowest-cost transfers with staging orbits/families.

orbits seem to provide lower maneuver costs, Figure 5.17 shows that L_2 departure orbits tend to have lower lowest-cost times-of-flight. This may be because the manifold arcs reach the Earth SoI faster and extend slightly farther, decreasing the TOF of the transfer.

Many of the previous examples have shown that the transfers with lower total Δv tend to have higher times-of-flight and vice versa. Therefore, to find the departure orbits that provide decreases in both, the lowest-cost solutions are compared using J , the cost function value. The results of this comparison are shown in Figure 5.18. Immediately, it is clear once again that the transfers with direct departures outperform those with staging orbits, with J values near 31 and 36 respectively. Note that these J values have little physical significance but are a linear combination of the Δv and TOF. The J value spread at each Jacobi constant value is similar to the spread in TOF in Figure 5.17.

In general, comparing the J values between the departure orbits, it is less clear which families perform the best. For the staging orbits, the L_2 halo orbits have lower costs at the

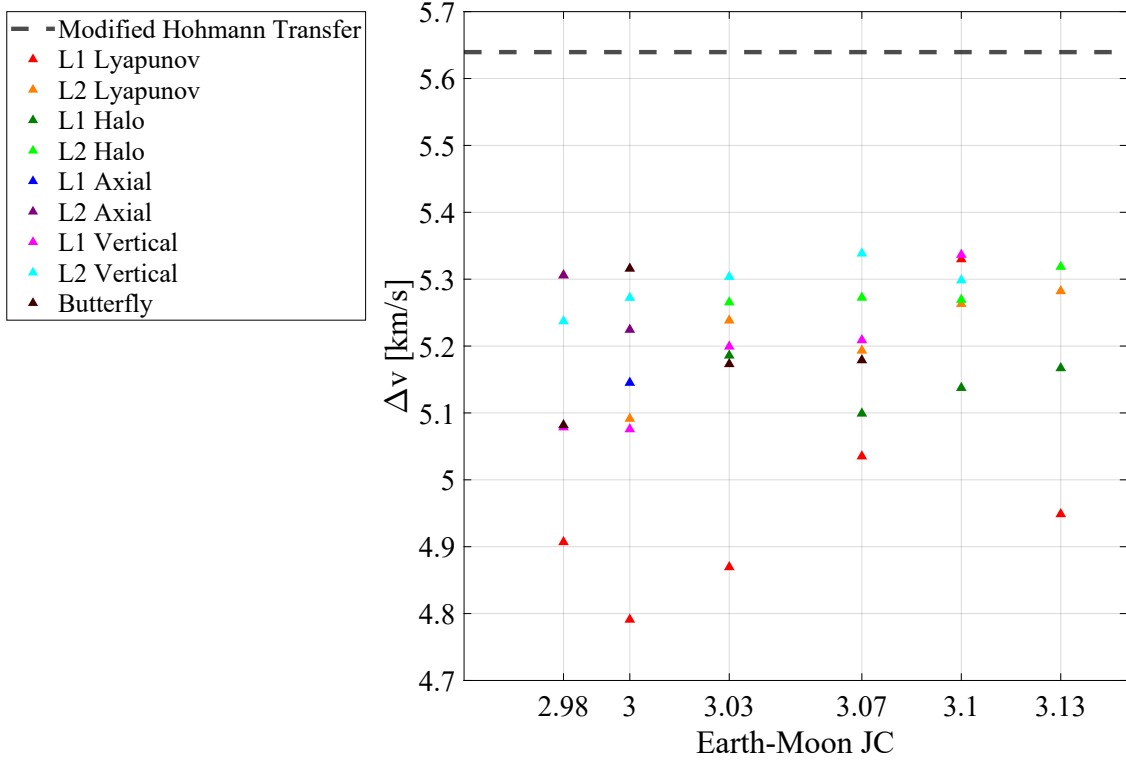


Figure 5.16. Average Δv comparison between lowest-cost transfers with direct departures from various orbits/families.

higher Jacobi constant values. At the lower Jacobi constants, the better families are different for each case, although the L_2 Lyapunov orbits are consistently low throughout. Comparing the direct transfers, the L_2 vertical orbit family performs well across the majority of the energy range, with the L_2 halos again having low values at higher Jacobi constant orbits. Still within the direct transfer category, the L_1 Lyapunov family performs the worst when evaluated with the cost function. The lowest overall cost departure orbit is surprisingly the 3.13 L_2 Lyapunov orbit direct departure, with an average cost function value of 30.19, an average total maneuver cost of 5.282 km/s, and an average total TOF of 3.92 years. The lowest-cost direct transfer from this departure orbit is shown in Figure 5.19 and Figure 5.20 with a total maneuver cost of 5.293 km/s and TOF of 3.24 years.

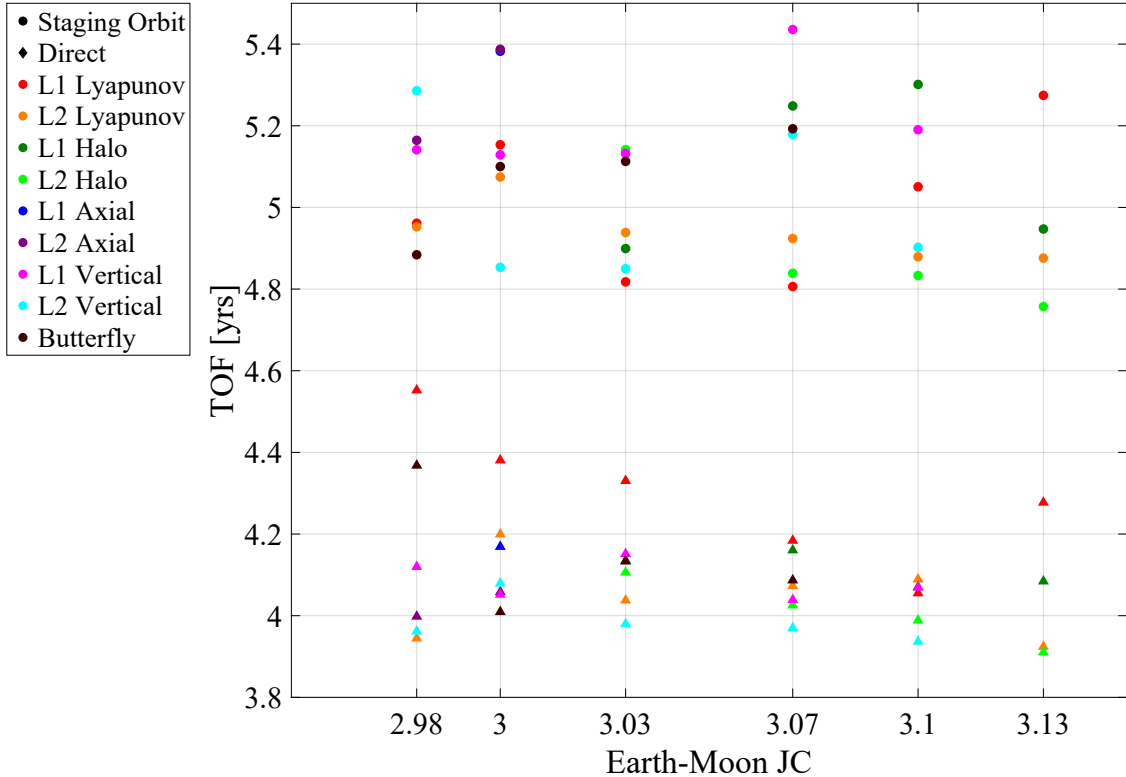


Figure 5.17. Average TOF comparison between lowest-cost transfers from various orbits/families.

5.3 Comparison to Previous Work

As mentioned previously in Section 1.3, several authors have investigated transfers between Earth or cislunar space and Mars. These studies use a variety of methodologies to accomplish these transfers, leveraging direct impulsive burns, low-thrust, and/or invariant manifolds. Some of their relevant findings are provided here for comparison to the results of this investigation.

It is important to note that each of the transfers from these investigations, whose results are consolidated into Table 5.1, uses a different methodology. Some use an optimizer, others leverage invariant manifolds, and the number and placement of maneuvers vary from transfer to transfer. Additionally, each one departs from and arrives at different locations, making it difficult to directly compare the total maneuver Δv and TOF values. Many of the investigations also assume that the orbital planes of Earth and Mars are coplanar, neglecting the

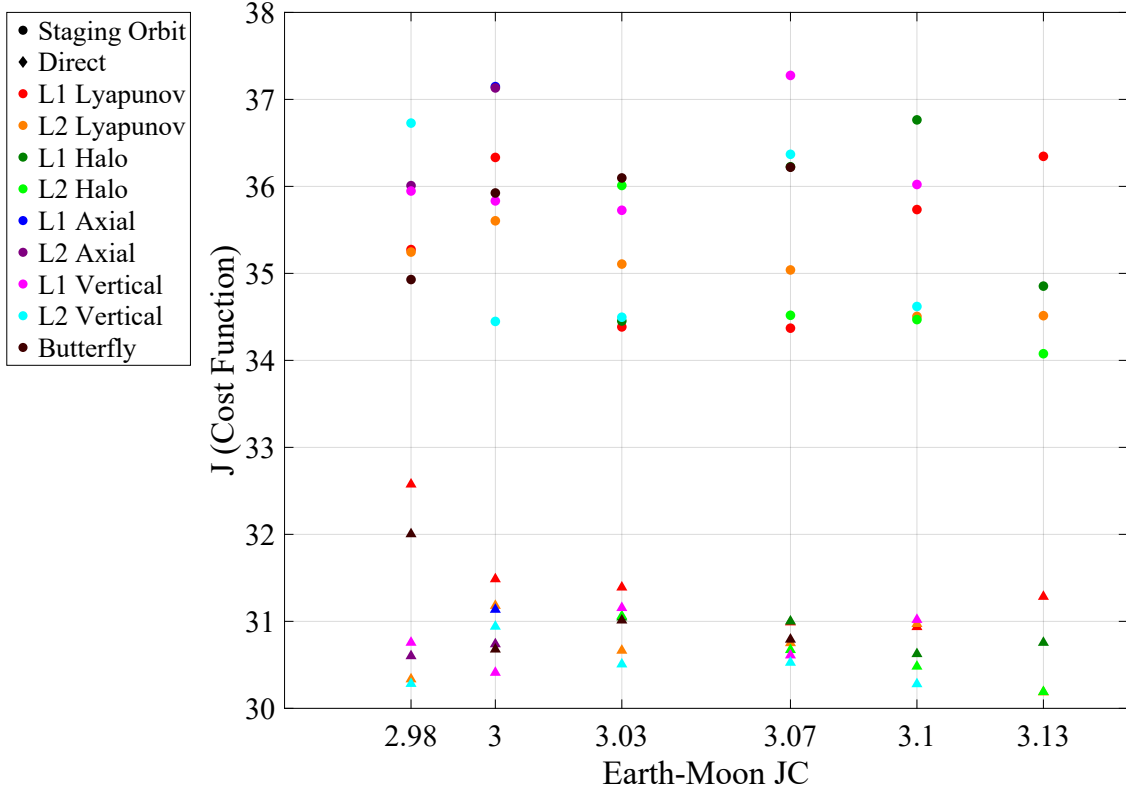
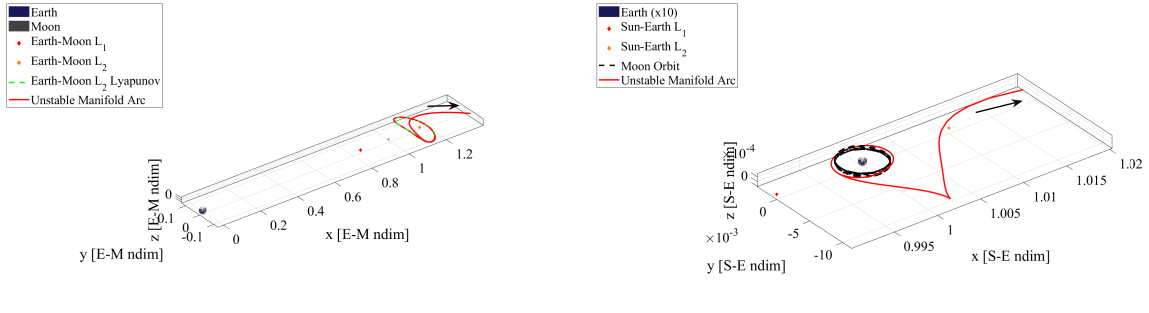


Figure 5.18. Average cost function value comparison between lowest-cost transfers from various orbits/families.



(a) Earth-Moon barycentric rotating frame. (b) Sun-Earth barycentric rotating frame.

Figure 5.19. L_2 Lyapunov orbit ($JC = 3.13$) departure CR3BP arc for lowest-cost case.

nontrivial plane change maneuver required when considering true orbital planes. Therefore, a direct comparison cannot be made between all of these methodologies. However, they do provide some intuition for the costs of similar interplanetary transfers.

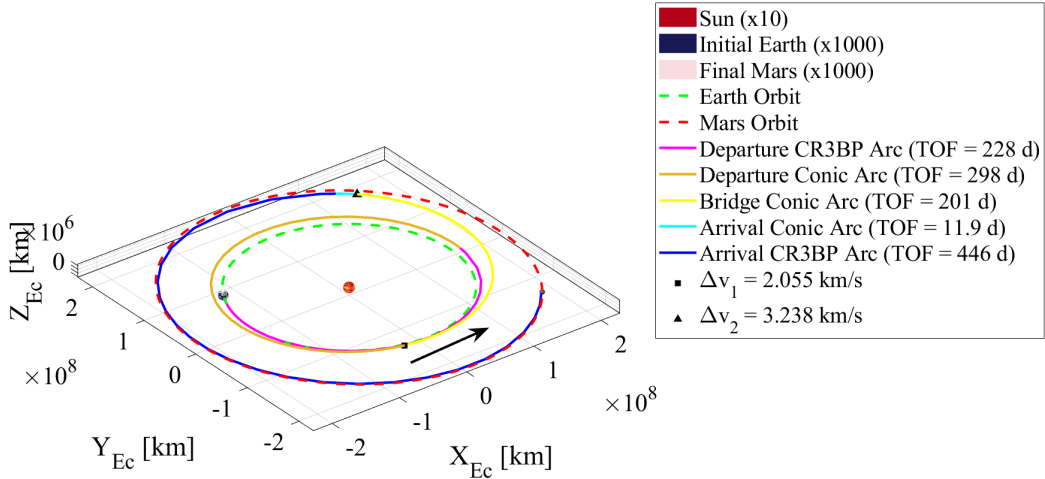


Figure 5.20. MMAT in the Sun-centered Ecliptic J2000 frame for lowest-cost case.

Kakoi et al. inspired the transfer methodology between the Earth-Moon and Sun-Earth CR3BP models[25], [38]. Their investigation focused on comparing different transfer scenarios departing from Earth-Moon L_1 and L_2 halo orbits. While the strategies used are slightly different, Kakoi et al. construct transfers that utilize Sun-Earth unstable invariant manifolds and compare them to direct transfers from Earth-Moon halo orbits. As some sample values for an L_2 halo departure, their investigation found that a transfer along a Sun-Earth halo invariant manifold required a total maneuver cost of 1.604 km/s and a total TOF of 1762 days (4.82 years). Note that in their investigation, a maneuver is applied along the departure manifold arc to speed up the transfer and the final destination is Mars' location, cutting off the long arrival time of the stable manifold arc. On the other hand, directly using the unstable manifold from the Earth-Moon halo orbit resulted in a transfer with a Δv of 0.921 km/s and a TOF of 1784 days (4.88 years)[38]. This direct transfer again uses a maneuver along the departure manifold arc, as well as an inclination change maneuver during an Earth-flyby. Other direct transfers provided in the study have lower and higher times-of-flight and maneuver costs, showing that there is a wide variety of available options.

Table 5.1. Representative transfer costs from previous and current investigations.

Transfer Type	Origin	Destination	Δv [km/s]	TOF [days]
Hohmann Transfer	Earth	Sun-Mars L_1	5.64	258
Lambert Arc[53]	Earth	Mars	5.61	310
Optimized 4-Body[19]	LEO	LMO	5.65	258
Lambert Arc CR3BP[20]	Lunar DRO	LMO	3.29	206
CR3BP Manifolds[22]	S-E Lyapunov	S-M Lyapunov	3.76	999
Pseudo-Manifolds[24]	S-E Halo	S-M Halo	2.06	596
CR3BP Manifolds[25]	E-M Halo	Mars	0.92	1784
CR3BP Manifolds[26]	Lunar DRO	S-M Lyapunov	5.40	1102
CR3BP MMAT[29]	S-E Halo	S-M Halo	4.53	1776
CR3BP MMAT	E-M Halo	S-M Halo	5.10	1520

The results of the current investigation are consistent with Kakoi's conclusions. Utilizing invariant manifolds can decrease transfer maneuver Δv values while increasing the TOF[38]. This is shown here via comparison to the results of previous investigations and direct comparison to the patched conic modified Hohmann solution. While Kakoi's transfer data cannot be directly compared to those from this investigation, the general conclusion of Kakoi et al. is that the utilization of direct Earth-Moon manifolds allows for more flexible departure dates and transfer options, while the comparison of transfers with direct departures to those with Sun-Earth staging orbits is orbit-dependent[25], [38]. This investigation supports the flexibility of the direct transfer methodology and concludes that the maneuver cost comparison is orbit-dependent. However, with the MMAT strategy used to connect the planetary system invariant manifolds, it is shown that the options with direct departures have shorter times-of-flight compared to when an intermediate staging orbit is included.

From a direct comparison between the Δv and TOF results of this investigation and the previous studies summarized in Table 5.1, incorporating invariant manifolds can decrease maneuver cost on the order of 1 km/s compared to modified Hohmann transfers, Lambert arcs[53], and optimized direct solutions from LEO to LMO[19]. As explained, the manifold arcs do significantly increase the transfer TOF, but this is an acceptable trade-off for some mission scenarios and depends on the transfer design. The results are also consistent with some previous manifold transfers between CR3BP orbits[26], [29].

At first glance, several of the entries in Table 5.1 that utilize manifolds appear to have better results than those produced by this investigation. However, the transfers cannot be directly compared because of discrepancies between the assumptions and dynamical models utilized as well as different origins/destinations. All of these investigations besides the one from Kakoi et al. assume that the Sun-Earth and Sun-Mars systems are coplanar and depart from the Sun-Earth system instead of cislunar space[22], [24]. This results in a lower Δv and TOF for those transfers by ignoring the first leg of the journey and the inclination change maneuver. Kakoi's transfers target Mars' position instead of terminating in a nearby orbit, eliminating the need for arrival maneuvers and manifold arcs that end Δv and time[25]. Even with those simplifying assumptions, the results from these investigations that include invariant manifolds have long times-of-flight, suggesting that these results do not contradict the findings from this investigation.

Overall, this investigation provides transfers that have lower maneuver Δv costs than direct patched conic methods but with longer times-of-flight. The results are consistent with invariant manifold transfers from previous literature; the maneuver costs are higher due to the use of a more accurate dynamical model and cislunar departure orbits. While the TOF is longer in some cases, using transfers that directly depart the system instead of intermediate staging in Sun-Earth halo orbits can decrease those times on the order of 1 year. Additionally, the proposed transfer methodologies connect Earth-Moon CR3BP orbits to Sun-Mars CR3BP orbits using invariant manifolds, a likely future mission scenario that has not received a lot of attention to date.

6. CONCLUDING REMARKS

For humanity to develop and maintain a constant presence at Mars and other deep-space locations, a comprehensive understanding of multi-body dynamical systems theory and departure dynamics within cislunar space is critical. This investigation develops a methodology for designing transfers from unstable cislunar periodic orbits to deep-space targets utilizing invariant manifolds in the CR3BP. By applying dynamical systems theory, this design approach links multiple CR3BP systems for end-to-end transfers that exist in families of solutions, allowing for more flexible mission designs. Additionally, in this investigation, various unstable cislunar periodic orbit families are analyzed in the context of these interplanetary transfers to evaluate their departure characteristics. The result is an improved understanding of invariant manifold departure behavior in the Earth-Moon CR3BP, as well as a catalog of Mars transfer tradespaces. The end-to-end transfer maneuver costs in this investigation are consistent with other lower-energy transfers in previous literature and better than traditional approaches, although the time-of-flight increases significantly. This section summarizes the contributions of this investigation and provides several recommendations for future work.

6.1 Investigation Summary

6.1.1 Low-Energy Cislunar-to-Mars Transfer Design Methodology

Unstable periodic orbits in the CR3BP possess unstable and stable invariant manifolds that asymptotically depart from or arrive onto the orbit and arcs from these manifolds are utilized to construct ballistic transfers starting or terminating at these orbits. However, in the context of interplanetary and deep-space transfers, the energy gaps between invariant manifolds of different systems prevent direct connections between these manifolds, dictating the need for bridging arcs or alternative strategies. The end-to-end cisunar-to-Mars transfer design methodology developed in this investigation patches two planetary manifold arcs together with a heliocentric Keplerian bridging arc employing the MMAT approach. Since this bridging leg of the trajectory is sufficiently far away from both the Earth and Mars, the solar gravity is the dominating force considered and is adequately modeled by the relative

2BP, leading to a semi-analytical method for computing this part of the transfer. This approach is also able to incorporate the true orbital planes of Earth and Mars, resulting in a higher model fidelity and robust framework for a transfer design to bridge planetary systems.

In addition to the MMAT methodology, some end-to-end transfers constructed in this investigation stage in an intermediate L_2 halo orbit in the Sun-Earth CR3BP. Those solutions rely on near-ballistic connections between unstable Earth-Moon and stable Sun-Earth invariant manifold arcs for low-cost transfers in a blended CR3BP model. Solutions that instead directly depart the system without connecting to a staging orbit still rely on this blended model, transitioning from one CR3BP system to the other at the edge of the Moon sphere of influence. The successful meshing of the blended CR3BP and patched 2BP-CR3BP dynamical models facilitates the end-to-end transfers between Earth-Moon and Sun-Mars CR3BP periodic orbits.

Another major benefit of this new transfer methodology is that the transfers exist in families of solutions. Through the exploitation of dynamical systems theory, there are a variety of ways to continue the family of solutions. Each solution tradespace for the orbits employed in this investigation, all of which are supplied in Appendix A, shows families of transfer solutions continued by varying either the unstable departure manifold or the initial departure epoch. New families could also be generated by varying the stable arrival manifold onto the Sun-Mars halo orbit or the Jacobi constant of the intermediate staging orbit. By not relying on individual point solutions that have to be recomputed whenever a parameter changes, the transfer methodology developed in this investigation offers improved mission design flexibility while also providing a broader view of the design tradespace.

6.1.2 Intermediate Sun-Earth Staging Halo Orbits

Since unstable invariant manifolds asymptotically depart from periodic orbits, the cis-lunar manifold arcs take a long time to depart from the Earth-Moon system. Once they do, these manifold arcs are propagated under the Sun-Earth dynamics until they leave the Earth SoI. In some cases, the unstable invariant manifolds from Sun-Earth periodic orbits depart the Earth region with more desirable characteristics. Consequently, for each cislunar

departure orbit analyzed in this investigation, transfers with direct manifold departures from the system are compared to those that stage in an intermediate Sun-Earth L_2 northern halo orbit. This comparative analysis identifies the optimal system departure strategy for each cislunar orbit.

In the context of the end-to-end transfer methodology developed in this investigation, it appears that the direct departure transfers perform better overall than those that utilize a staging orbit in terms of total maneuver Δv cost and TOF. While staging orbit transfers for a few of the selected orbits achieve a slightly lower average Δv , the direct transfers have lower times-of-flight in every case analyzed. The TOF decrease can be on the order of 1 year compared to around 0.1 km/s for maneuver costs. This conclusion is further reinforced by the cost function analysis of the transfers, where all of the direct transfer families have lower cost function values than those with staging orbits. Consequently, in this investigation, the transfers that directly depart the Earth system appear to outperform those that stage in an intermediate Sun-Earth halo orbit in terms of TOF and usually maneuver cost as well.

6.1.3 Cislunar Departure Characteristics

Each cislunar departure orbit included in this investigation provides families of transfer solutions, evaluated in a tradespace between total maneuver Δv and total TOF. For each tradespace, a cost function is applied to determine the ten lowest-cost orbits in each family (staging orbit and direct) based on mission design preferences. In this investigation, parameters are selected such that decreases in TOF are valued more highly than decreases in Δv . The characteristics of these ten lowest-cost transfers are compared between the different cislunar departure orbits to identify characteristics across families and energy levels.

The timing and placement of the second MMAT maneuver are crucial in minimizing both the total Δv maneuver cost and TOF for these interplanetary transfers. For both types of transfers developed in this investigation, the location of the second MMAT maneuver, which includes the inclination change, is the dominating factor for the transfer total Δv cost. The closer this burn occurs to the periapsis of the heliocentric bridge conic arc, the lower the maneuver cost. Additionally, in the case of transfers that directly depart the Earth

vicinity, unstable invariant manifold arcs that exit near the Sun-Earth L_2 point provide the minimum- Δv solutions in the family. On the other hand, the main contributing factor for lowering total transfer TOF is the relative phasing of the Keplerian conic arcs. When the true anomaly of the arrival conic arc at the Mars SoI intersection is just after the intersection of the bridge and arrival conic arcs, this minimizes the arrival conic arc TOF and consequently the total transfer TOF. The minimum-TOF solutions in the families occur when the invariant manifold arcs exit near the Sun-Earth L_1 Lagrange point; however, the lowest-cost transfers that balance the two parameters still exit from L_2 .

The selection of cislunar departure periodic orbit significantly influences both the maneuver cost and TOF for interplanetary transfers. In terms of maneuver cost, the L_1 halo and vertical orbit families, as well as the L_2 axial orbit family, provide the best options for staging orbit transfers. For the transfers with direct departures, the L_1 Lyapunov and halo orbit families result in the lowest- Δv transfer options. The L_1 family departures leverage close passes by the Moon to lessen the energy gap between invariant manifold arcs of two planetary systems. When it comes to the transfer TOF, L_2 Lyapunov and halo orbit families perform the best for staging orbit transfers, while L_2 halo, axial, and butterfly orbit families have the fastest direct transfers. The L_2 orbit families often have invariant manifolds that depart the Earth-Moon system faster and extend further than the L_1 orbit families. Applying the cost function to find a balance between Δv and TOF, this investigation identifies that transfers from the L_2 Lyapunov, halo, and vertical orbit families with direct departures perform well at various Jacobi constant levels. The best cislunar departure orbit identified in this investigation is the 3.13 L_2 Lyapunov orbit, whose lowest-cost transfers have an average maneuver cost of 5.282 km/s and a TOF of 3.92 years. This analysis underscores the importance of selecting appropriate cislunar departure orbits to achieve efficient deep-space transfers with a balance between maneuver cost and TOF.

Employing the two interplanetary transfer methodologies developed in this investigation, all of the included cislunar departure orbits have staging orbit and direct transfers with total maneuver costs that are up to 1 km/s less than the traditional Earth-Mars interplanetary transfer methods. And while the times-of-flight of these transfers are significantly longer than traditional interplanetary transfers due to the asymptotic nature of invariant manifolds, the

transfers with direct departures save up to 1 year compared to the staging orbit transfers. The transfers developed in this investigation confirm that invariant manifold arcs can be utilized to decrease interplanetary transfer maneuver costs and highlight a few cislunar orbit families with desirable departure characteristics.

6.2 Recommendations for Future Work

With increasing interest in interplanetary missions and the application of dynamic systems theory in multi-body trajectory design, there are many potential avenues of future research to build off the work done in this investigation. A few promising options are presented here:

- **Continue this analysis with cislunar departure orbits in a broader Jacobi constant range and transfers to other deep-space targets.**

In the current investigation, cislunar departure orbits were limited to a Jacobi constant range of 2.98-3.13. Many potentially useful unstable orbits and orbit families in the Earth-Moon CR3BP exist at Jacobi constant values outside of that range. For example, there are many families of resonant and period-multiplying orbits that were not examined in this investigation. A complete analysis of cislunar departure dynamics from unstable orbits would require an extension of the current analysis to these other orbits and families. This investigation also limited its scope by selecting a Sun-Mars L_1 northern halo orbit as its arrival destination. The methodologies developed are applicable for any unstable CR3BP arrival periodic orbit and should be verified with other arrival orbits and CR3BP deep-space target systems such as Venus or Jupiter.

- **Explore cislunar departure dynamics from stable CR3BP orbits.**

Unstable CR3BP departure and arrival periodic orbits are exclusively employed in this investigation to exploit their invariant manifolds for ballistic departures and arrivals. Unfortunately, the methodologies developed do not apply to stable CR3BP orbits due to their lack of these manifolds so other dynamical systems theory techniques are required. The utilization of impulsive maneuvers along the most stretching directions of

a periodic orbit is a promising approach for stable orbit departure and could be applied as an alternative to invariant manifold arcs with the MMAT method. Muralidharan and Howell demonstrate the usefulness of such an approach with some applications within cislunar space[54]. This approach opens alternative avenues for low-energy deep-space trajectory design by facilitating efficient departure from stable CR3BP orbits.

- **Investigate strategies for incorporating dynamical systems theory and invariant manifolds into other interplanetary transfer design methodologies and optimization.**

This investigation employed a combination of near-ballistic Earth-Moon to Sun-Earth transfers and the MMAT methodology to design interplanetary transfers, but this technique is not the only way to incorporate multi-body dynamical systems theory into deep-space trajectory design. Many other strategies exist that incorporate intentional Earth or Moon flybys or different maneuver counts and placements. It is possible that some of these methodologies could offer transfers with lower times-of-flight than those computed in this investigation. The transfers presented here, while they exist in families of solutions, are not optimized. Consequently, an exploration of other transfer methodologies that incorporates trajectory optimization is necessary to continue to improve interplanetary mission design.

- **Employ other dynamical models to confirm the results of this investigation and further explore cislunar departure dynamics.**

Since the gravitational effects of the Earth, Moon, and Sun are all considered at various stages in this investigation, depending on the dynamical model being applied, it would be beneficial to incorporate a 4-body model such as the BCR4BP to efficiently represent these dynamics. There is precedent for applying this model to the exploration of cislunar departure dynamics, and it would also simplify the construction of transfers between the Earth-Moon and Sun-Earth systems, as well as better facilitate the relative phasing between the celestial bodies[17], [36]. The inclusion of the solar gravitational

influence in the cislunar region would also aid in the departure from stable cislunar orbits through pseudo-manifolds that stem from the inclusion of the Sun in the Earth-Moon dynamical model. Finally, the results of this investigation, as well as all of those proposed in this future work section, should be validated in a high-fidelity ephemeris force model. This validation will ensure that the transfer geometries persist under a more accurate representation of the dynamical regime while also providing insight into feasible launch dates and windows in the near future for these types of deep-space transfers. Transition to higher-fidelity dynamical models is the necessary next step for these transfers to be applied to real mission scenarios.

REFERENCES

- [1] B. R. Zamora, *Gateway Space Station*, 2024. [Online]. Available: <https://www.nasa.gov/reference/gateway-about/>.
- [2] National Aeronautics and Space Administration, *NASA Strategic Plan 2022*, 2022. [Online]. Available: <https://www.nasa.gov/wp-content/uploads/2023/09/fy-22-strategic-plan-1.pdf?emrc=ff1a1e>.
- [3] National Aeronautics and Space Administration, *Moon to Mars Objectives September 2022*, 2022. [Online]. Available: <https://www.nasa.gov/wp-content/uploads/2022/09/m2m-objectives-exec-summary.pdf?emrc=119caf>.
- [4] B. G. Drake, “Human exploration of Mars design reference architecture 5.0,” NASA Lyndon B. Johnson Space Center, Tech. Rep., 2009. [Online]. Available: <https://ntrs.nasa.gov/api/citations/20090040343/downloads/20090040343.pdf>.
- [5] W. S. Koon, M. W. Lo, J. E. Marsden, and S. D. Ross, “Heteroclinic connections between periodic orbits and resonance transitions in celestial mechanics,” *Chaos: An Interdisciplinary Journal of Nonlinear Science*, vol. 10, no. 2, pp. 427–469, 2000. DOI: [10.1063/1.166509](https://doi.org/10.1063/1.166509).
- [6] H. E. S. Amiri, D. Brain, O. Sharaf, *et al.*, “The Emirates Mars mission,” *Space Science Reviews*, vol. 218, no. 4, 2022. DOI: [10.1007/s11214-021-00868-x](https://doi.org/10.1007/s11214-021-00868-x).
- [7] P. Yang, Y. Huang, P. Li, *et al.*, “Orbit determination of China’s first Mars probe Tianwen-1 during interplanetary cruise,” *Advances in Space Research*, vol. 69, pp. 1060–1071, 2022. DOI: [10.1016/j.asr.2021.10.046](https://doi.org/10.1016/j.asr.2021.10.046).
- [8] K. A. Farley, K. H. Williford, K. M. Stack, *et al.*, “Mars 2020 mission overview,” *Space Science Reviews*, vol. 216, no. 142, 2020. DOI: [10.1007/s11214-020-00762-y](https://doi.org/10.1007/s11214-020-00762-y).
- [9] D. F. Landau and J. M. Longuski, “Trajectories for human missions to Mars, Part 1: Impulsive transfers,” *Journal of Spacecraft and Rockets*, vol. 43, no. 5, pp. 1035–1042, 2006. DOI: [10.2514/1.18995](https://doi.org/10.2514/1.18995).
- [10] S. Fritz and K. Turkoglu, “Optimal trajectory determination and mission design for asteroid/deep space exploration via multi-body gravity assist maneuvers,” in *2016 IEEE Aerospace Conference*, Big Sky, Montana, USA, 2016.

- [11] J. Barrow-Green, *Poincaré and the Three Body Problem*. Providence, Rhode Island, USA: American Mathematical Society, 1997.
- [12] R. Farquhar, D. Muhonen, and L. C. Church, “Trajectories and orbital maneuvers for the ISEE-3/ICE comet mission,” in *AIAA/AAS Astrodynamics Conference*, Seattle, Washington, USA, 1984.
- [13] M. W. Lo, B. G. Williams, W. E. Bollman, *et al.*, “Genesis mission design,” *The Journal of the Astronautical Sciences*, vol. 49, no. 1, pp. 169–184, 2001. DOI: [10.1007/BF03546342](https://doi.org/10.1007/BF03546342).
- [14] M. Woodard, D. Folta, and D. Woodfork, “ARTEMIS: The first mission to the lunar libration orbits,” in *21st International Symposium on Space Flight Dynamics*, Toulouse, France, 2009.
- [15] B. Cheetham, T. Gardner, and A. Forsman, “Cislunar Autonomous Positioning System Technology Operations and Navigation Experiment (CAPSTONE),” in *ASCEND 2021*, 2021.
- [16] M. Menzel, M. Davis, K. Parrish, *et al.*, “The design, verification, and performance of the James Webb Space Telescope,” *Publications of the Astronomical Society of the Pacific*, vol. 135, no. 1047, 2023. DOI: [10.1088/1538-3873/acbb9f](https://doi.org/10.1088/1538-3873/acbb9f).
- [17] K. K. Boudad, K. C. Howell, and D. C. Davis, “Departure and escape dynamics from the near rectilinear halo orbits in the Earth-Moon-Sun system,” *The Journal of the Astronautical Sciences*, vol. 69, pp. 1076–1114, 2022. DOI: [10.1007/s40295-022-00328-w](https://doi.org/10.1007/s40295-022-00328-w).
- [18] E. M. Zimovan-Spreen, “Dynamical structures nearby NRHOs with applications to transfer design in cislunar space,” *The Journal of the Astronautical Sciences*, vol. 69, pp. 718–744, 2022. DOI: [10.1007/s40295-022-00320-4](https://doi.org/10.1007/s40295-022-00320-4).
- [19] A. Miele and T. Wang, “Optimal transfers from an Earth orbit to a Mars orbit,” *Acta Astronautica*, vol. 45, no. 3, pp. 119–133, 1999. DOI: [10.1016/S00094-5765\(99\)00109-5](https://doi.org/10.1016/S00094-5765(99)00109-5).
- [20] D. Conte, M. Di Carlo, H. Koki, D. B. Spencer, and M. Vasile, “Earth-Mars transfers through Moon distant retrograde orbits,” *Acta Astronautica*, vol. 143, pp. 372–379, 2017. DOI: [10.1016/j.actaastro.2017.12.007](https://doi.org/10.1016/j.actaastro.2017.12.007).

- [21] J. Esper and B. Aldrin, “Mars small-spacecraft human exploration resource prospector with aero-braking (SHERPA): Demonstrating an end-to-end mission to Phobos distant retrograde orbit,” in *International Astronautical Conference (IAC) 2019*, Washington, D.C., USA, 2019.
- [22] F. Topputo, M. Vasile, and F. Bernelli-Zazzera, “Low energy interplanetary transfers exploiting invariant manifolds of the restricted three-body problem,” *The Journal of the Astronautical Sciences*, vol. 53, no. 4, pp. 353–372, 2005. DOI: [10.1007/BF03546358](https://doi.org/10.1007/BF03546358).
- [23] M. Nakamiya, H. Yamakawa, D. J. Scheeres, and M. Yoshikawa, “Interplanetary transfers between halo orbits: Connectivity between escape and capture trajectories,” *Journal of Guidance, Control, and Dynamics*, vol. 33, no. 3, pp. 803–813, 2010. DOI: [10.2514/1.46446](https://doi.org/10.2514/1.46446).
- [24] S. Haibin, W. Shuai, and C. Pingyuan, “Fast low-energy halo-to-halo transfers between Sun-planet systems,” *Chinese Journal of Aeronautics*, vol. 27, no. 2, pp. 338–348, 2014. DOI: [10.1016/j.cja.2014.02.005](https://doi.org/10.1016/j.cja.2014.02.005).
- [25] M. Kakoi, K. C. Howell, and D. Folta, “Access to Mars from Earth-Moon libration point orbits: Manifold and direct options,” *Acta Astronautica*, vol. 102, pp. 269–286, 2014. DOI: [10.1016/j.actaastro.2014.06.010](https://doi.org/10.1016/j.actaastro.2014.06.010).
- [26] I. Cavallari, R. Petitdemange, and S. Lizy-Destrez, “Transfer from a lunar distant retrograde orbit to Mars through Lyapunov orbits,” in *International Symposium on Space Flight Dynamics*, Melbourne, Australia, 2019.
- [27] E. Scantamburlo, M. Guzzo, and R. I. Paez, “Interplanetary transfers using stable and unstable manifold tubes originating at L1 and L2 in the elliptic restricted three-body problems,” *Acta Astronautica*, vol. 200, pp. 97–110, 2022. DOI: [10.1016/j.actaastro.2022.07.036](https://doi.org/10.1016/j.actaastro.2022.07.036).
- [28] D. Canales, K. C. Howell, and E. Fantino, “Transfer design between neighborhoods of planetary moons in the circular restricted three-body problem: The moon-to-moon analytical transfer method,” *Celestial Mechanics and Dynamical Astronomy*, vol. 133, no. 36, 2021. DOI: [10.1007/s10569-021-10031-x](https://doi.org/10.1007/s10569-021-10031-x).
- [29] D. Canales, K. C. Howell, and E. Fantino, “A versatile moon-to-moon transfer design methodology for applications involving libration point orbits,” *Acta Astronautica*, vol. 198, pp. 388–402, 2022. DOI: [10.1016/j.actaastro.2022.06.010](https://doi.org/10.1016/j.actaastro.2022.06.010).

- [30] Y. Lu, H. Li, J. Che, Y. Yang, Y. Yang, and Y. Sun, “Design and optimization of low-energy transfer orbit to Mars with multi-body environment,” *Science China*, vol. 58, no. 10, pp. 1660–1671, 2015. DOI: [10.1007/s11431-015-5847-7](https://doi.org/10.1007/s11431-015-5847-7).
- [31] Y. Shimane and K. Ho, “Gravity-assist low-thrust inter-system trajectory design with manifold captures,” *The Journal of the Astronautical Sciences*, vol. 69, pp. 193–217, 2022. DOI: [10.1007/s40295-022-00319-x](https://doi.org/10.1007/s40295-022-00319-x).
- [32] S. K. Singh and K. Negi, “Earth-Mars halo to halo low thrust manifold transfers using variable specific impulse engine,” *Acta Astronautica*, vol. 220, 2024. DOI: [10.1016/j.actaastro.2024.03.049](https://doi.org/10.1016/j.actaastro.2024.03.049).
- [33] J. J. Masdemont, G. Gomez, L. Lei, and H. Peng, “Global analysis of direct transfers from lunar orbits to Sun-Earth libration point regimes,” *Celestial Mechanics and Dynamical Astronomy*, vol. 133, no. 15, 2021. DOI: [10.1007/s10569-021-10011-1](https://doi.org/10.1007/s10569-021-10011-1).
- [34] Q. Guo and H. Lei, “Families of Earth-Moon trajectories with applications to transfers towards Sun-Earth libration point orbits,” *Astrophysics and Space Science*, vol. 364, no. 43, 2019. DOI: [10.1007/s10509-019-3532-1](https://doi.org/10.1007/s10509-019-3532-1).
- [35] A. Pasquale, M. Lavagna, and F. Renk, “Cislunar escape trajectories through patched Sun-Earth/Earth-Moon three-body problem,” in *72nd International Astronautical Congress*, Dubai, UAE, 2021.
- [36] K. Boudad, K. Howell, and D. Davis, “Energy and phasing considerations for low-energy transfers from cislunar to heliocentric space,” in *31st AAS/AIAA Spaceflight Mechanics Meeting*, Charlotte, North Carolina, USA, 2021.
- [37] D. C. Garcia, “Transfer design methodology between neighborhoods of planetary moons in the circular restricted three-body problem,” Ph.D. Dissertation, Purdue University, West Lafayette, IN, USA, 2021.
- [38] M. Kakoi, “Design of transfers from Earth-Moon L_1/L_2 libration point orbits to a destination object,” Ph.D. Dissertation, Purdue University, West Lafayette, IN, USA, 2015.
- [39] B. Semenov, *SPICE: An observation geometry system for space science missions*, 2023. [Online]. Available: <https://naif.jpl.nasa.gov/naif/>.
- [40] D. A. Vallado, *Fundamentals of Astrodynamics and Applications*, Fourth Edition. Hawthorne, CA, USA: Microcosm Press, 2013.

- [41] E. M. Zimovan, “Characteristics and design strategies for near rectilinear halo orbits within the Earth-Moon system,” M.S. Thesis, Purdue University, West Lafayette, IN, USA, 2017.
- [42] K. K. Boudad, “Disposal dynamics from the vicinity of near rectilinear halo orbits in the Earth-Moon-Sun system,” M.S. Thesis, Purdue University, West Lafayette, IN, USA, 2018.
- [43] D. J. Scheeres, “The restricted Hill four-body problem with applications to the Earth-Moon-Sun system,” *Celestial Mechanics and Dynamical Astronomy*, vol. 70, pp. 75–98, 1998. DOI: [10.1023/A:1026498608950](https://doi.org/10.1023/A:1026498608950).
- [44] M. A. Andreu, “Dynamics in the center manifold around L2 in the quasi-bicircular problem,” *Celestial Mechanics and Dynamical Astronomy*, vol. 84, pp. 105–133, 2002. DOI: [10.1023/A:1019979414586](https://doi.org/10.1023/A:1019979414586).
- [45] J. S. Parker and R. L. Anderson, *Low-Energy Lunar Trajectory Design*. Pasadena, CA, USA: NASA Jet Propulsion Laboratory, 2013.
- [46] D. J. Grebow, “Generating periodic orbits in the circular restricted three-body problem with applications to lunar south pole coverage,” M.S. Thesis, Purdue University, West Lafayette, IN, USA, 2006.
- [47] N. I. Sadaka, “There and back again: Generating repeating transfers using resonant structures,” M.S. Thesis, Purdue University, West Lafayette, IN, USA, 2023.
- [48] R. Park, *Three-body periodic orbits*. [Online]. Available: https://ssd.jpl.nasa.gov/tools/periodic_orbits.html.
- [49] E. M. Zimovan Spreen, “Trajectory design and targeting for applications to the exploration program in cislunar space,” Ph.D. Dissertation, Purdue University, West Lafayette, IN, USA, 2021.
- [50] R. J. Power, “Characterization of lunar access relative to cislunar orbits,” M.S. Thesis, Purdue University, West Lafayette, IN, USA, 2019.
- [51] L. Perko, *Differential Equations and Dynamical Systems*, Third Edition. New York City, NY, USA: Springer, 1991.

- [52] D. Guzzetti, E. M. Zimovan, K. C. Howell, and D. C. Davis, “Stationkeeping analysis for spacecraft in lunar near rectilinear halo orbits,” in *27th AAS/AIAA Space Flight Mechanics Meeting*, 2017.
- [53] D. Eagle, *Earth-to-Mars interplanetary pork chop plots*, 2022. [Online]. Available: <https://www.mathworks.com/matlabcentral/fileexchange/39248-earth-to-mars-interplanetary-pork-chop-plots>.
- [54] V. Muralidharan and K. C. Howell, “Stretching directions in cislunar space: Applications for departures and transfer design,” *Astroynamics*, vol. 7, no. 2, pp. 153–178, 2022. DOI: [10.1007/s42064-022-0147-z](https://doi.org/10.1007/s42064-022-0147-z).

A. END-TO-END TRANSFER TRADESPACES

L_1 Lyapunov Orbits

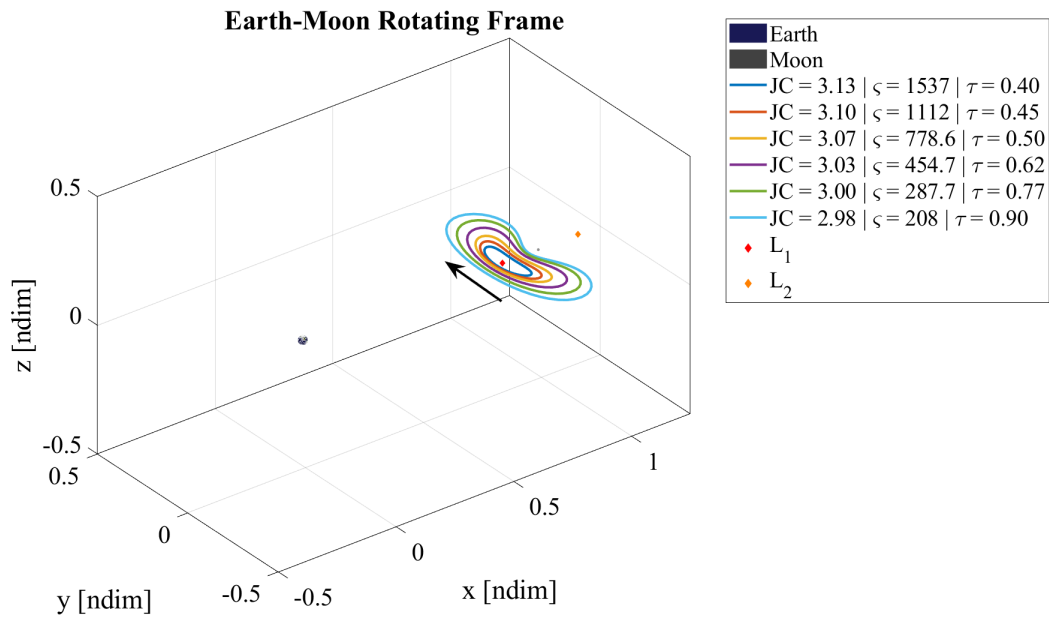


Figure A.1. Earth-Moon L_1 Lyapunov departure orbits and their stability characteristics.

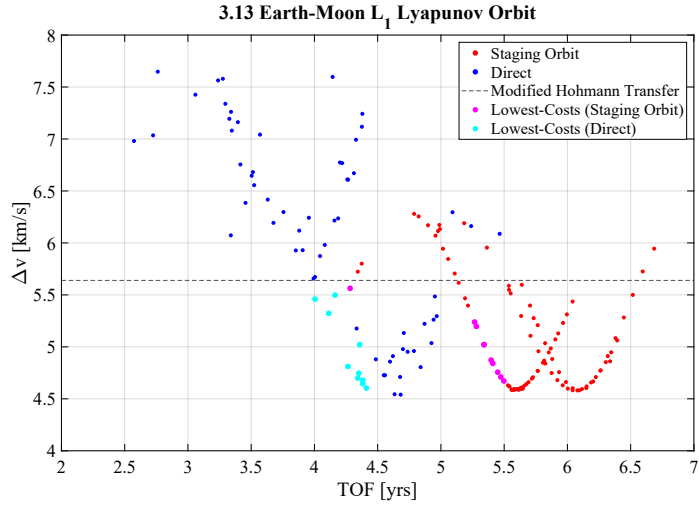


Figure A.2. Transfer tradespace departing from an Earth-Moon L_1 Lyapunov orbit ($JC = 3.13$).

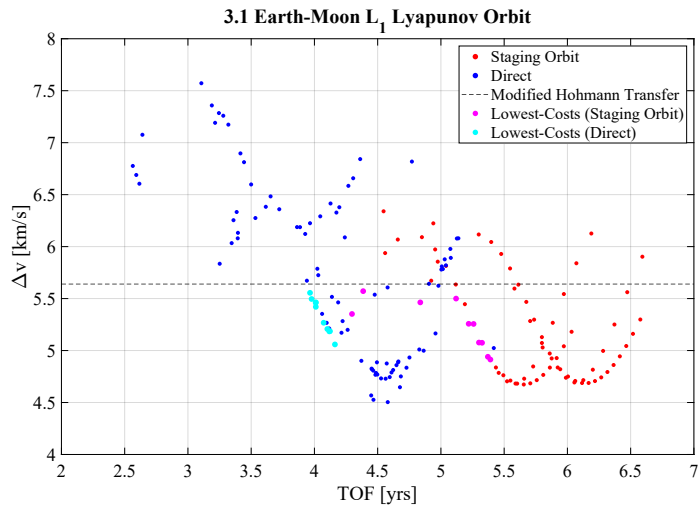


Figure A.3. Transfer tradespace departing from an Earth-Moon L_1 Lyapunov orbit ($JC = 3.1$).

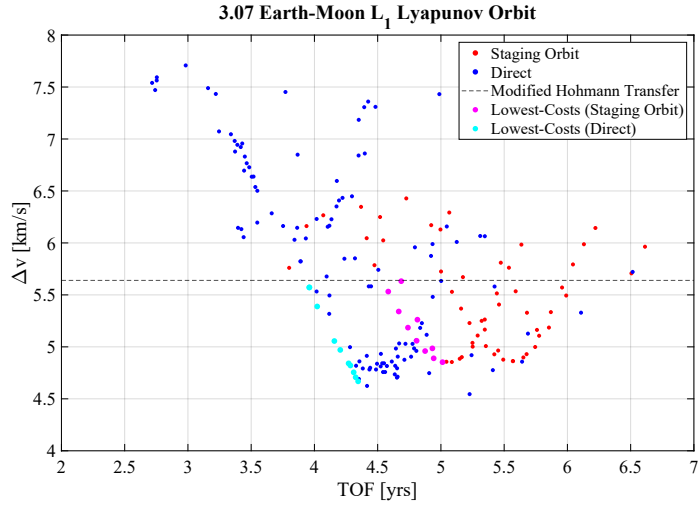


Figure A.4. Transfer tradespace departing from an Earth-Moon L_1 Lyapunov orbit ($JC = 3.07$).

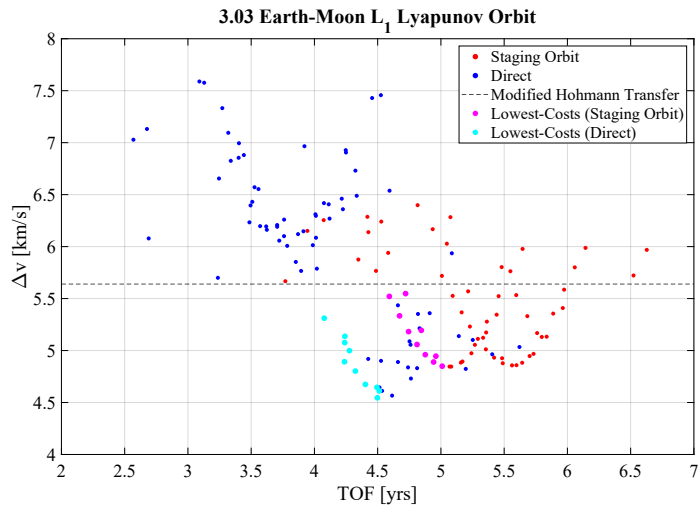


Figure A.5. Transfer tradespace departing from an Earth-Moon L_1 Lyapunov orbit ($JC = 3.03$).

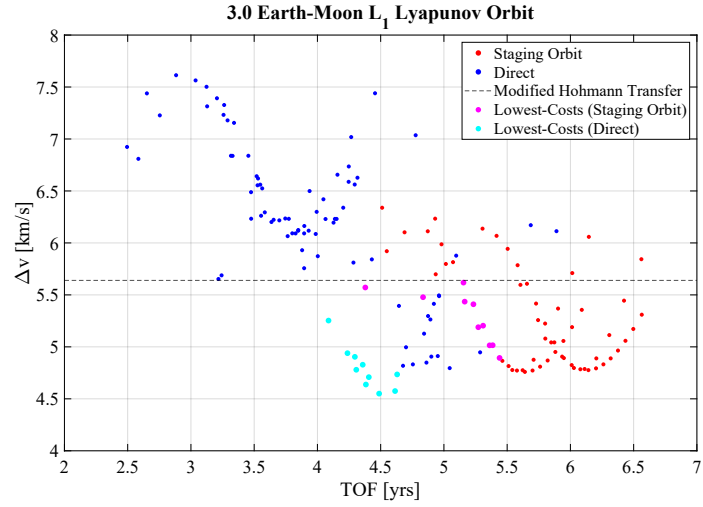


Figure A.6. Transfer tradespace departing from an Earth-Moon L_1 Lyapunov orbit ($JC = 3.0$).

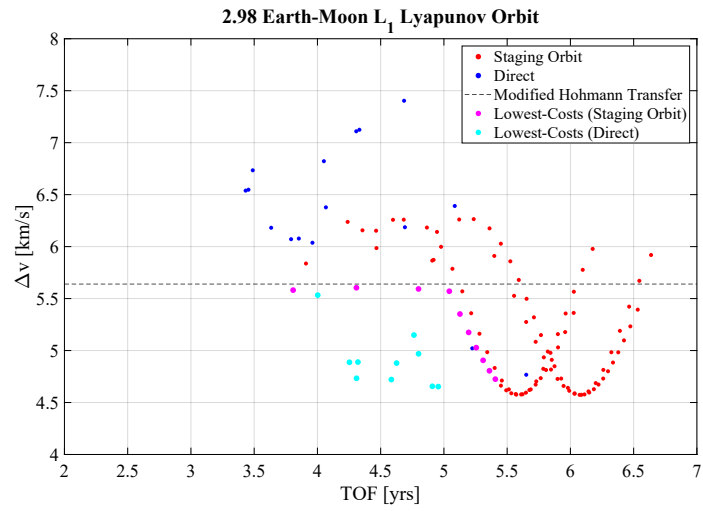


Figure A.7. Transfer tradespace departing from an Earth-Moon L_1 Lyapunov orbit ($JC = 2.98$).

L_2 Lyapunov Orbits

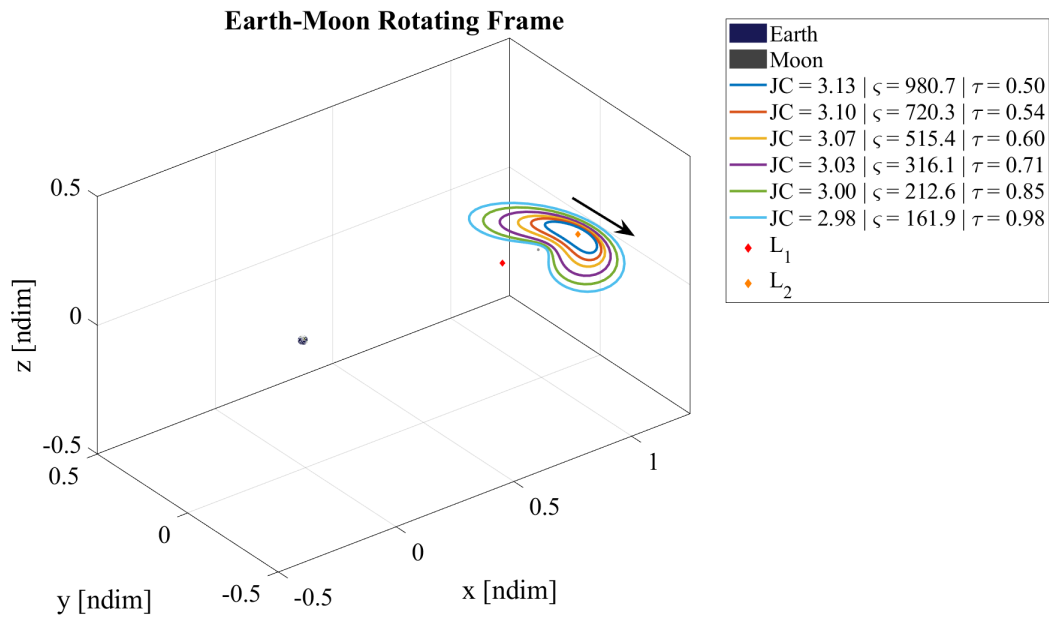


Figure A.8. Earth-Moon L_2 Lyapunov departure orbits and their stability characteristics.

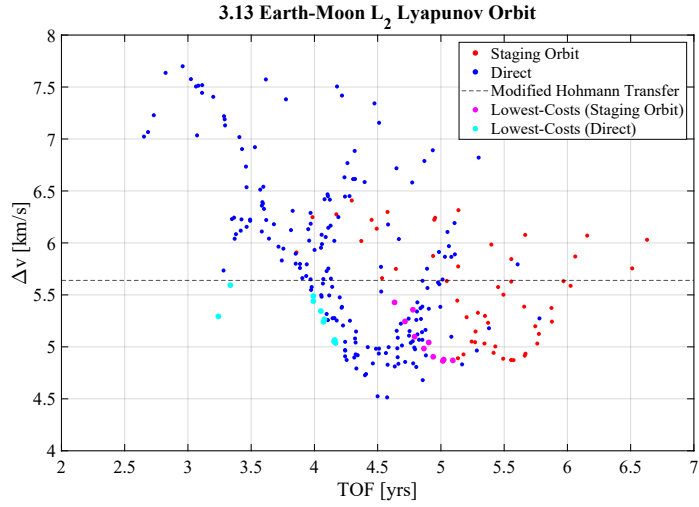


Figure A.9. Transfer tradespace departing from an Earth-Moon L_2 Lyapunov orbit ($JC = 3.13$).

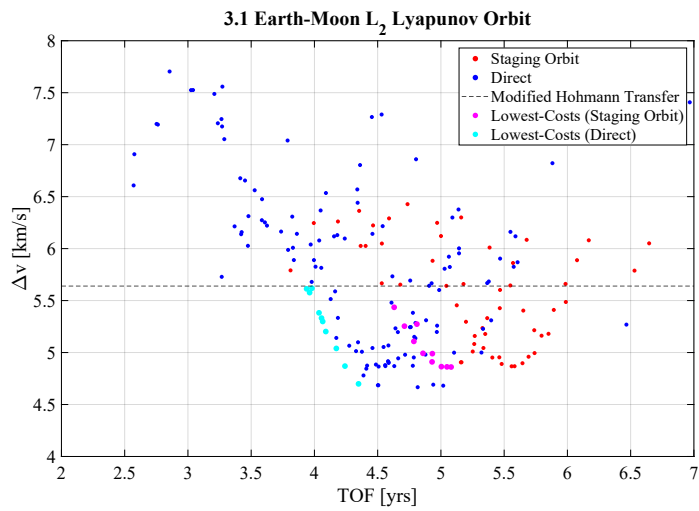


Figure A.10. Transfer tradespace departing from an Earth-Moon L_2 Lyapunov orbit ($JC = 3.1$).

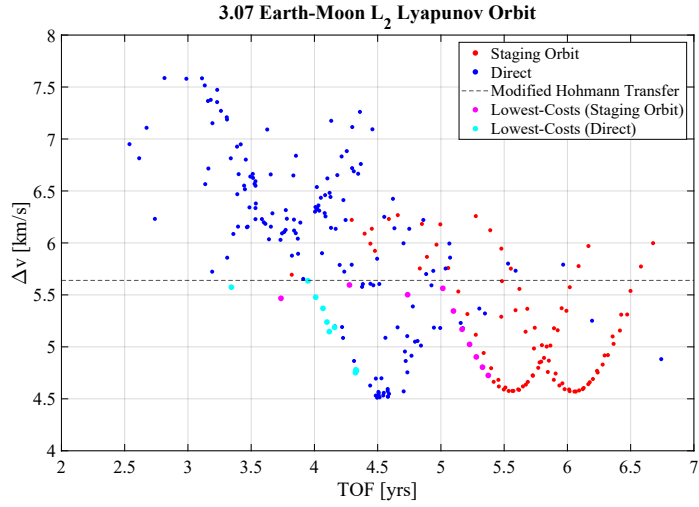


Figure A.11. Transfer tradespace departing from an Earth-Moon L_2 Lyapunov orbit ($JC = 3.07$).

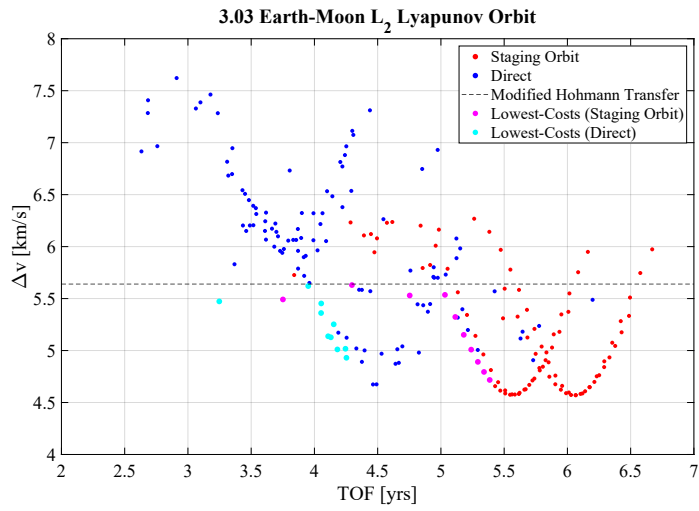


Figure A.12. Transfer tradespace departing from an Earth-Moon L_2 Lyapunov orbit ($JC = 3.03$).

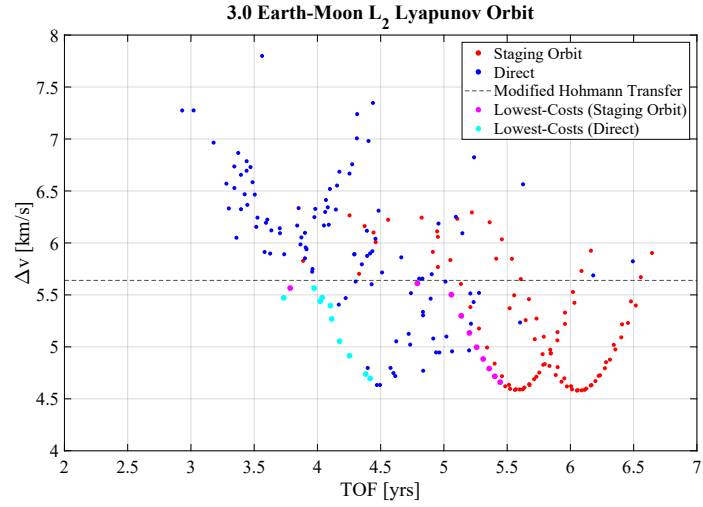


Figure A.13. Transfer tradespace departing from an Earth-Moon L_2 Lyapunov orbit ($JC = 3.0$).

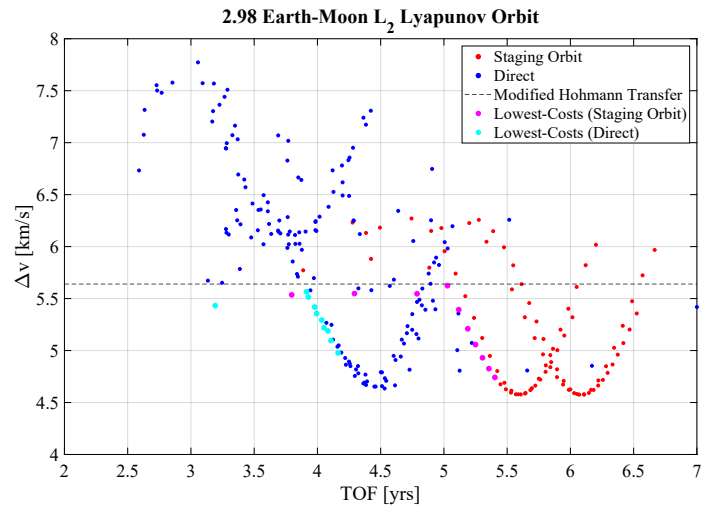


Figure A.14. Transfer tradespace departing from an Earth-Moon L_2 Lyapunov orbit ($JC = 2.98$).

L_1 Halo Orbits

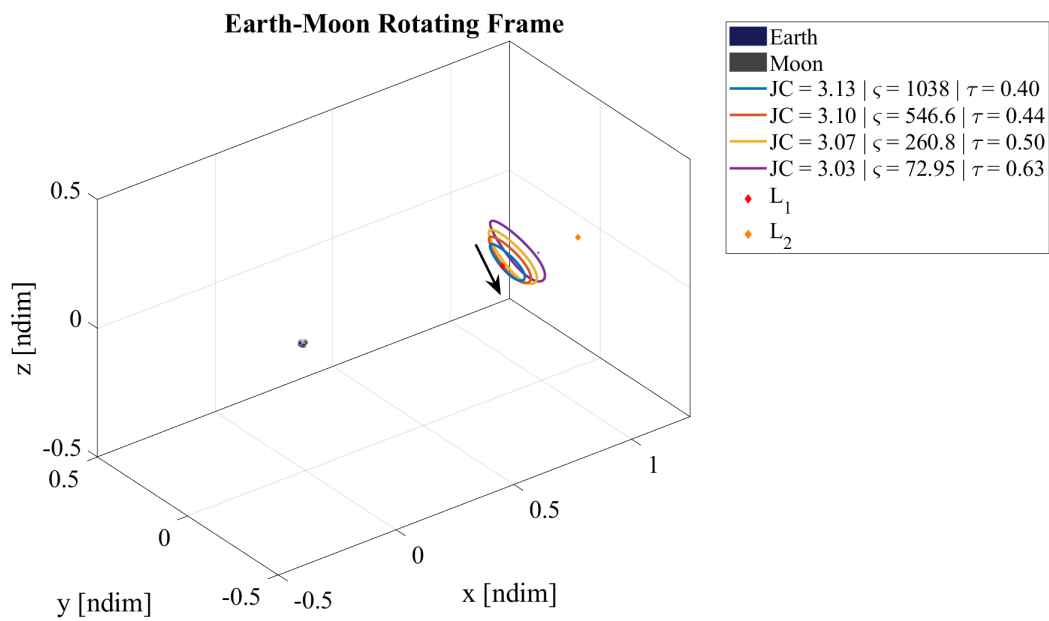


Figure A.15. Earth-Moon L_1 northern halo departure orbits and their stability characteristics.

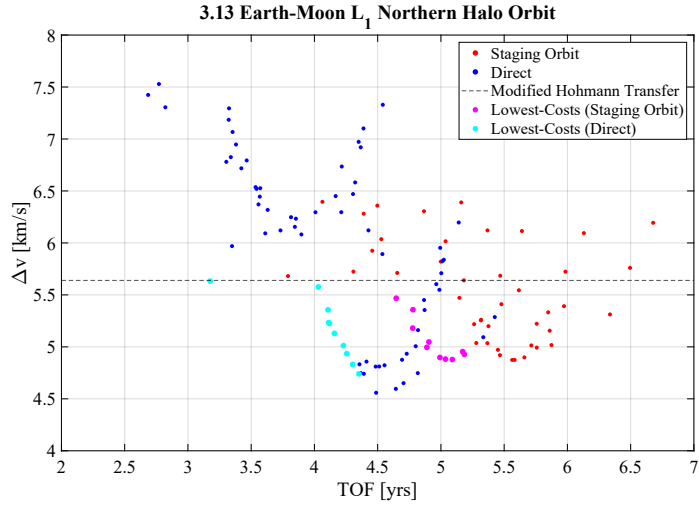


Figure A.16. Transfer tradespace departing from an Earth-Moon L_1 northern halo orbit ($JC = 3.13$).

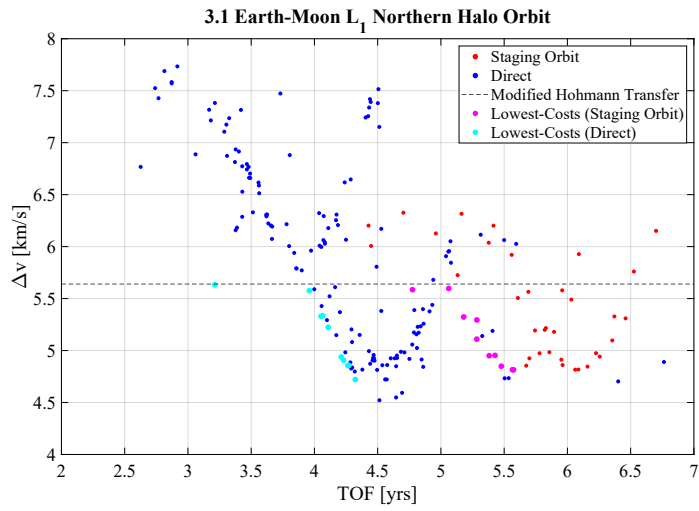


Figure A.17. Transfer tradespace departing from an Earth-Moon L_1 northern halo orbit ($JC = 3.1$).

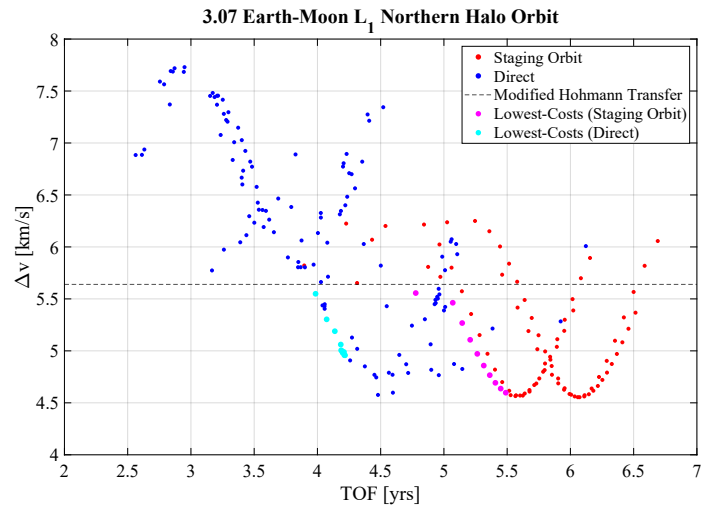


Figure A.18. Transfer tradespace departing from an Earth-Moon L_1 northern halo orbit ($JC = 3.07$).

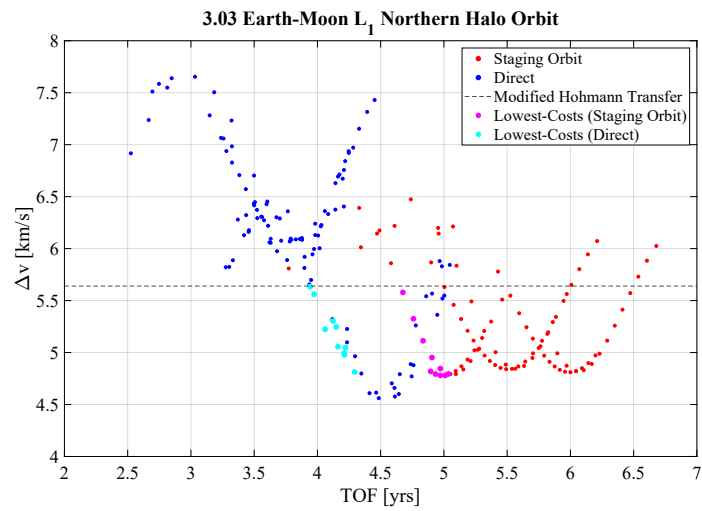


Figure A.19. Transfer tradespace departing from an Earth-Moon L_1 northern halo orbit ($JC = 3.03$).

L_2 Halo Orbits

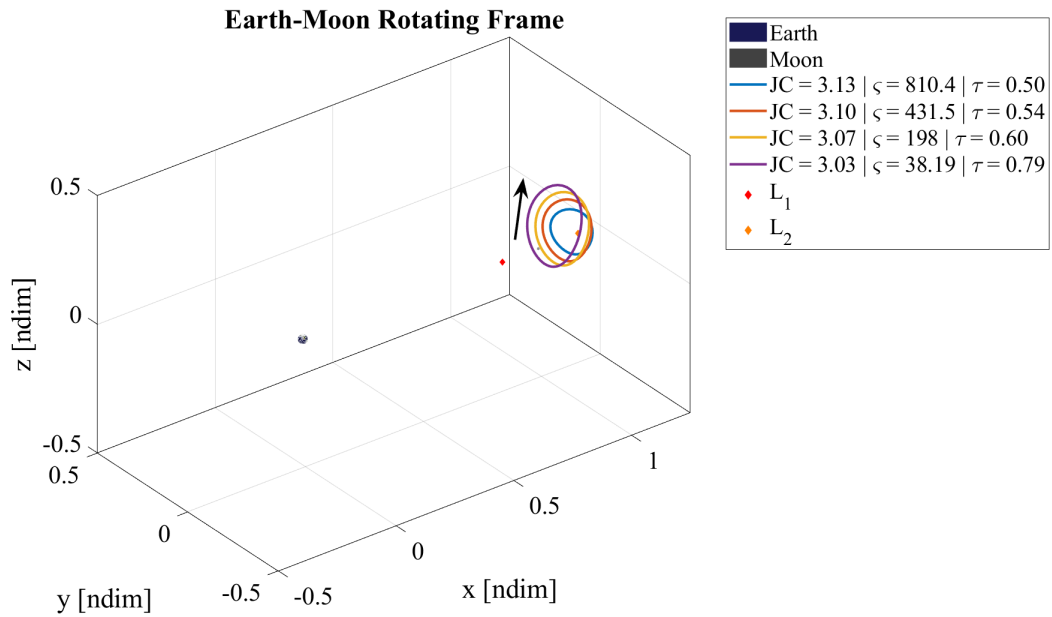


Figure A.20. Earth-Moon L_2 northern halo departure orbits and their stability characteristics.

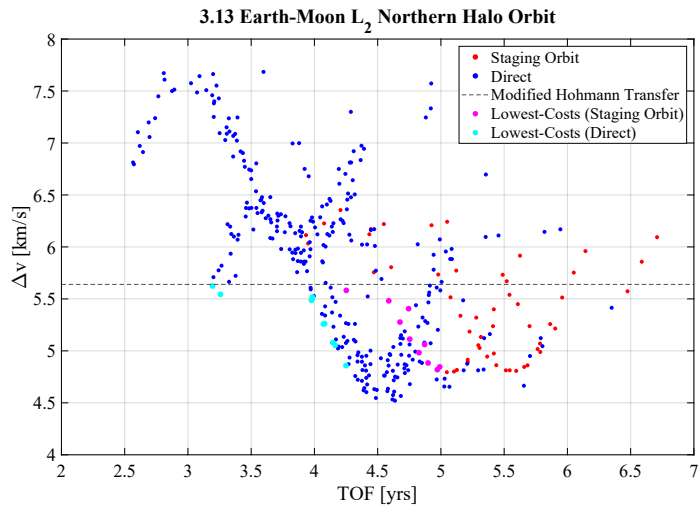


Figure A.21. Transfer tradespace departing from an Earth-Moon L_2 northern halo orbit ($JC = 3.13$).

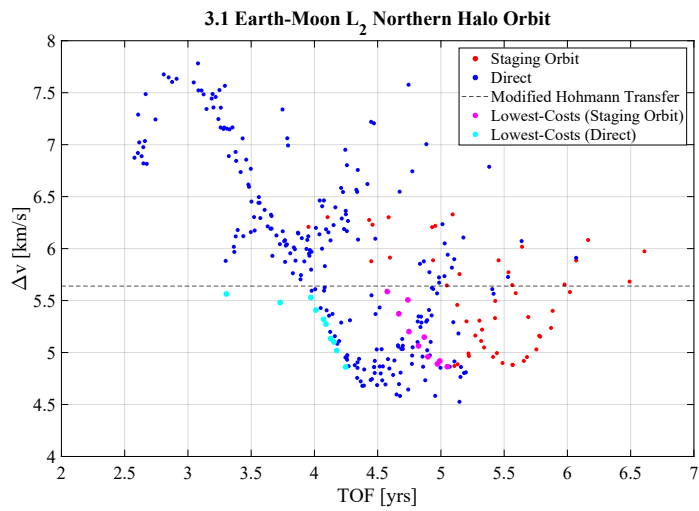


Figure A.22. Transfer tradespace departing from an Earth-Moon L_2 northern halo orbit ($JC = 3.1$).

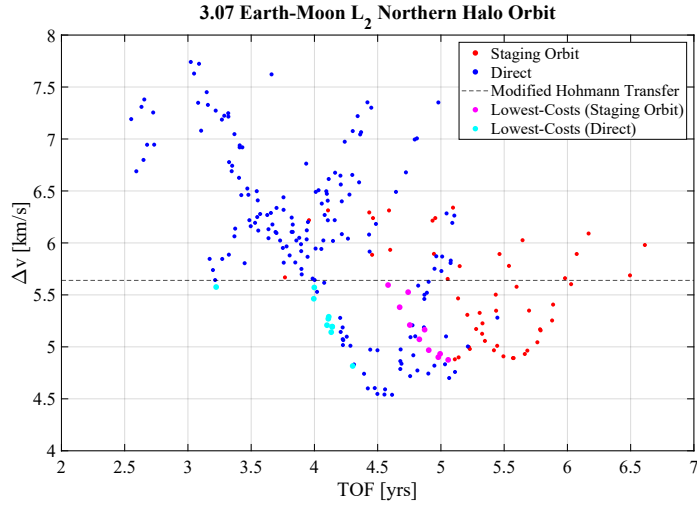


Figure A.23. Transfer tradespace departing from an Earth-Moon L_2 northern halo orbit ($JC = 3.07$).

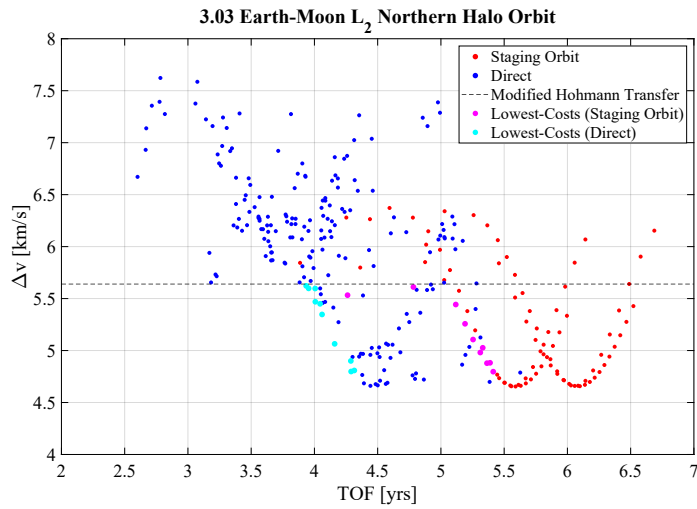


Figure A.24. Transfer tradespace departing from an Earth-Moon L_2 northern halo orbit ($JC = 3.03$).

L_1 Axial Orbits

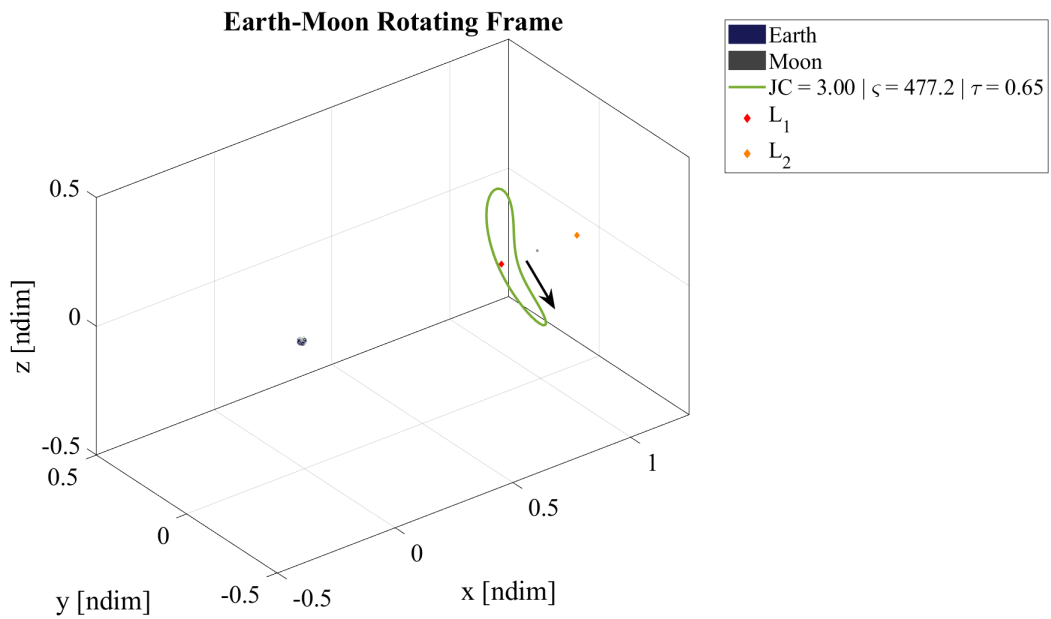


Figure A.25. Earth-Moon L_1 northwestern axial departure orbits and their stability characteristics.

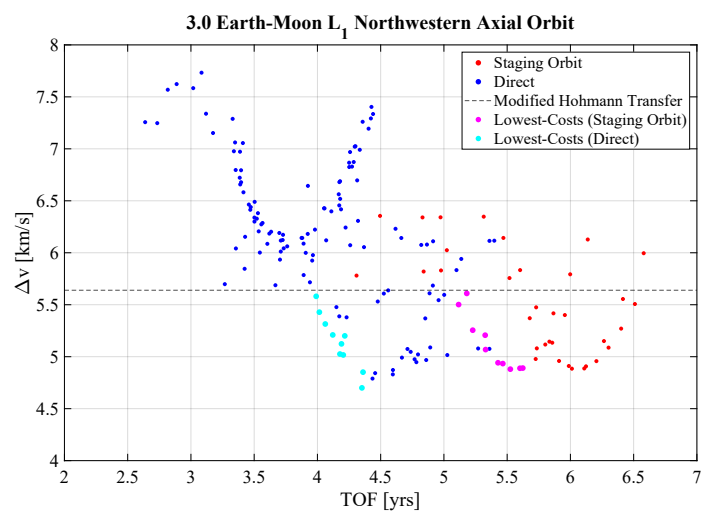


Figure A.26. Transfer tradespace departing from an Earth-Moon L_1 northwestern axial orbit ($JC = 3.0$).

L_2 Axial Orbits

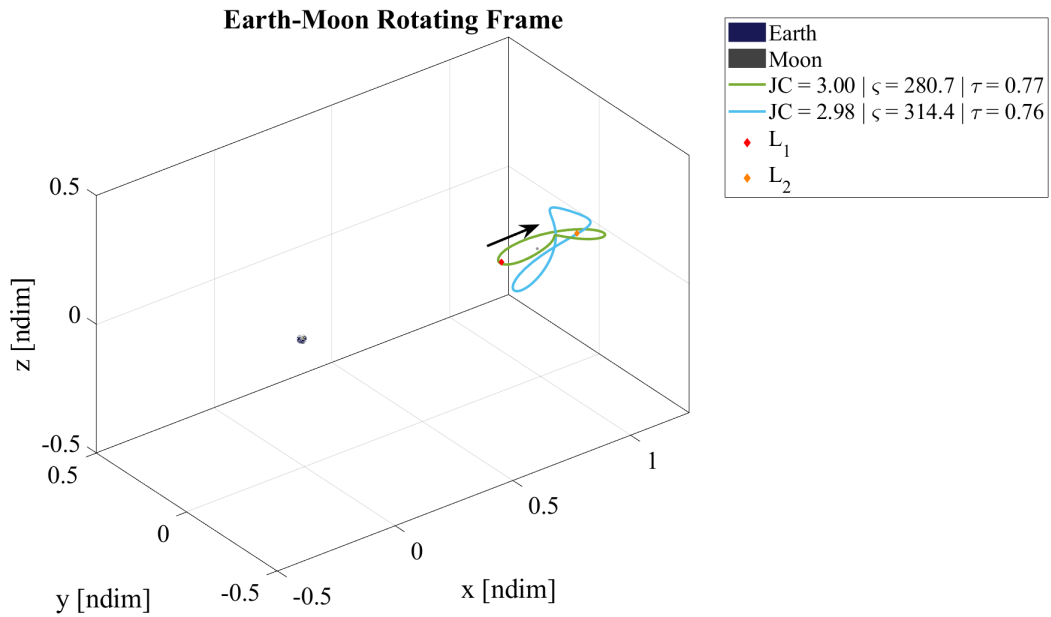


Figure A.27. Earth-Moon L_2 northeastern axial departure orbits and their stability characteristics.

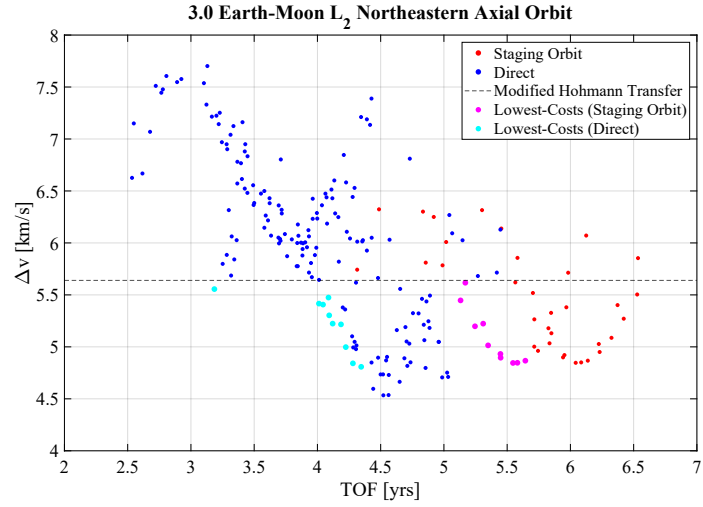


Figure A.28. Transfer tradespace departing from an Earth-Moon L_2 north-eastern axial orbit ($JC = 3.0$).

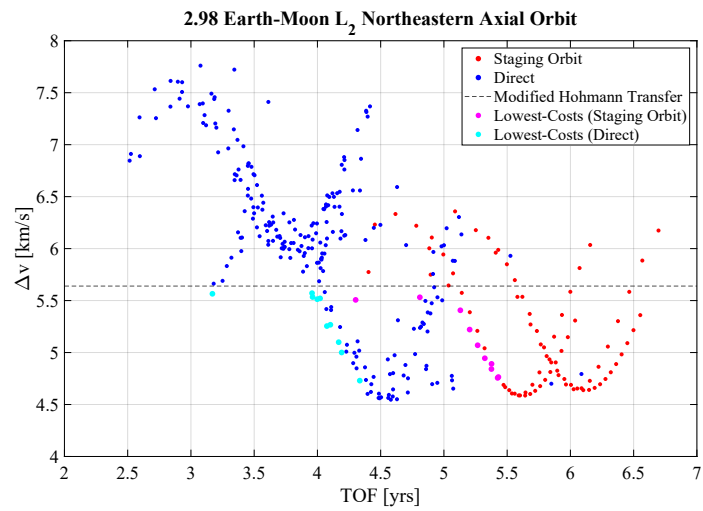


Figure A.29. Transfer tradespace departing from an Earth-Moon L_2 north-eastern axial orbit ($JC = 2.98$).

L_1 Vertical Orbits

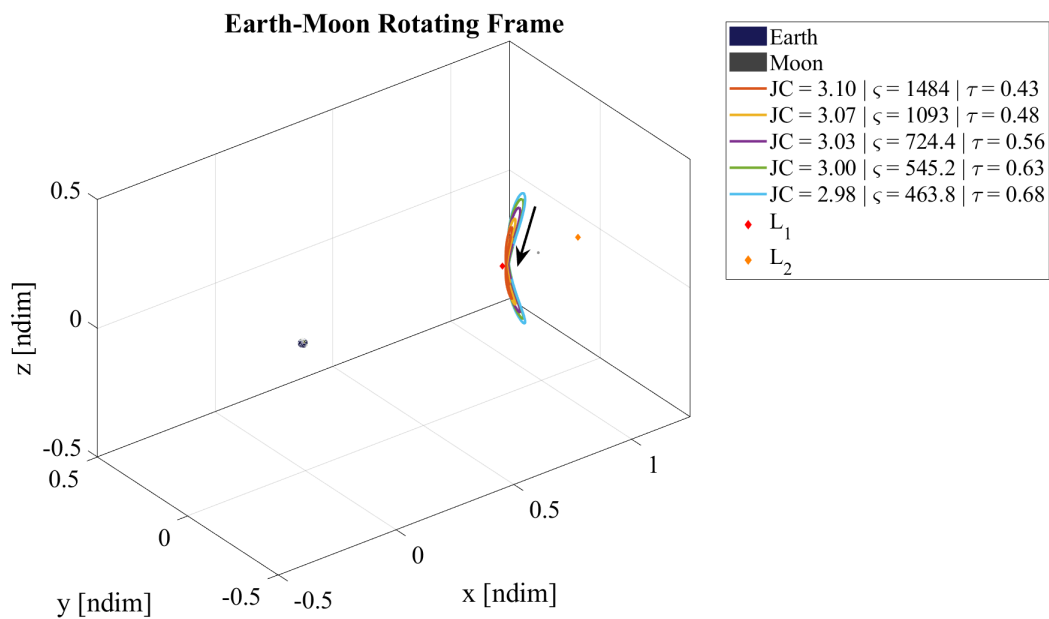


Figure A.30. Earth-Moon L_1 vertical departure orbits and their stability characteristics.

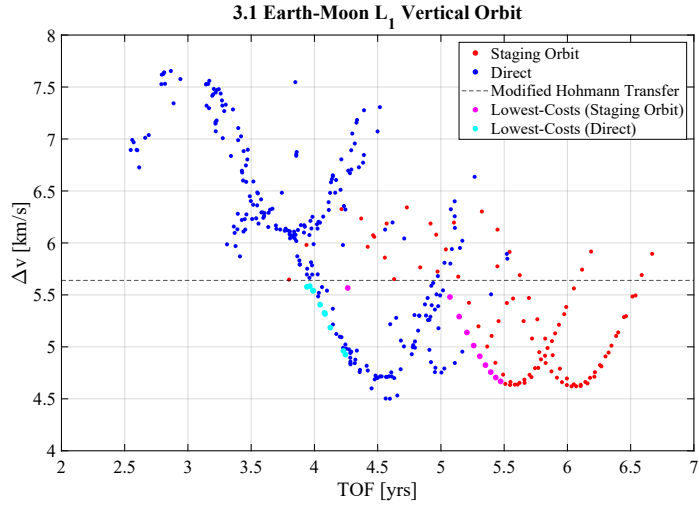


Figure A.31. Transfer tradespace departing from an Earth-Moon L_1 vertical orbit ($JC = 3.1$).

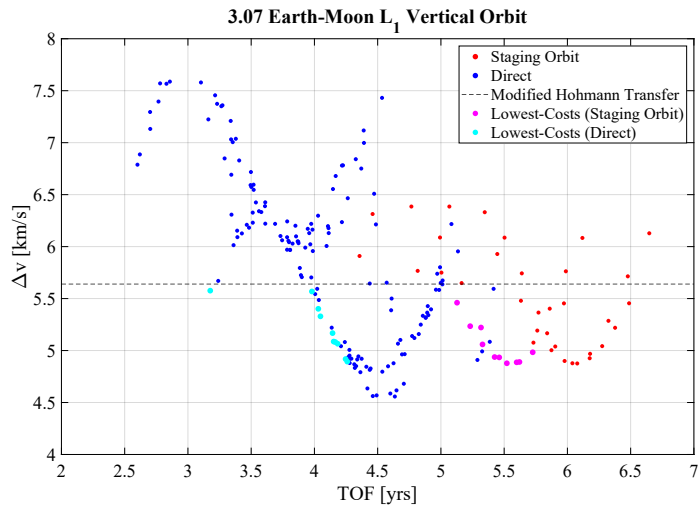


Figure A.32. Transfer tradespace departing from an Earth-Moon L_1 vertical orbit ($JC = 3.07$).

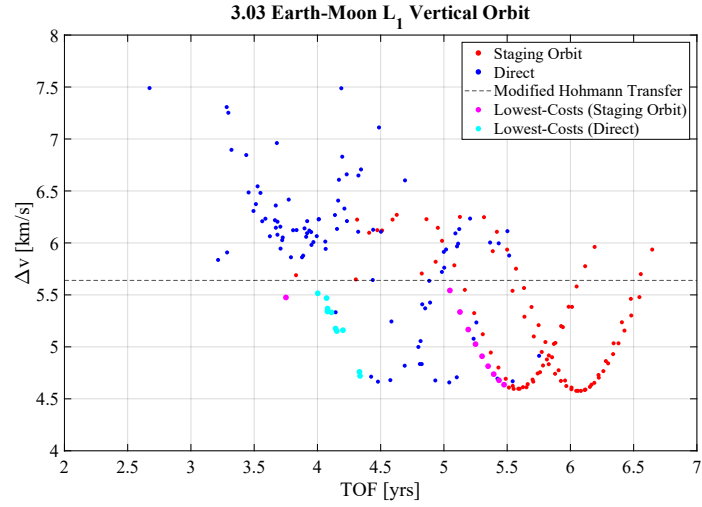


Figure A.33. Transfer tradespace departing from an Earth-Moon L_1 vertical orbit ($JC = 3.03$).

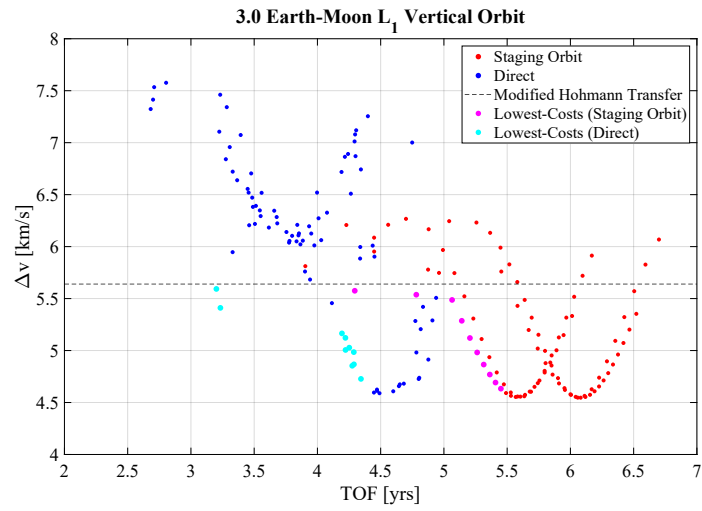


Figure A.34. Transfer tradespace departing from an Earth-Moon L_1 vertical orbit ($JC = 3.0$).

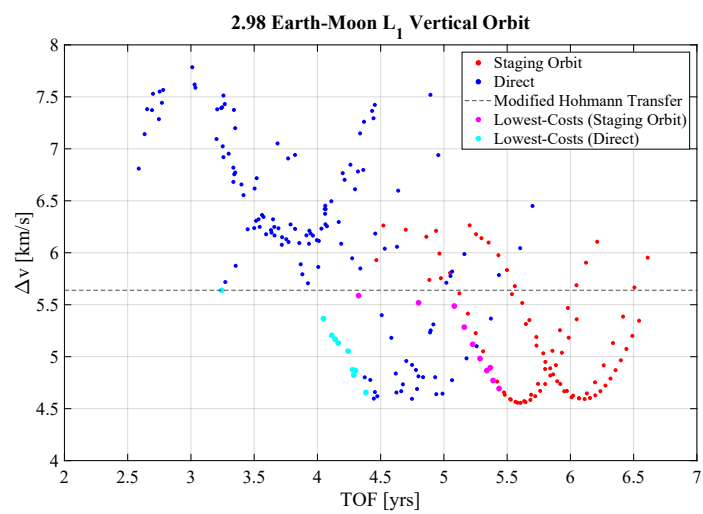


Figure A.35. Transfer tradespace departing from an Earth-Moon L_1 vertical orbit ($JC = 2.98$).

L_2 Vertical Orbits

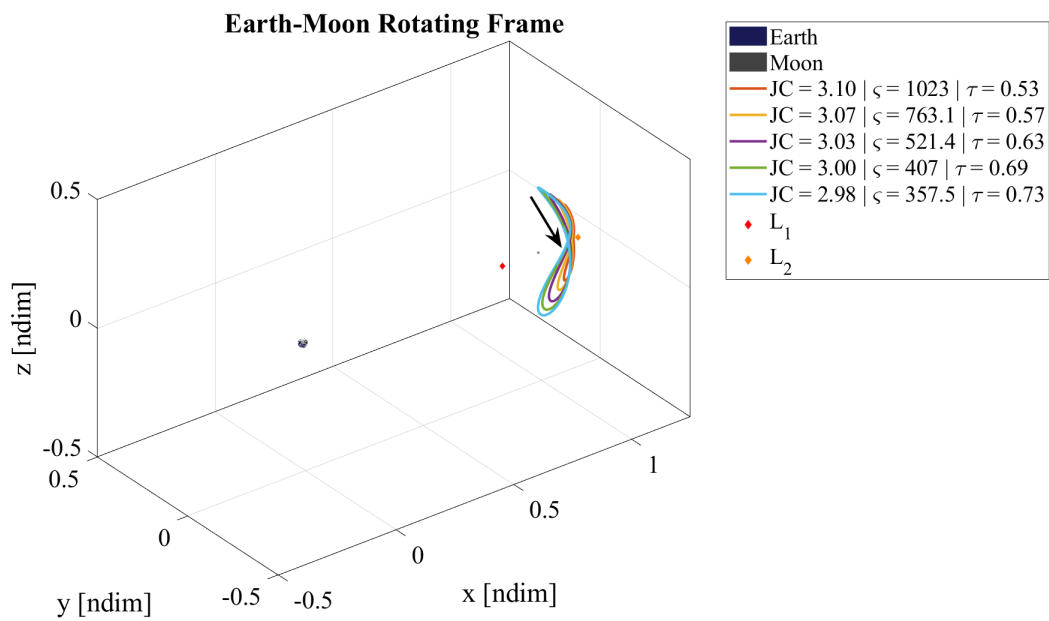


Figure A.36. Earth-Moon L_2 vertical departure orbits and their stability characteristics.

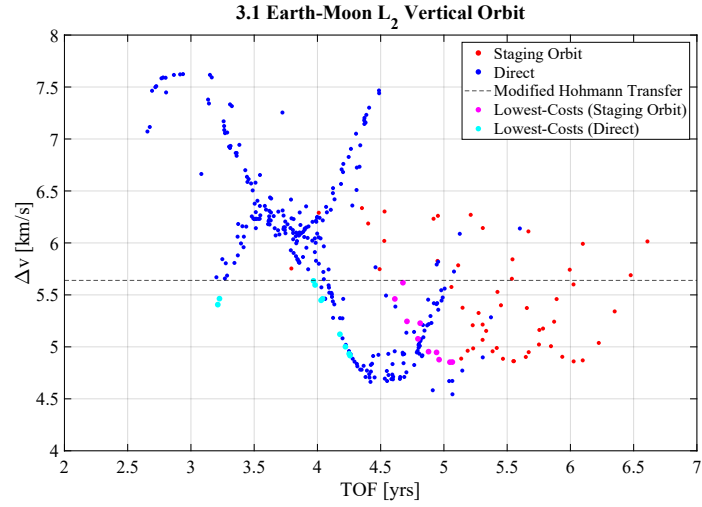


Figure A.37. Transfer tradespace departing from an Earth-Moon L_2 vertical orbit ($JC = 3.1$).

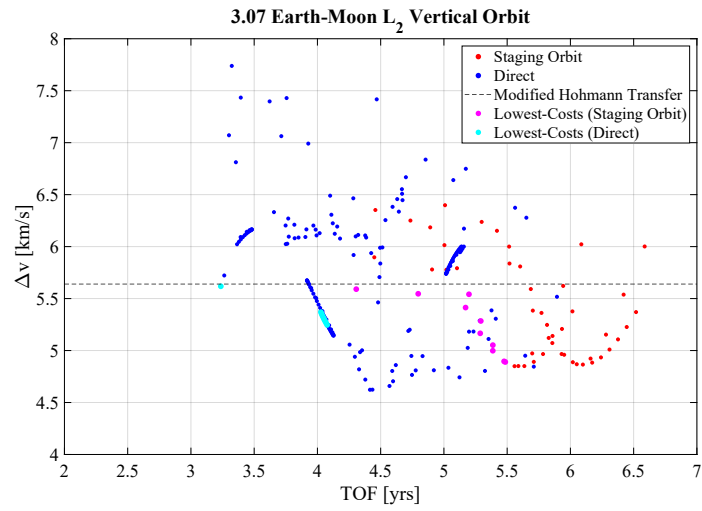


Figure A.38. Transfer tradespace departing from an Earth-Moon L_2 vertical orbit ($JC = 3.07$).

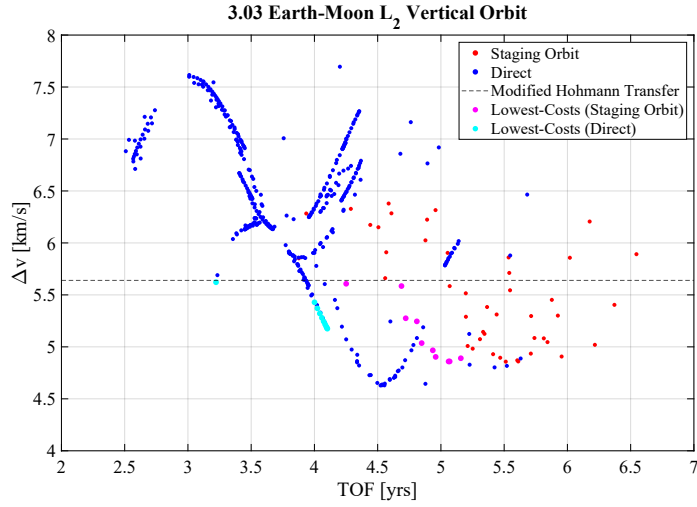


Figure A.39. Transfer tradespace departing from an Earth-Moon L_2 vertical orbit ($JC = 3.03$).

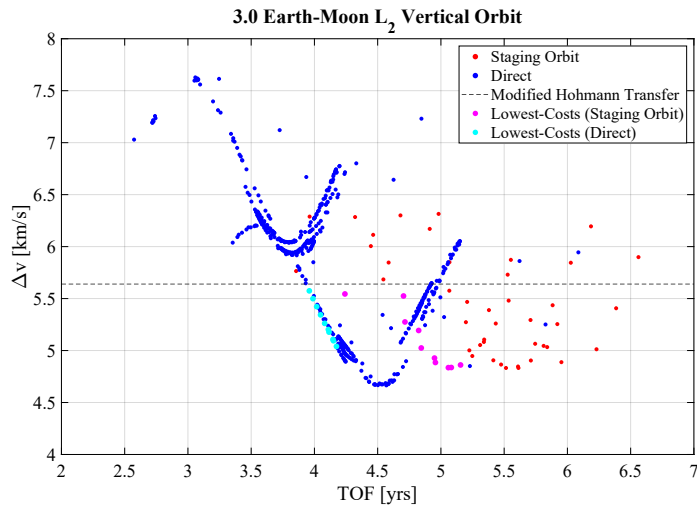


Figure A.40. Transfer tradespace departing from an Earth-Moon L_2 vertical orbit ($JC = 3.0$).

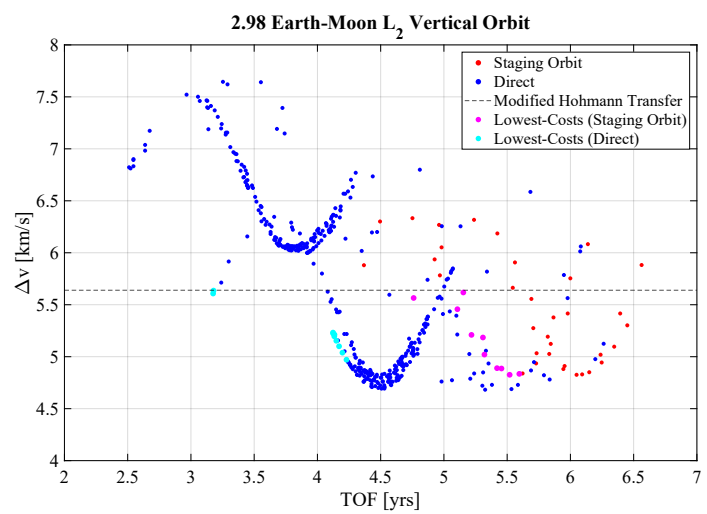


Figure A.41. Transfer tradespace departing from an Earth-Moon L_2 vertical orbit ($JC = 2.98$).

Butterfly Orbits

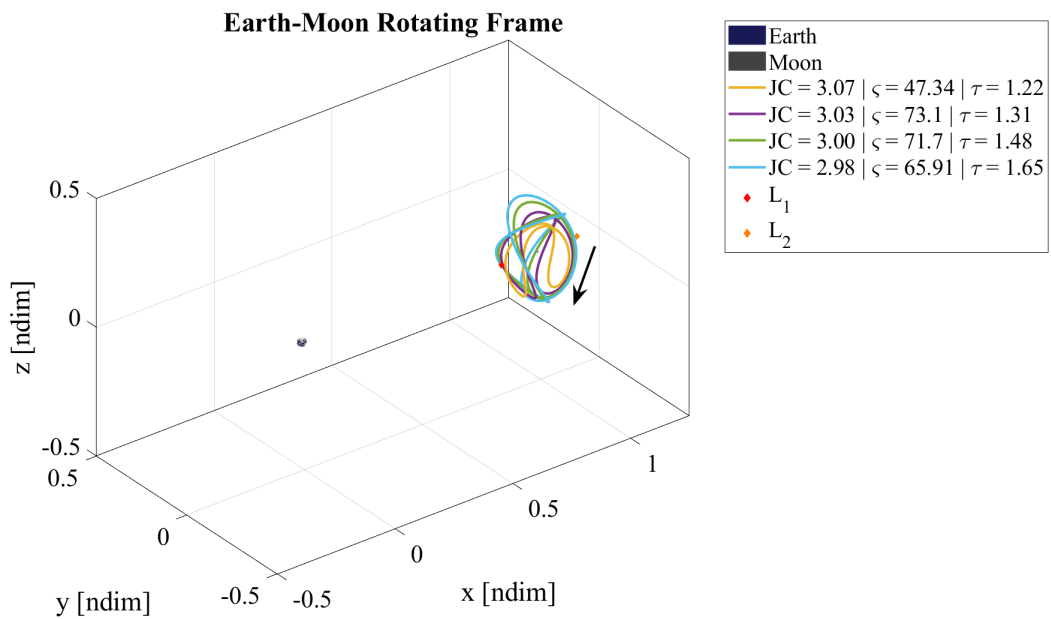


Figure A.42. Earth-Moon butterfly departure orbits and their stability characteristics.

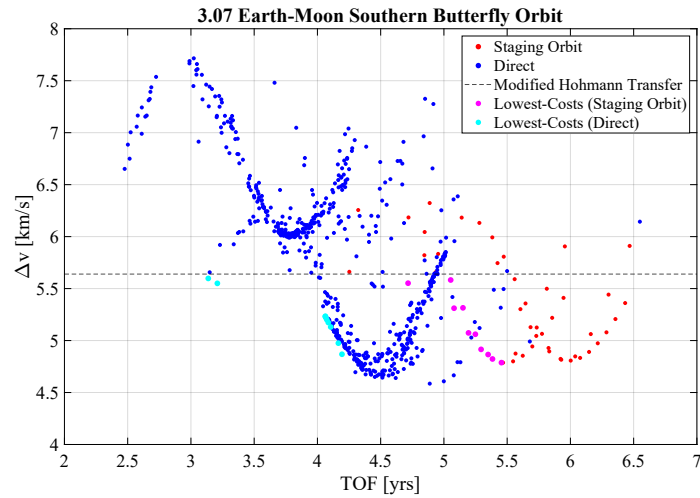


Figure A.43. Transfer tradespace departing from an Earth-Moon butterfly orbit ($JC = 3.07$).

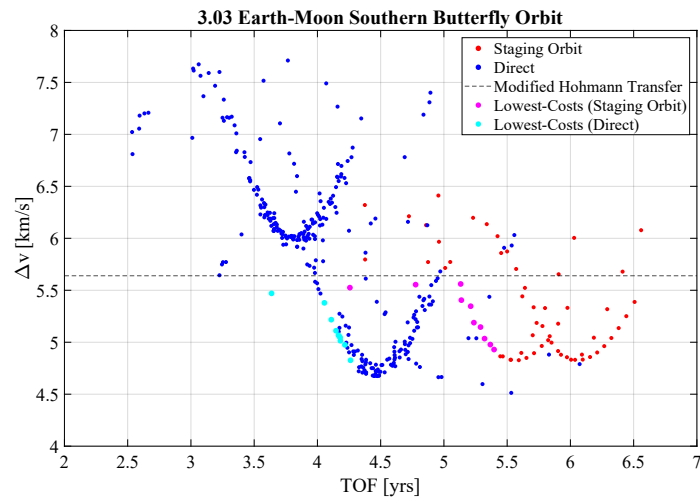


Figure A.44. Transfer tradespace departing from an Earth-Moon butterfly orbit ($JC = 3.03$).

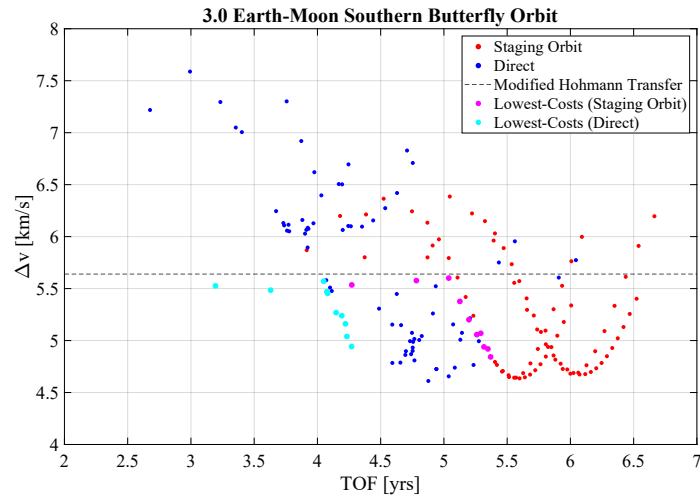


Figure A.45. Transfer tradespace departing from an Earth-Moon butterfly orbit ($JC = 3.0$).

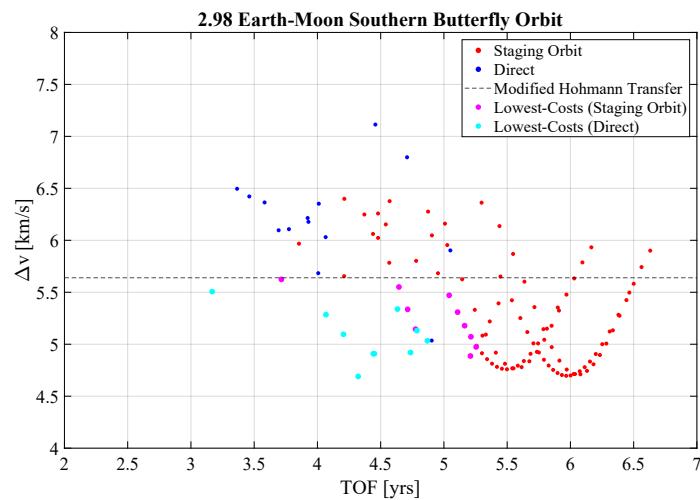


Figure A.46. Transfer tradespace departing from an Earth-Moon butterfly orbit ($JC = 2.98$).